UC San Diego
UC San Diego Electronic Theses and Dissertations

Title
Development of stratocumulus cloud modeling in coastal California for solar forecasting

Permalink
https://escholarship.org/uc/item/4r21r4tw

Author
Wu, Elynn

Publication Date
2020

Peer reviewed|Thesis/dissertation

UNIVERSITY OF CALIFORNIA SAN DIEGO

Development of stratocumulus cloud modeling in coastal California for solar forecasting

A dissertation submitted in partial satisfaction of the
requirements for the degree
Doctor of Philosophy

in

Engineering Sciences (Mechanical Engineering)

by

Elynn Wu

Committee in charge:

Professor Jan Kleissl, Chair
Professor Carlos Coimbra
Professor Joel Norris
Professor Eugene Pawlak
Professor Lynn Russell

2020

The dissertation of Elynn Wu is approved, and it is accept-

able in quality and form for publication on microfilm and

electronically:

_____

_____

_____

_____

_____

Chair

University of California San Diego

2020

DEDICATION

This work is dedicated to my parents for their love and support.

TABLE OF CONTENTS

LIST OF FIGURES

LIST OF TABLES

ACKNOWLEDGEMENTS

I would like to first thank my advisor, Jan Kleissl, for his support and feedback for me throughout my study. Having Jan as my advisor has not only made the journey possible but also fun and exciting. I appreciate his trust in letting me pursue interesting research ideas, and I truly enjoy all the serious and funny discussions we had in our meetings.

I am also grateful for Carlos Coimbra, Joel Norris, Eugene Pawlak, Lynn Russell for being on my committee and offering suggestions and discussions about my research. I am extremely grateful for Kay Suselj, Marcin Kurowski, and Joao Teixeira. They have supported me immensely during my stay in JPL and beyond. Their insights on NWP have made the last two chapters of this thesis possible. I would also like to express my gratitude to Thijs Heus for his expertise in clouds and LES, and for letting me in on the open-source CFD project. I also appreciate my collaborators: Rachel Clemesha, Dazhi Yang, and Luca Delle Monache for their support and dedication, and Kelsey Johnson for managing the EVSA project and going on electric car field trips with me.

Furthermore, I would like to thank my labmates and friends for their assistance, support, and ideas; particularly Monica Zamora Zapata, Handa Yang, Xiaohui Zhong, Dipak Sahu, Bengu Ozge Akyurek, Mohamed Ghonima, Ben Kurtz, Felipe Mejia, Ryan Hanna, Jose Ortiz Tarin, Isabella Arzeno, and Ingram Vargas. Finally, I am forever grateful for my parents, Evan Wu, Chacha Lin, and Daniel Peroni for their love and support for this journey.

Chapter 2, in full, is a reprint of the material as it appears in Coastal Stratocumulus Cloud Edge Forecasts" (E. Wu, R. E. S. Clemesha, and J. Kleissl) published in Solar Energy, 2018. The dissertation author was the primary investigator and author of this paper.

Chapter 3, in full, is a reprint of the material in the conference paper "Observation-Based Analog Ensemble Solar Forecast in Coastal California" (E. Wu, M. Zamora Zapata, L. D. Monache, and J. Kleissl) in 46th IEEE Photovoltaic Specialists Conference (PVSC), 2019. The dissertation author was the primary investigator and author of this paper.

Chapter 4, in full, is a reprint of the material as it is expected to appear in "On the Parameterization of Convective Downdrafts for Marine Stratocumulus Clouds" (E. Wu, H. Yang, J. Kleissl, K. Suselj, M. J. Kurowski, and J. Teixeira) in Monthly Weather Review. The dissertation author was the primary investigator and author of this paper.

Chapter 5, in part, is being prepared for publication titled "Sensitivity to the Parameterization of Convective Updrafts and Downdrafts in Marine Stratocumulus Clouds" (E. Wu, J. Kleissl, K. Suselj, M. J. Kurowski, and J. Teixeira). The dissertation author was the primary investigator and author of this paper.

VITA

2014   Bachelor of Science, University of Washington

2016   Master of Science, University of California San Diego

2020   Doctor of Philosophy, University of California San Diego

PUBLICATIONS

Wu, E., Kleissl, J., Suselj, K., M. J. Kurowski, & J. Teixeira (2019). Sensitivity to the Parameterization of Convective Updrafts and Downdrafts in Marine Stratocumulus Clouds. In preparation.

Wu, E., Yang, H., Kleissl, J., Suselj, K., M. J. Kurowski, & J. Teixeira (2019). On the Parameterization of Convective Downdrafts for Marine Stratocumulus Clouds. Monthly Weather Review, in revision 12/2019.

Yang, D., **Wu**, E., & Kleissl, J. (2019). Operational solar forecasting for the real-time market. International Journal of Forecasting, 35(4), 1499-1519.

Wu, E., Zapata, M. Z., Monache, L. D., & Kleissl, J. (2019). Observation-Based Analog Ensemble Solar Forecast in Coastal California. 46th IEEE Photovoltaic Specialists Conference (PVSC).

Wu, E., Clemesha, R. E. S., & Kleissl, J. (2018). Coastal Stratocumulus cloud edge forecasts. Solar Energy, 164(September 2017), 355-369.

ABSTRACT OF THE DISSERTATION

Development of stratocumulus cloud modeling in coastal California for solar forecasting

by

Elynn Wu

Doctor of Philosophy in Engineering Sciences (Mechanical Engineering)

University of California San Diego, 2020

Professor Jan Kleissl, Chair

Solar energy integration into the power grid requires forecasting of solar power due to the natural variability of solar irradiance, primarily due to clouds. Recently, rooftop solar photovoltaic (PV) installations have grown dramatically in California, with a majority of these systems concentrated near the densely-populated coast. A common weather phenomena in coastal California are vast sheets of convective low clouds called Stratocumulus (Sc) clouds. The formation and dissipation of Sc clouds greatly impact solar power production.

The challenges surrounding the modeling of Sc clouds come from the complex interplay among the governing physics– namely, surface-driven convection, cloud-top triggered convection, microphysical processes, and entrainment across the inversion layer. This thesis uses tools

including satellite images, statistical analysis, and numerical weather prediction (NWP) models to predict Sc clouds and generate solar irradiance forecast. First, a novel approach of tracking the evolution of stationary clouds to produce short-term solar forecast using satellite images is presented. The method predicts Sc dissipation time accurately by overcoming the limitation of the frozen cloud assumption in traditional cloud motion vector satellite solar forecasting techniques. Second, an observation-based analog ensemble forecast is investigated to better understand the meteorological variables contributing to Sc cloud lifetime. Intra-day analog ensemble solar forecasts suggest that boundary layer averaged heat, moisture, and height are key to capturing Sc dissipation time. Finally, Sc forecast beyond intra-day is investigated through the use of a numerical weather prediction model– Weather Research and Forecasting (WRF). In WRF, the planetary boundary layer (PBL) scheme parameterizes mixing processes in the PBL that impact the heat and moisture profile in the PBL. An eddy-diffusivity/mass-flux (EDMF) framework is adopted to model realistic mixing in the PBL. The framework models the non-convective environment through eddy-diffusivity and the convective area using a mass-flux. Specifically, cloud-top triggered downdrafts are developed and integrated into the mass-flux model. Turbulent downdrafts help mix the heat and moisture in the top part of the PBL and result in better representation of thermodynamic profiles and cloud thickness.

Chapter 1

Introduction

1.1 Background

Stratocumulus (Sc) clouds are one of the most common cloud types on Earth (Wood, 2012). They have a strong negative radiative impact on the Earth's energy budget because they strongly reflect incoming solar radiation and have very little effect on outgoing longwave radiation. They form under strong temperature inversions and are commonly seen off the western coast of continents in the mid-latitudes, making them a familiar cloud to a large population. The distinct overcast feature of Sc earn them the nickname "May Gray", "June Groom", and "Fogust" to many residents in coastal California. Sc clouds have been the topic of research for many years because of their prevalence to the Earth's climate, weather, and energy budget. They impede visibility to negatively affect air traffic (Reynolds et al., 2012), and they also impact solar power integration into the electric grid. As a result, accurate modeling of Sc clouds is of high importance.

In the state of California, due to its aggressive renewable mandate, high electricity prices, and decreasing solar system costs, more than one million rooftop solar photovoltaic (PV) systems have been installed during the last two decades. Since a majority of rooftop PV systems are located along the densely-populated coast of California, an accurate forecast of Sc clouds is ever

more important as they greatly reduce the solar power production. Traditionally, solar forecast rely on different systems depending on the forecast horizon. For short-term solar forecast up to about 5 h ahead, imagery-based cloud advection techniques are used, such as cloud motion vectors (CMV) from satellite images (Perez et al., 2010). Imagery-based CMV techniques assume "frozen" clouds to move in the direction of the regional wind field. While the assumption is valid for a few hours, it becomes inaccurate for longer time horizon. For longer-term solar forecast, ranging from hours-ahead to days-ahead, physics-based numerical weather prediction (NWP) is used (Jimenez et al., 2016, Mathiesen and Kleissl, 2011). NWP leverages current weather observations in the model initialization and then integrates a set of primitive equations numerically in time to produce the forecast. Due to computational constraints, state-of-the-art NWP models have limited spatial and temporal resolution and can lead to erroneous representation of clouds. Another set of forecast systems– statistical solar forecast– build upon existing forecast and perform statistical post-processing to improve the overall forecast accuracy.

While CMV and NWP successfully predict many weather conditions, they often struggle for stratocumulus-topped boundary layer (STBL). This is because the physical processes governing STBL are complex and often range in spatial and temporal scales, making the modeling of Sc clouds difficult. On the one hand, large scale subsidence sets up the strong temperature inversion and is a result of the descending branch of the Hadley cell, where the circulation is on the order of $O(10km)$. The strength of subsidence determines how warm and dry the free troposphere is and has a direct effect on Sc cloud lifetime. On the other hand, entrainment takes place at the interface of the cloud-top and the free troposphere, within a layer of $O(10m)$. Between these largest and smallest scales several important processes occur on scales on the order of typical STBL height ($O(1km)$). At the surface, sensible and latent heat fluxes provide warm and moist air into STBL and are often considered in the form of rising plumes. At the cloud-top, radiative and evaporative cooling initiates cooled downdrafts, and entrainment also interacts with these downdrafts. Together updrafts and downdrafts drive turbulence and transport

surface and cloud-top properties throughout the STBL. Wind shear at the surface also generates turbulence for STBL. Because of the strong turbulence, the STBL is coupled from the surface up to cloud-top, leading to well-mixed profiles in liquid conserved potential temperature and total water mixing ratio. During the day, solar radiation heats the cloud layer and often leads to thinning or dissipation of Sc clouds. Finally, drizzle also contribute to the thinning of Sc clouds. The interplay of the aforementioned processes ultimately determine the fate of Sc clouds. The following paragraph describes how these physical processes limit the forecast accuracy of CMV and NWP techniques and novel algorithms that I have developed to improve forecasts of the STBL.

1.2   Overview of the Dissertation

In this dissertation, tools including satellite images, statistical models, and numerical weather prediction (NWP) models are used to model Sc clouds and generate solar irradiance forecast in coastal California. First, short term forecast using satellite imagery are used. Since Sc clouds do not normally follow the synoptic wind direction, the "frozen" cloud technique in CMV breaks down and leads to false Sc cloud advection (Miller et al., 2017). In coastal California, Sc clouds often form at night and reach maximum coverage before sunrise. During the day, solar heating at the surface and entrainment of warm and dry air from the free troposphere cause Sc clouds to dissipate. With these physical insights in mind, a novel approach to track the evolution of stationary clouds and produce solar forecast using satellite images is proposed in Chapter 2. This differs from CMV approaches where only advection of frozen clouds is considered.

Another approach to leverage physical insights is in the form of statistical post processing or data-driven approaches. Data-driven approaches predict the future based on past relationships in the input and output data. In Chapter 3 an observation-based analog ensemble (AnEn) solar forecast illustrates the usefulness of combing physical and statistical insights.

While observation-based AnEn is useful for intra-day forecast, the accuracy suffers with increasing forecast lead time. For longer-term forecast, accurate NWP output is an invaluable input to statistics-based models. The Weather Research and Forecasting (WRF, Skamarock et al. (2019)) is an open-source community NWP model used in research and in operational settings. WRF consists of two major components: a dynamical solver and model physics. The dynamical solver consists of numerical techniques to solve the fully-compressible, Eulerian nonhydrostatic equations. Prognostic variables include velocity components, perturbation moist potential temperature, perturbation geopotential, and perturbation dry-air surface pressure. Scalars such as water vapor mixing ratio, cloud water mixing ratio, and chemical species may also be included. The model physics are parameterizations aimed to represent processes that are complex and difficult to resolve. They include microphysics, cumulus, land-surface interaction, planetary boundary layer (PBL), and radiation. Specifically, the vertical sub-grid fluxes parameterized by PBL schemes play a critical role in Sc cloud maintenance and dissipation. Chapter 4 and Chapter 5 focus on PBL parametrization in WRF for Sc modeling.

Chapter 2

Coastal Stratocumulus cloud edge forecasts

2.1   Introduction

Stratocumulus (Sc) clouds are the most common cloud type on Earth, with an annual mean coverage of 22% for the ocean surface and 12% for the land surface (Hahn and Warren, 2007). Sc clouds strongly reflect incoming solar radiation. Due to their low cloud height they emit a similar amount of outgoing longwave radiation as the surface. Therefore, Sc clouds have a strong net negative radiative effect on the Earths radiative balance (Hartmann et al., 1992, Wood, 2012). Sc clouds form in a shallow planetary boundary layer and are capped by a strong temperature inversion. The inversion limits the vertical mixing of warm dry air above, and cool moist air beneath (Klein and Hartmann, 1993), which keeps the clouds from evaporating. Geographically, the highest Sc cloud land coverage is found in the mid-latitude coastal region next to eastern boundary currents (Wood, 2012), where the temperature inversion in this region is associated with the warm dry descending branch of the Hadley cell.

Coastal California is an area of high Sc cloud coverage during the late spring and summer months when the semi-permanent North Pacific High has the greatest intensity (Clemesha et al., 2016). Sc clouds greatly influence the weather, water, and energy of the ecosystem and have

been a topic of extensive research for many years (e.g. Beer and Leopold, 1947, Iacobellis and Cayan, 2013, Johnstone and Dawson, 2010, Williams et al., 2015). In recent years, an aggressive renewable energy mandate in the state of California has attracted more than half a million rooftop solar photovoltaic (PV) installations. As solar PV becomes an important source of generation to the grid, it is critical for the utilities and system operators to maintain reliable service while maximizing solar energy utilization (Denholm et al., 2016). With a majority of rooftop solar PV along the densely-populated coast of California, an accurate forecast of Sc clouds during the summer months becomes important as these clouds reduce solar irradiance substantially.

Two types of methods are traditionally used in solar irradiance forecasting depending on the forecast horizon. For short-term solar forecasting, imagery-based cloud advection is used. Ground-based sky imager systems are used for intra-hour forecasting (Chauvin et al., 2016, Chow et al., 2011, Dev et al., 2017, Huang et al., 2013a, Peng et al., 2015, Yang et al., 2014), while satellite cloud motion vectors (CMV) are used for forecasting up to 5-hour ahead (Perez et al., 2010). Traditional image-based cloud advection assumes "frozen" clouds to move in the direction of the regional wind field. While this assumption generally holds true for a few hours, it loses validity for longer term forecast. For longer-term solar forecasting, ranging from hours-ahead to days-ahead, physics-based numerical weather prediction (NWP) is used (Jimenez et al., 2016, Lara-Fanego et al., 2012, Mathiesen and Kleissl, 2011). NWP uses current weather observations to solve a set of primitive equations and numerically integrate the weather forward in time. Forecast accuracy varies considerably depending on the time, location, and weather condition. Perez et al. (2010) found that hourly-averaged satellite CMV forecast mean bias error (MBE) and root mean square error (RMSE) on an annual basis range from 0.2 W m^{-2} and 104 Wm^{-2} in an arid region like Desert Rock, NV to 30 Wm^{-2} and 159 Wm^{-2} in a semi-arid elevated place like Boulder, CO. Mathiesen and Kleissl (2011) found that NWP models generally under-predict cloudy conditions, resulting in an over-prediction of solar irradiance. Recent studies have combined satellite images and NWP to better improve short-term solar forecasting (Arbizu-Barrena et al., 2017, Lee et al.,

2017). For example, in addition to using traditional CMV techniques, Arbizu-Barrena et al. (2017) use a NWP to allow both advection and diffusion to the cloud index derived from Meteosat Second Generation. It is shown that this technique outperforms traditional CMV in areas with low topographic complexity, but struggles in areas where cloud patterns are influenced by the terrain, as is the case for coastal California.

NWP forecasts of Sc clouds in coastal California have been improved through better cloud initialization (Mathiesen et al., 2013, Yang and Kleissl, 2016) or by modifying inversion base height in NWP to better represent the clouds (Zhong, 2017). Imagery-based cloud advection forecasts have received less attention. Traditional satellite CMV forecasts do not accurately predict how Sc clouds move or dissipate in time largely because Sc clouds do not typically follow the synoptic wind direction. An example of false Sc cloud advection by traditional satellite CMV forecast has recently been reported by Miller et al. (2017). Sc clouds over land often form at night and reach their maximum coverage before sunrise. During the day, Sc clouds dissipate because of solar heating at the surface (and the resulting surface sensible heat flux), solar heating of the cloud, and entrainment of drier warmer air from aloft (Ghonima et al., 2016). As dissipation of Sc clouds is not considered, frozen cloud advection in satellite CMV often under-predicts solar irradiance.

The objective of this paper is to improve solar irradiance forecasting during Sc cloud days primarily through quantifying the dissipation time of Sc clouds. A Sc cloud edge forecast (hereinafter called "line forecast") using the Geostationary Operational Environmental Satellite (GOES) is proposed to improve solar irradiance forecasting by allowing for Sc cloud dissipation. The forecast is based on tracking the most inland edge of Sc clouds. The novelty of the method is that it can track evolution (dissipation in this case) of a stationary cloud, while standard cloud motion approaches only consider advection of frozen clouds. The method combines physical insights into lower atmospheric cloud top heights under a strong inversion with statistical methods. While applied here to Sc cloud forecasting in California, we expect the cloud edge tracking to be

equally valid for other overcast stationary clouds such as coastal Sc cloud forecasts elsewhere and inland fog forecasts. For example, fog and low stratus in Germany pose a challenge for the transmission system operators. In addition to the low stratus risk forecast system designed for day-ahead warnings (Kohler et al., 2017), line forecasts for short-term forecasting could also help support the decision makings.

This paper is organized as follows. Section 2.2 explains the conceptual motivation and assumptions of the line forecast 2.2.1, followed by a description of Sc cloud dissipation time and cloud thickness evolution (2.2.2 and 2.2.3). Then error metrics are presented in Section 2.2.4. Section 3 contains input data (2.3.1 and 2.3.2), case study setup (2.3.3), and validation sites and data (2.3.4). Section 2.4 contains the validation results and discussion. Validation of assumptions are investigated in 2.4.1 , followed by validation against satellite observations (2.4.2), and discussion of geographical error distributions (2.4.2). Finally, Section 2.5 provides conclusions.

2.2   Methods

2.2.1   Cloud edge line forecast conceptual motivation and assumptions

In coastal California, the Sc cloud eastern (inland) boundary edge elevation is typically found to be at a maximum during the early morning and then decreases in time. Conceptually, clouds thicken and spread at night due to longwave cooling, but start to thin when longwave radiative cooling is balanced by solar heating, which occurs shortly after sunrise (Akyurek and Kleissl, 2017). In southern California, the terrain rises nearly monotonically and peaks at about 1.5 km elevation 40 to 80 km inland. The eastern boundary of Sc clouds usually follows isolines of land elevation. Iacobellis and Cayan (2013) showed that the inland penetration of Sc clouds is limited by the height of the inversion base and coastal topography. In other words, Sc clouds extend inland up to where the land elevation reaches the inversion base height, and the inversion

8

base height equals the cloud top height. Dissipation of Sc clouds occurs after sunrise, often following land elevation as the mass of air required to be heated in order to become cloud-free decreases with increasing elevation.

The line forecast employs the correlation between land elevation and the Sc cloud eastern boundary, by extrapolating the evolution of cloud edge elevation in time to predict the future cloud edge location. The line forecast assumes: (i) constant inversion height (and cloud top height) along the cloud edge; (ii) a constant rate of decrease in the cloud edge boundary elevation; (iii) an exponential increase in the ratio of GHI to clear sky GHI (clear sky index, k_t) from sunrise to one when the clouds dissipate; and (iv) no satellite parallax effect. Assumptions (ii) and (iii) will be tested in Section 2.4.1. Rastogi et al. (2016) investigated the inversion base height at San Diego Miramar (NKX: 32.85°N, 117.115°W), Vandenberg Air Force Base (VBG: 34.75°N, 120.56°W), and the northern Channel Islands (approximately 34°N, 120°N) during 19652015 using radiosonde data and the Modern-Era Retrospective Analysis for Research and Applications (MERRA) (Rienecker et al., 2011). While radiosonde data showed that inversion height is generally 100 m lower at VBG than NKX, MERRA data showed nearly identical inversion base height for the three points. Although radiosonde data showed differences between VBG and NKX, the lack of spatial coverage made it hard to determine the inversion height everywhere in the domain. As such, assumption (i) was treated as valid for this study. As the GOES satellite is at a zenith angle of approximately 43 degrees and 50 degrees in the southern and northern end of California, the projection of the cloud edge on the surface will be displaced horizontally by tan (zenith angle) times cloud top height above ground level. However, because average cloud top heights are only 400 m above mean sea level the parallax error is small relative to the scales of terrain elevation changes and the horizontal resolution of the satellite images.

2.2.2 Cloud Dissipation Time

The GOES visible channel captures a new image every 15 min. At each satellite image time stamp, a visible reflectance cloud test (Iacobellis and Cayan, 2013) is performed, and the eastern boundary of Sc clouds with its corresponding land elevation are extracted. The median land elevation of all the points over the boundary is used to represent the elevation at each time step. Any missing satellite images are ignored. The time step of the line forecast model is every 15 min. An example of the Sc cloud inland boundary moving towards lower land elevation is shown in Figure 2.1. The median land elevation of the boundary as shown in Figure 2.1 decreases from 900 m at 0700 to 370 m at 1000 PST. Pacific Standard Time (PST) lags Coordinated Universal Time (UTC) by 8 h and will be used for the remainder of this study. Figure 2.2 shows the step by step approach used to issue a Sc cloud line forecast for this day. A time series of the boundary median elevation is shown in Figure 2.2b. Note that the accuracy of the line forecast is limited by the number of visible images available. While the forecast issued at 0800 PST is accurate for this day, at 0700 PST the line forecast would not be able to accurately predict the cloud dissipation. Only two elevation points were available by 0700 PST, and the extrapolation of these median land elevation would result in clouds persisting for the whole day.

To predict when Sc clouds will dissipate at a given location, a linear regression is performed on a time series of the points corresponding to the Sc cloud eastern boundary land elevation (Figure 2.2b) and extrapolated in time to the elevation for the given location. A linear regression is chosen empirically, and this assumption will be tested in the next section. The method uses a least square linear fit. It is hypothesized that the time when the predicted cloud edge elevation reaches the elevation of the specified surface location is the time when Sc clouds dissipate:

$$t_{clear} = \frac{E_{site} - a}{b}, \qquad (2.1)$$

where t_{clear} is the cloud dissipation time, E_{site} is the land elevation of the site of interest, and a

10
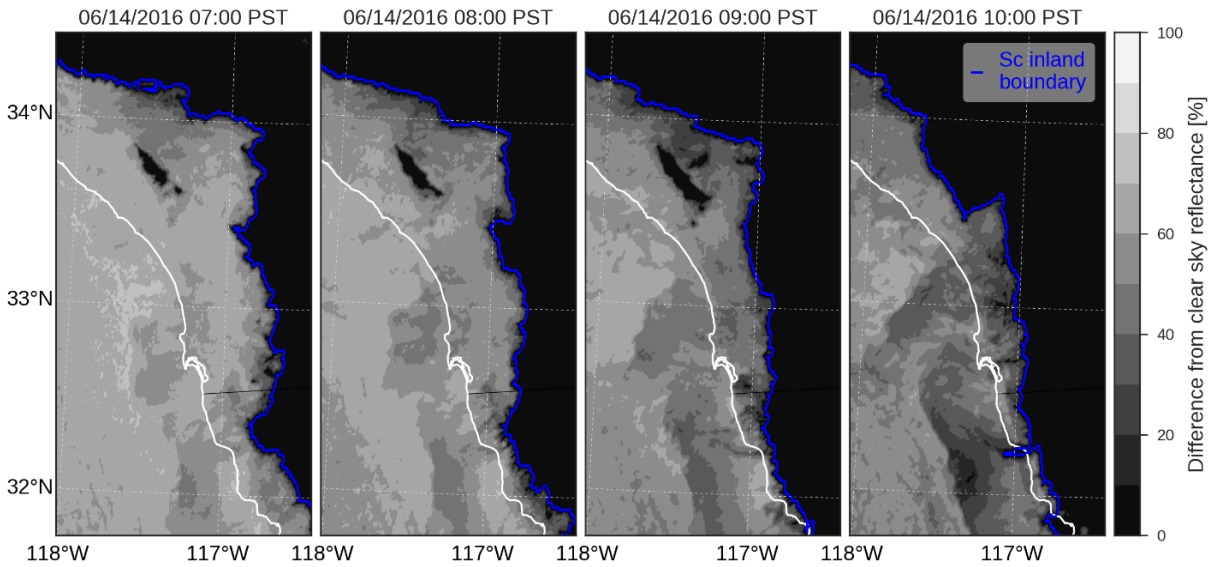
Figure 2.1: GOES visible images at 0700, 0800, 0900, and 1000 PST on June 14, 2016 with Sc cloud inland boundary highlighted in blue. Raw images are post-processed such that pixels within 15.5% of their clear sky reflectance are plotted as dark (clear), while pixels with larger than 15.5% difference are plotted in grey scales (cloudy). Threshold value of 15.5% was previously tested and finalized (see Text S1 in Clemesha et al. (2016)). The position of the boundary advances towards the coast from 0700 to 1000 PST. Note that Santa Ana Mountains (33.70°N, 117.50°W) are clear because the land elevation is above the inversion base height.

11
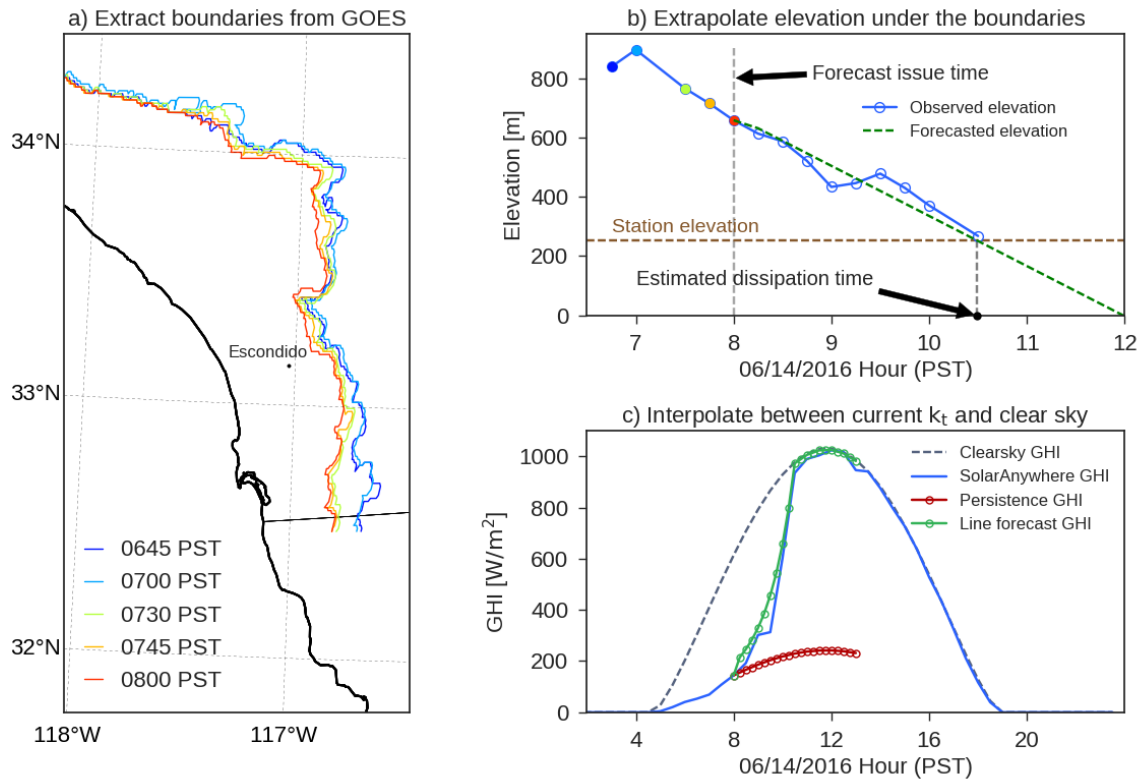
Figure 2.2: Steps to issue a cloud edge or the line forecast at 0800 PST for Escondido with a land elevation of 250 m: (a) Extract Sc cloud inland boundary in consecutive GOES images up to 0800 PST and record the median land elevation under the colored lines (between 32.5°N and 34.5°N). (b) Extrapolate the median land elevation in time using a best fit line through 0645 to 0800 PST. Cloud dissipation time is when the forecasted elevation intercepts with the station elevation (here approximately at 1030 PST). (c) Interpolate between current kt at 0800 PST and clear sky kt at cloud dissipation time using the exponential function described in Section 2.3. The green line in (c) is the line forecast issued at 0800 PST with a 15-min time resolution.

12

and b are the intercept and slope from the least square linear fit.

2.2.3 Cloud Thickness Evolution

To describe the cloud thickness evolution between forecast issue time and dissipation time, the clear-sky index (k_t) is interpolated using an exponential function between forecast issue time and dissipation time to represent the thinning of Sc clouds:

$$k_t^* (t^*) = ae^{bt^*} + c, \qquad (2.2)$$

where a, b, and c are constant coefficients. k_t^* and t^* are normalized k_t and time as defined later in Eqs. 2.3 and 2.4. Physically, when the sun angle is low (early morning), not much heat is received at the surface and the thickness of the clouds is approximately constant. As the day progresses, solar heating increases drastically, and the cloud thickness decreases successively quicker. As such, an exponential function is chosen.

The clear sky irradiance model from Perez et al. (2002) is used to compute k_t. To determine the coefficients for the fitted exponential function, the coastal low cloudiness dataset from Clemesha et al. (2016) is used. The dataset was created using GOES images from 1996 to 2016 with a spatial resolution of 4 km and a temporal resolution of 30-minutes. Historical days within the dataset when Sc clouds are present are identified. The corresponding SolarAnywhere (2019) data, a satellite solar irradiance product, are extracted to determine the exponential function that best describes the increase in k_t from sunrise to cloud dissipation time. SolarAnywhere data are available from 2003 to 2016, and only the overlapped time period between the coastal low cloudiness dataset and SolarAnywhere are used. Note that 2016 is excluded in this analysis as it will be used to validate the forecast (Section 2.4.1). June and August are selected in southern and central and northern California, respectively, as they represent the respective months with the most dominant marine layer cloud influence (Clemesha et al., 2016). A map of southern and

central and northern California domain is shown in Figure 2.3.
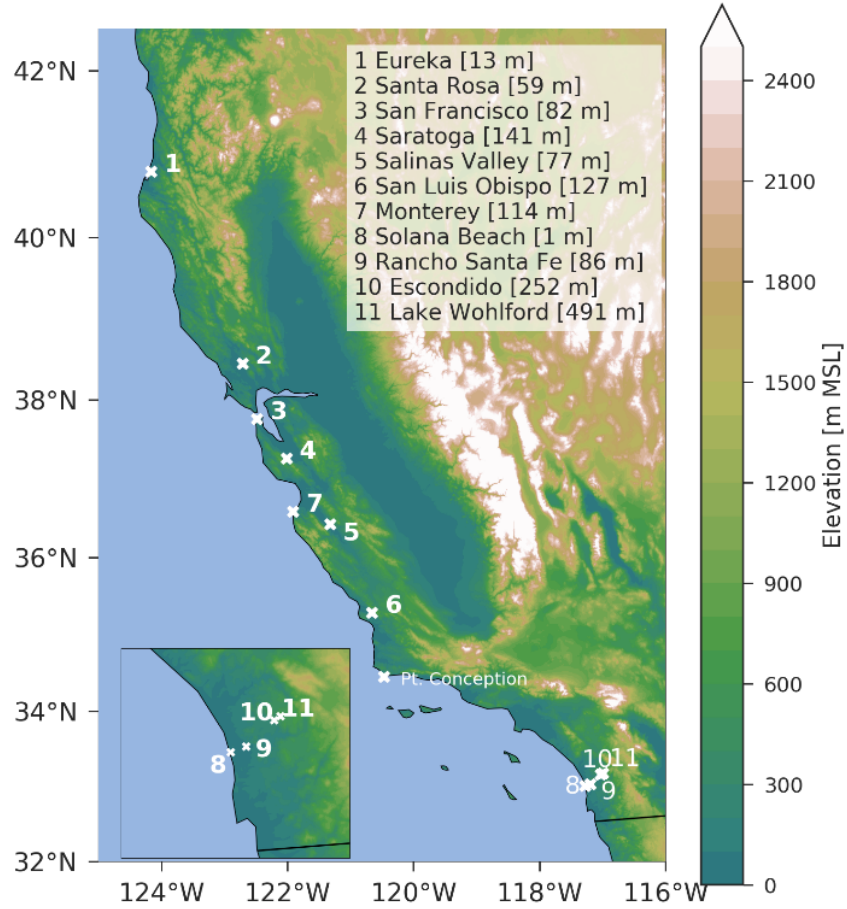
Figure 2.3: Elevation map showing validation site locations. Specific site elevations are given in the legend. The cut-off of southern California from central and northern California is around Pt. Conception, all southern California stations are shown in the inset.

Time stamps are scaled by the time difference between sunrise and cloud dissipation time:

$$t^* = \frac{t - t_{sunrise}}{t_{clear,obs} - t_{sunrise}}, for\, t_{sunrise} \leq t \leq t_{clear,obs}, \tag{2.3}$$

where $t_{clear,obs}$ is the first time when observed k_t is clear, and $t_{sunrise}$ is the time stamp at sunrise. The observed clear k_t) is defined following Kankiewicz et al. (2014) where clear sky is defined as k_t) greater than 0.8. Sunrise is chosen as the reference time because that is when solar heating starts to thin the cloud deck. Similarly, to normalize different starting k_t at sunrise, k_t for each

Table 2.1: Coefficients of the average of the fitted exponential function in Eqs. 2.2 for central and northern California and southern California (black dashed lines in Figure 2.5) for different sunrise times.

Location	a	b	c
Central and northern California (sunrise at 0600 PST)	0.003	5.959	0.022
Central and northern California (sunrise at 0630 PST)	0.006	5.041	0.022
Southern California (sunrise at 0530 PST)	0.005	5.238	0.014

individual day is scaled by k_t at sunrise:

$$k_t^* = \frac{k_t - k_{t_{sunrise}}}{1 - k_{t_{sunrise}}}, \tag{2.4}$$

where $k_{t_{sunrise}}$ is the clear sky index at sunrise. To avoid picking earlier times where the accuracy of k_t decreases because of difficulty of modeling clear sky irradiance near sunrise, the first daytime point is chosen to be when cosine of solar zenith angle is greater than 0.1. Cosine of solar zenith angles are calculated for all stations shown in Figure 2.3. During the month of June, 0530 PST marks the time when cos (solar zenith angle) is greater than 0.1 for stations in southern California. For central and northern California, 0600 PST marks the time when cos (solar zenith angle) is greater than 0.1 for early August while the time gradually shifts to 0630 PST by late August.

An example of the fitted exponential function at a single site is shown in Figure 2.4. For this study, two sets of coefficients are determined after repeating the analysis for multiple sites. The first set will be used to forecast k_t in central and northern California in August, and the second set will be used to forecast k_t in southern California in June. The coefficients are tabulated in Table 2.1 and the corresponding curves can be seen in Figure 2.5. The stations shown in this analysis will be used as validation sites and will be discussed in greater details in Section 2.3.4.

To produce a time series of forecasted k_t , forecast issue time and future time stamps are scaled following Eqs. 2.3, and cloud dissipation time is calculated following Eqs. 2.1(1). These
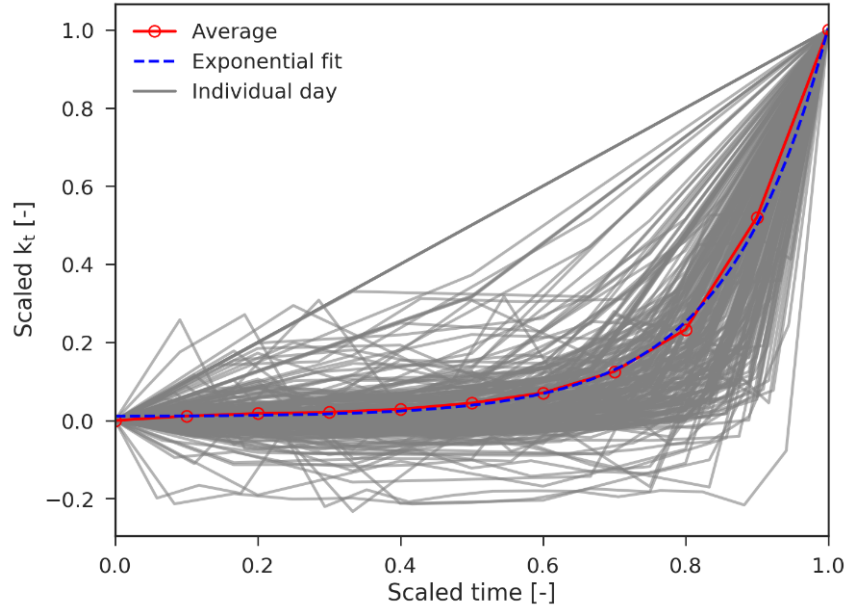
Figure 2.4: Scaled time t* and scaled clear sky index kt* for Sc cloud days in August from 2003 to 2015 at Santa Rosa, CA. The average of the kt* for individual days (red line) is used to fit the exponential function (blue line). Negative k* during the day indicates a decrease of k_t from sunrise.
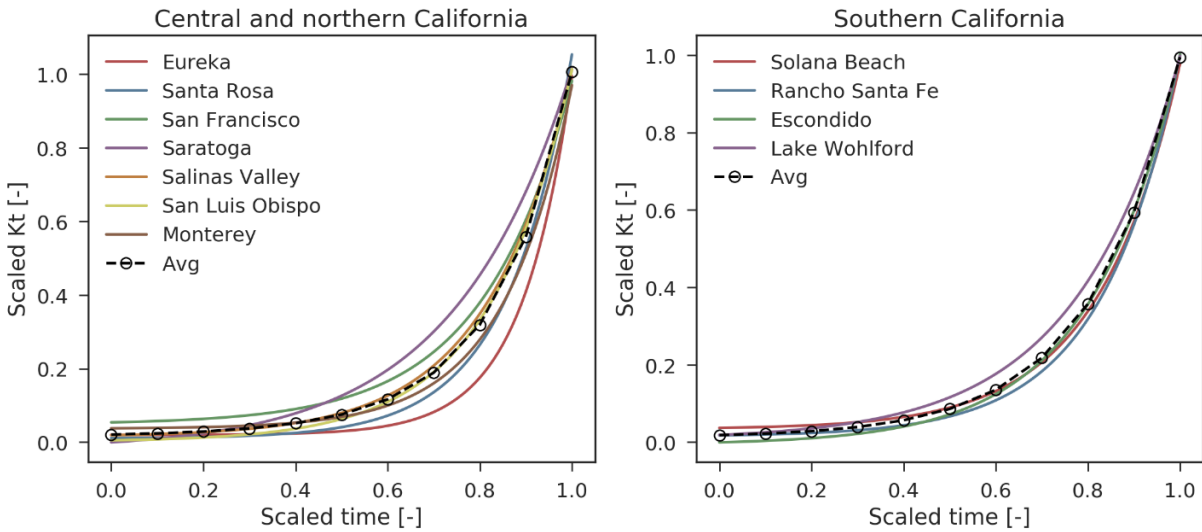
Figure 2.5: The fitted exponential function at each individual station and their average for central and northern (left) and southern California (right). The corresponding coefficients can be found in Table 2.1.

scaled time stamps are then plugged into Eqs. 2.2 to retrieve k_t^*. Lastly, k_t^* is transformed back to k_t by rearranging Eqs. 2.4 and replacing $k_{t_{sunrise}}$ as k_t at forecast issue time t_o:

$$k_t = k_t^* (1 - k_{t,0}) + k_{t,0}. \tag{2.5}$$

This k_t model has the benefit that points that are falsely flagged as cloudy by the line forecast at the forecast issue time (e.g., land elevation is lower than the median land elevation of the boundary yet the pixel is initially clear), are automatically corrected to clear because future k_t is an interpolation between current k_t ($k_{t,0} = 1$ in this case) and clear k_t (i.e., $k_t = 1$). In other words, these points will not be changed to lower k_t and will remain clear.

2.2.4 Error metrics

The error metrics used for validation are mean bias error (MBE), mean absolute error (MAE), and forecast skill (FS):

$$MBE \equiv \frac{1}{N} \sum_{n=1}^{N} x_n - x_n^{obs} \tag{2.6}$$

$$MAE \equiv \frac{1}{N} \sum_{n=1}^{N} |x_n - x_n^{obs}| \tag{2.7}$$

$$FS \equiv 1 - \frac{MAE}{MAE_{persistence}} \tag{2.8}$$

where x_n is the nth forecast of GHI, and x_n^{obs} is the nth observation of GHI. To further quantify the skill of the Sc cloud line forecast, the FS defined by Coimbra et al. (2013) and modified by Yang and Kleissl (2016) is used to intercompare line forecasts against persistence forecasts. Positive values of FS indicate that line forecasts have a lower MAE than persistence forecasts. The maximum value of FS is 1.

2.3 Data and Validation

2.3.1 Elevation data

Land elevation data are obtained from General Bathymetric Chart of the Oceans (GEBCO, 2017) at 30 arc-second intervals (or approximately 1 km). At each time stamp, the land elevation at the cloud boundary is retrieved. Land points below the median cloud boundary elevation are assumed to be cloudy, and the median cloud boundary land elevation is assumed to be decreasing during the day. In other words, non-negative slope b in Eqs. 2.1 are not considered, but such cases are limited to early morning, presumably because solar heating is still weaker than longwave cooling at large solar zenith angles, leading to an initial increase in cloud cover and/or thickness (Akyurek and Kleissl, 2017). On most days, the cloud edge elevation eventually drops to sea level, representing a complete clearing of Sc clouds for the coastal land area. Cloud boundaries over the ocean are ignored as the focus of this paper is solar irradiance forecasts over the land.

Further constraints on the domain are required to avoid assigning far inland points as cloudy because they have a land elevation below the median Sc cloud edge elevation. The topography of coastal California rises steeply near the coast, but then drops to near sea level across the coastal mountain range in the Central Valley and Imperial Valley. In reality, Sc clouds seldom penetrate that far inland as the mountain ranges act as barriers to the airmasses that support Sc clouds. The inland valleys represent arid climates and are mostly clear throughout the summer. To constrain the domain to areas where Sc clouds commonly occur, we filter the points using the 20-year summertime California coastal low cloudiness dataset from Clemesha et al. (2016). Land points with no low cloud occurrence in the 20-year low cloud dataset are removed from the cloud mask. Doing so also assures that the extrapolation of boundary elevation will not include land points with the same land elevation but too far inland (e.g., a land point can be at sea level but located a few hundred kilometers away from the coast). The final coastal domain is shown in Figure 2.6.
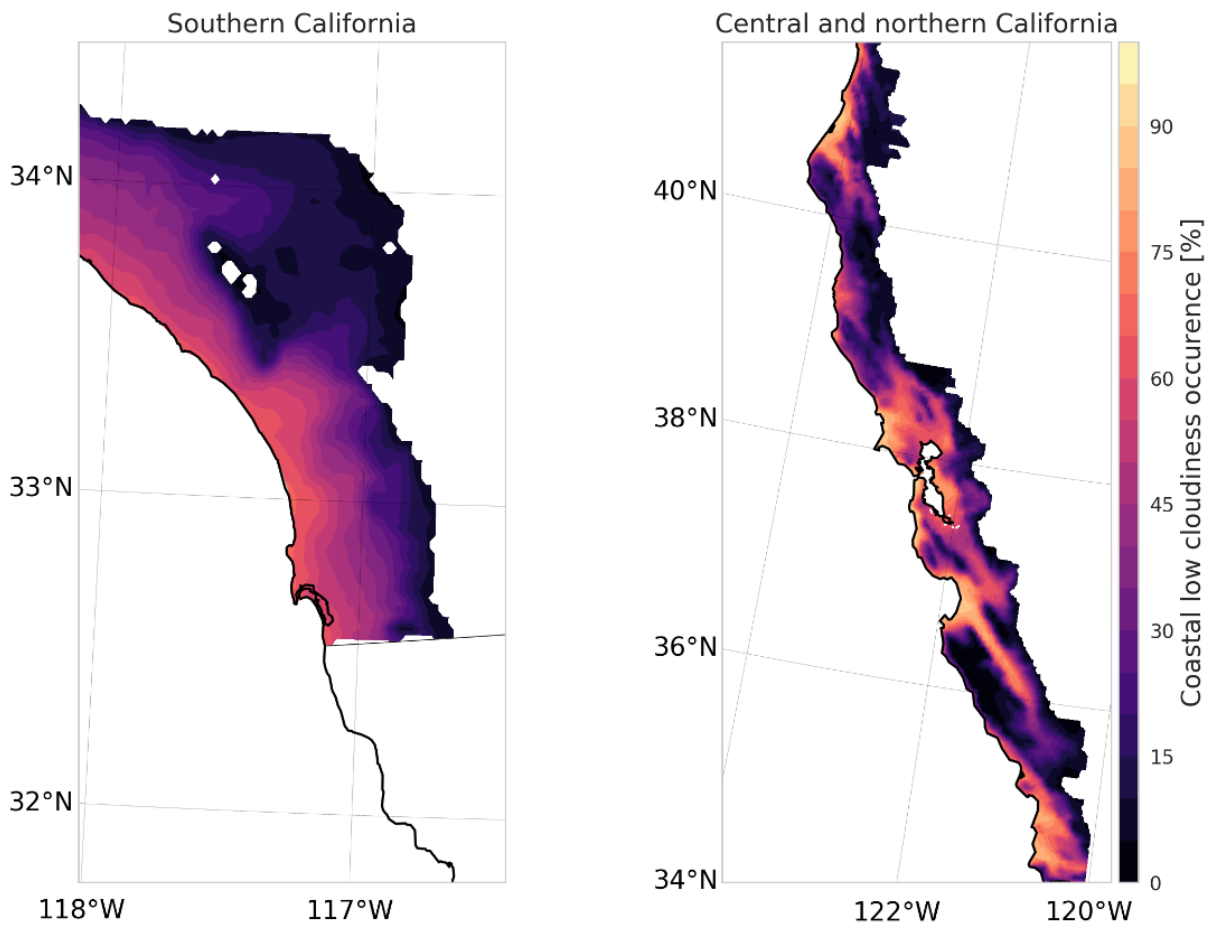
Figure 2.6: California coastal low cloudiness (Clemesha et al., 2016) occurrence is averaged between 0600 and 0800 PST over 20-years for June in southern California and August for central and northern California.

2.3.2 GOES data and cloud edge retrieval

GOES-15 Imager measurements in the visible channel at 1-km resolution are obtained from National Oceanic and Atmospheric Administration (NOAA) Comprehensive Large Array-Data Stewardship System (CLASS). Images are captured every 15 minutes. During the daytime hours, images are missing at 1515, 1015, 1245, and 1315 PST. A post-launch calibration developed at NOAAs National Environmental Satellite, Data, and Information Services (NESDIS, 2017) is applied to the images to account for sensor degradation.

To retrieve clouds from the satellite images, a clear sky or background reflectance is determined by sorting the reflectance from all images at each month and hour and selecting the minimum reflectance at each pixel (Iacobellis and Cayan, 2013). Instead of using the preceding one month of data ($\sim$ 30 images) as was the case in Iacobellis and Cayan (2013), we use the preceding three months of data ($\sim$ 90 images) because it yields a better cloud detection. This method assumes that there is at least one clear day during the three-month window. After obtaining clear sky reflectance for every pixel, a binary cloud mask is turned on every time the pixel reflectance exceeds its clear sky reflectance by 15.5% (Clemesha et al., 2016). Once the cloud mask at each time stamp is determined, the longest consecutive contour line is extracted as the Sc cloud eastern boundary.

2.3.3 Location and time period for the case studies

As mentioned in Section 2.2.3, June and August are the peak months of southern and central and northern California coastal low clouds, respectively. Therefore, the months of June and August 2016 are chosen for southern California and central and northern California for validation, respectively. We quantify days with Sc cloud coverage using the following approach: (1) For the first visible image of the day, at least 10 % of cloud coverage in the coastal low cloudiness product are present over land in each domain. (2) Use the corresponding thermal infrared image

at 10.7 μm to compute scene temperature (i.e., cloud top temperature) following Weinreb and Han (2011). As Sc clouds are low and have relatively uniform cloud top height, the variation in cloud top temperature in the coastal domain is used to exclude days with significant amount of high clouds. After threshold testing, a standard deviation in cloud temperature of 3 % (about 8 K) among the cloudy pixels is chosen. Days with scene temperature standard deviation greater than 3 % are removed. While the standard deviation thresholding removes days with significant multi-level clouds (i.e., both low and high clouds are in the domain), there are some days when the proportion of high clouds is too small to raise the standard deviation above 3% . These days are kept in the dataset, but to avoid misclassifying the cloud edge elevation, land elevation at pixels with scene temperature lower than 280 K are removed. A flowchart to determine when the line forecast should be used is shown in Figure 2.7.

For southern California, a total of 19 days passed (June 1 to 9, 11 to 15, 23 to 25, and 29 to 30) the threshold tests. For central and northern California, a total of 25 days passed (August 1 to 28, excluding August 18, 19, and 22).
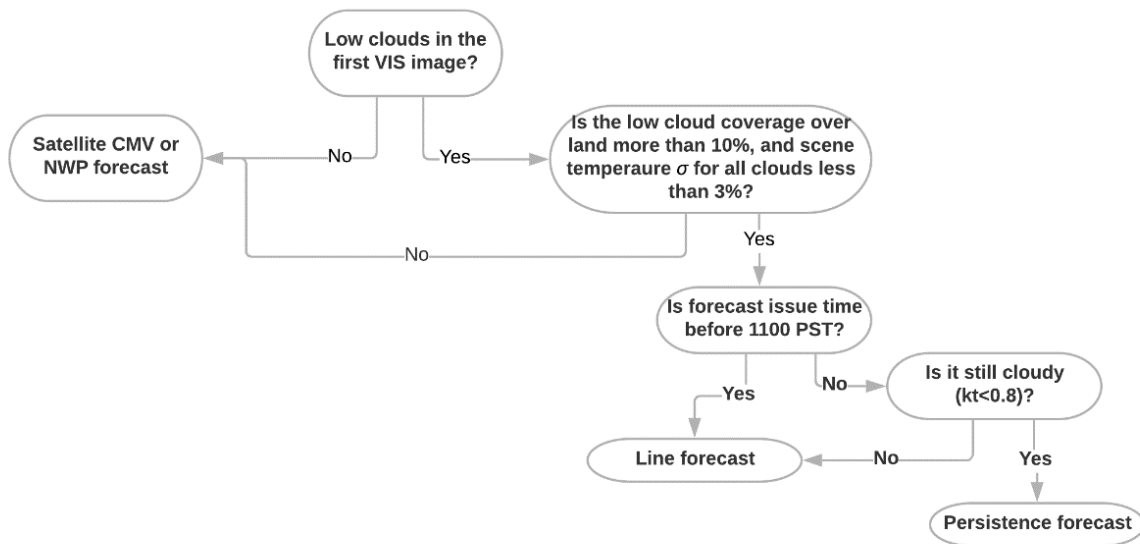
Figure 2.7: Flowchart defining under what conditions line forecasts are applied for coastal California.

Table 2.2: Summary of validation sites in central and northern California. Median Sc cloud burn-off time is obtained from 20 August months (1996-2015) using the coastal low cloudiness product at half hour time resolution.

Station	Eureka	Santa Rosa	San Francisco	Saratoga	Salinas Valley	San Luis Obispo	Monterey
Latitude [°]	40.798	38.447	37.752	37.262	36.427	35.283	36.583
Longitude [°]	-124.163	-122.709	-122.477	-122.013	-121.322	-120.653	-121.906
Elevation [m MSL]	13	59	82	141	77	127	114
Median Sc cloud burn-off time [HHMM PST]	1130	0930	1230	0800	0900	0830	1130

Table 2.3: Summary of validation sites in southern California. Median Sc cloud burn-off time is obtained from 20 June months (1996 – 2015) using the coastal low cloudiness product at half hour time resolution.

Station	Solana Beach	Rancho Santa Fe	Escondido	Lake Wohlford
Latitude [°]	33.007	33.033	33.159	33.178
Longitude [°]	-117.276	-117.189	-117.031	-116.995
Elevation [m MSL]	1	86	252	491
Median Sc cloud burn-off time [HHMM PST]	0900	0830	0800	0800

2.3.4   Validation sites

For the central and northern California case study, seven cities ranging from as far north as Eureka to as far south as San Luis Obispo are chosen as validation sites. Their locations and elevations are tabulated in Table 2.2. The sites are carefully chosen to represent the different challenges in forecasting Sc clouds in different regions.

For the southern California case study with a focus in the greater San Diego area, four sites along a line from coastal to inland are chosen. These four sites are part of the San Diego Gas & Electric (SDGE) weather station network with LI-COR LI200 pyranometers measuring GHI at a 5-minute resolution. Their locations and elevations are tabulated in Table 2.3. A map of all 11 validation sites is shown earlier in Figure 2.3.

2.3.5 Satellite solar resource data

Clean Power Researchs SolarAnywhere (2019) data utilizes GOES images to output solar irradiance by modulating a clear sky irradiance model (Perez et al., 2002). For June 2016, SolarAnywhere data are validated against the SDGE weather stations, with an average hourly MBE of 18 W m^{-2}, MAE of 30 Wm^{-2}, and RMSE of 57 Wm^{-2}. Jamaly and Kleissl (2012) also validated SolarAnywhere data against 52 California Irrigation Management Information System (CIMIS) ground sensors and found similar results an average hourly MBE of 19 Wm^{-2}, MAE of 46 Wm^{-2}, and RMSE of 65 Wm^{-2} over the year 2010. Because the accuracy is comparable to that of a typical ground sensor, accurate under typical conditions to $\pm$ 5 % (CIMIS, n.d.), SolarAnywhere data will be used as observations for validation hereinafter. SolarAnywhere data at 2 km spatial resolution and 30-minute temporal resolution are retrieved for the 11 validation sites.

2.3.6 Satellite cloud motion vector and persistence forecast

For reference, hourly satellite CMV data (Perez et al., 2010) from 1 hour to 5 hours ahead derived from GOES images are computed for the 11 validation sites. For the seven sites in central and northern California, data are available for 1–31 August 2016. For the four sites in southern California, data are only available for 5–15 June 2016. The (smart) persistence forecast uses the clear sky index (k_t) from SolarAnywhere satellite measurements at forecast issue time and assumes fixed k_t out to 5-hours ahead.

2.4 Results and Discussion

2.4.1 Validation of assumptions

Two assumptions described in Section 2.2.1 are tested here. If the Sc cloud boundary elevation decreases at a constant rate, then a linear least-square regression through the elevation points should have a coefficient of determination (R^2) that is close to 1. For each validation day, boundary elevation derived from GOES images between 0630 to 1230 PST ($\sim$ 23 images) as shown in Figure 2.8 are used to fit a linear least-square regression, and the R^2 is recorded. A detailed summary of each validation day can be found in Table 2.4. The average R^2 for the 43 validation days is 0.86, indicating that the slope of boundary elevation is nearly constant. If the boundary does not advance towards the coast and moves around the inland area throughout the day, a low R^2 is found, such as on June 11. Because the median boundary elevation is consistently higher than zero for this particular day, the least-square regression would suggest a burn-off time that is days away from the forecast issue time. As a result, the line forecast acts like a persistence forecast with only a slight increase in k_t for the day.
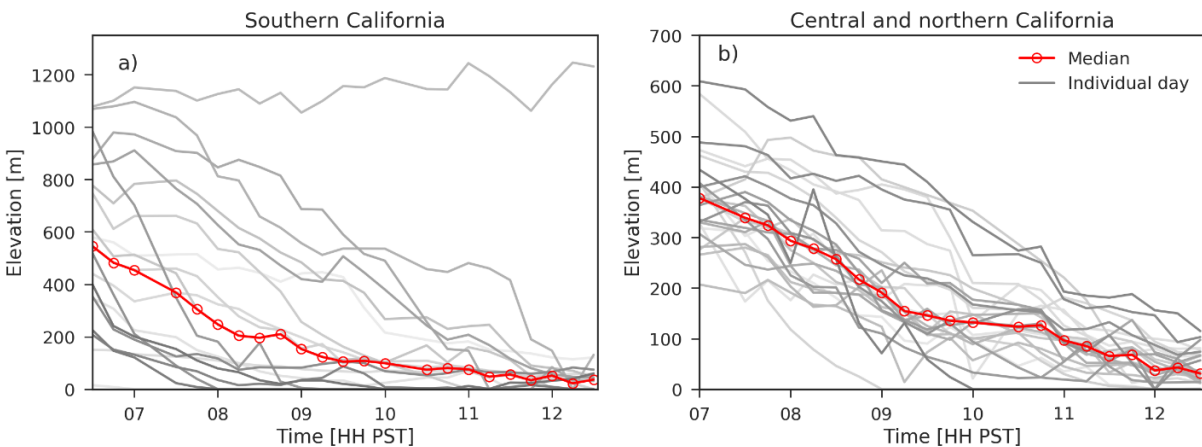
Figure 2.8: Time series of median cloud edge elevation for 19 days from June 2016 in (a) and 25 days from August 2016 in (b). The median edge elevation is shown in red. The cloud edge is detected using GOES data, and the median elevation is obtained from GEBCO.

To verify that morning k_t exponentially increases to clear sky when the clouds dissipate,

Table 2.4: Coefficient of determination for the linear least-square regression through the Sc cloud boundary elevation between sunrise time as determined in Section 2.2.3 and 1230 PST (or until the land is clear, whichever is earlier). Note that June 2016 is for southern California and August 2016 is for central and northern California.

Date	R^2	Date	R^2	Date	R^2	Date	R^2	Date	R^2
1-Jun	0.93	12-Jun	0.91	1-Aug	0.93	11-Aug	0.91	24-Aug	0.83
2-Jun	1.00	13-Jun	0.87	2-Aug	0.88	12-Aug	0.95	25-Aug	0.94
3-Jun	0.69	14-Jun	0.97	3-Aug	0.62	13-Aug	0.76	26-Aug	0.97
4-Jun	0.83	15-Jun	0.90	4-Aug	0.95	14-Aug	0.88	27-Aug	0.98
5-Jun	0.93	23-Jun	0.94	5-Aug	0.97	15-Aug	0.93	28-Aug	0.86
6-Jun	0.88	24-Jun	0.51	6-Aug	0.92	16-Aug	0.92	Average	0.86
7-Jun	0.95	25-Jun	0.59	7-Aug	0.95	17-Aug	0.86		
8-Jun	0.75	29-Jun	0.97	8-Aug	0.98	20-Aug	0.97		
9-Jun	0.96	30-Jun	0.80	9-Aug	0.87	21-Aug	0.89		
11-Jun	0.30	10-Aug	0.94	23-Aug	0.77				

the exponential function with coefficients in Table 2.1 is applied to SolarAnywhere data during June and August 2016. Cloud dissipation time is defined as the first time after sunrise when SolarAnywhere k_t is greater than 0.8. The average of the fitted exponential line is shown in Figure 2.9, and the hourly k_t MAE is tabulated in Table 2.5. Note that this analysis is not a forecast as cloud dissipation time is known. Smaller k_t MAE are found at inland stations, while stations at the immediate coast have larger errors (e.g., Solana Beach, San Francisco, and Monterey). The larger errors are due to ambiguous cloud dissipation time or clouds persisting for the whole day. For example, k_t decreases after the first clear point at San Francisco in Figure 2.9b, and the fitted exponential function is unable to capture any decreasing trend. Similar issues occur in Monterey. All inland stations have hourly k_t MAE less than 0.1, with Escondido, Lake Wohlford and Saratoga having the minimum MAE at 0.04. Overall, the exponentially fitted curves are representative for most validation stations.

Table 2.5: Hourly MAE k_t for the exponentially fitted k_t against actual SolarAnywhere k_t data at all validation stations. The fitted k_t is generated with known dissipation times as the first point where SolarAnywhere k_t ¿ 0.8.

Station	MAE k_t [-]
Solana Beach	0.13
Rancho Santa Fe	0.06
Escondido	0.04
Lake Wohlford	0.04
Santa Rosa	0.01
Saratoga	0.02
Salinas Valley	0.06
San Luis Obispo	0.06
Eureka	0.04
San Francisco	0.17
Monterey	0.12

Table 2.6: Number of days when clouds did not dissipate (i.e., persisting days) in southern California in June 2016 and central and northern California in August 2016.

Station	Persisting days [-]	Number of days considered in Figure 2.9 [-]
Solana Beach	6	19
Rancho Santa Fe	1	19
Escondido	1	19
Lake Wohlford	1	19
Santa Rosa	0	25
Saratoga	0	25
Salinas Valley	0	25
San Luis Obispo	0	25
Eureka	2	25
San Francisco	3	25
Monterey	7	25
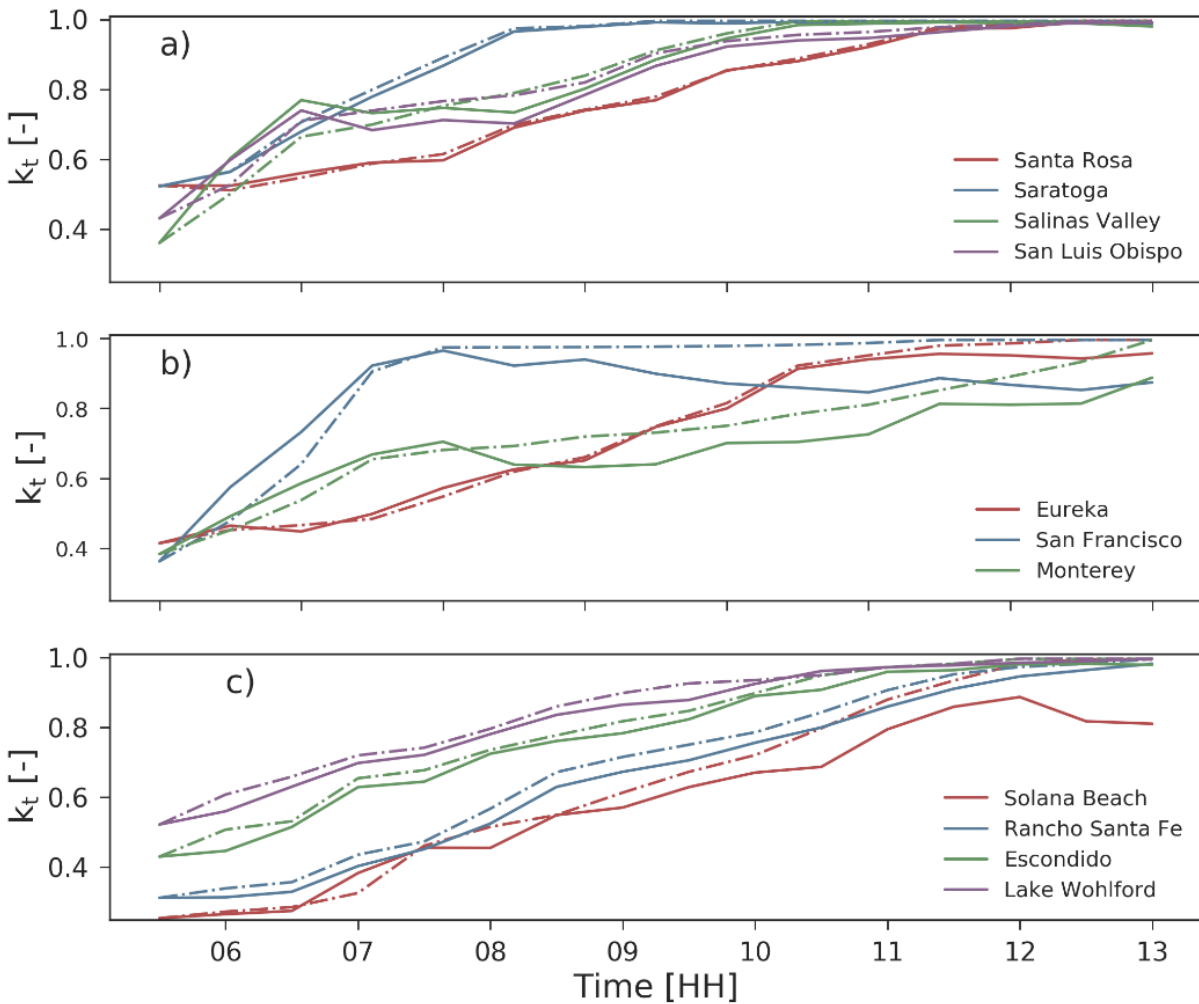
Figure 2.9: Time series of 30-min instantaneous kt from SolarAnywhere averaged over all days with known valid cloud dissipation time (i.e., kt is greater than 0.8). Depending on the station, there are approximately 25 days for (a) and (b) and 19 days for (c); days where kt never exceeds 0.8 are removed. Solid lines are actual SolarAnywhere averages, and dashed lines are the averaged exponential fits using the coefficients in Table 2.1. Note that these are hindcasts with known dissipation time to illustrate the exponential fit function. A breakdown of the number of days when clouds did not dissipate is shown in Table 2.6.

2.4.2 Validation against satellite observations

Southern California

Time series of hourly-averaged GHI are shown in Figure 2.10 for forecasts issued from 0700 to 1000 PST. While the line forecast is computed for all 19 days in June, Figure 2.10 is the average of 5–15 June 2016 because of the availability of satellite CMV forecasts. Forecasts issued after 1100 PST are not of interest as clouds have already dissipated on most days and the line forecast would coincide with persistence forecast with a clear sky index of 1. SolarAnywhere GHI shows that Sc clouds tend to stay longer at the coastal site where land elevation is lower. This is consistent with the assumption that Sc cloud eastern boundary moves towards the coast during the day, and the average land elevation of the boundary decreases.

MBE, MAE, and FS are shown in Figure 2.11. The line forecast consistently performs better than satellite CMV and persistence for all forecast horizon and forecast issue times at Rancho Santa Fe, Escondido, and Lake Wohlford. For Solana Beach, the line forecast is superior to the persistence forecast but slightly worse than satellite CMV. The line forecast has the lowest forecast skill for forecasts issued at 0700 PST. This is likely because only three visible GOES images are available at the time of the forecast issuance. In addition, dissipation often happens several hours after sunrise as seen in Table 2.2 and Table 2.3, making it difficult to forecast the burn-off time several hours ahead. With later forecast issue times, more images are available and the prediction of burn-off time becomes more accurate. Persistence forecasts have the worst error statistics because Sc clouds are present at the forecast issue time, fixing the clear sky index at the forecast issue time results in under-prediction of irradiance. While satellite CMV forecasts out-perform persistence at all four sites, CMV forecasts under-predict the irradiance. As Sc clouds do not follow the direction of the synoptic winds, the assumption of CMV breaks down and results in a cloudy bias.

The coastal topography of San Diego is predominantly north-south oriented, with in-

creasing land elevation from the coast to inland. This simple topographic elevation distribution favors line forecasts because it provides for more consistent meteorological conditions across the forecast domain. For example, (i) absorbed surface irradiance and resulting heating rates are similar due to consistent surface type, (ii) advection is similar due to homogeneous pressure gradients and surface roughness, (iii) microscale meteorological distortions such as local slope flows are avoided, (iv) a straight cloud edge provides for more consistent cloud edge erosion as detailed in the next paragraph. This consistency supports the line forecast assumptions of homogeneous land elevation at the cloud edge and homogeneous rate of change of land elevation at the cloud edge.

Horizontal entrainment of dry air at the cloud edge also plays an important role in the westward movement of the edge. Crosbie et al. (2016) found that the horizontal entrainment at the interface between clear skies and the cloud edge produces evaporatively cooled downdrafts and accelerates the erosion of the cloud edge. In southern California, the cloud edge is relatively straight (north-south) because of the distribution of land elevation. Therefore, horizontal entrainment does not produce as much inhomogeneous mixing as would be the case if the cloud edge was curved and the clear region was not just on one side of the edge. Because of relatively homogeneous lateral mixing and dominant Sc cloud dissipation due to solar heating, the line forecast exhibits significant error reductions compared to persistence and satellite CMV forecasts in southern California.

Central and northern California

The time series of hourly-averaged GHI from the 25 valid days in August 2016 is shown in Figure 2.12. MBE, MAE, and FS are shown in Figure 2.13. The line forecasts perform better than persistence forecasts at 5 out of 7 sites, and the number drops to 4 when compared to satellite CMV forecast. Unlike the four sites in southern California (Figure 2.10), more complex terrain makes forecasting the dissipation time of Sc clouds using the line forecast method difficult. This
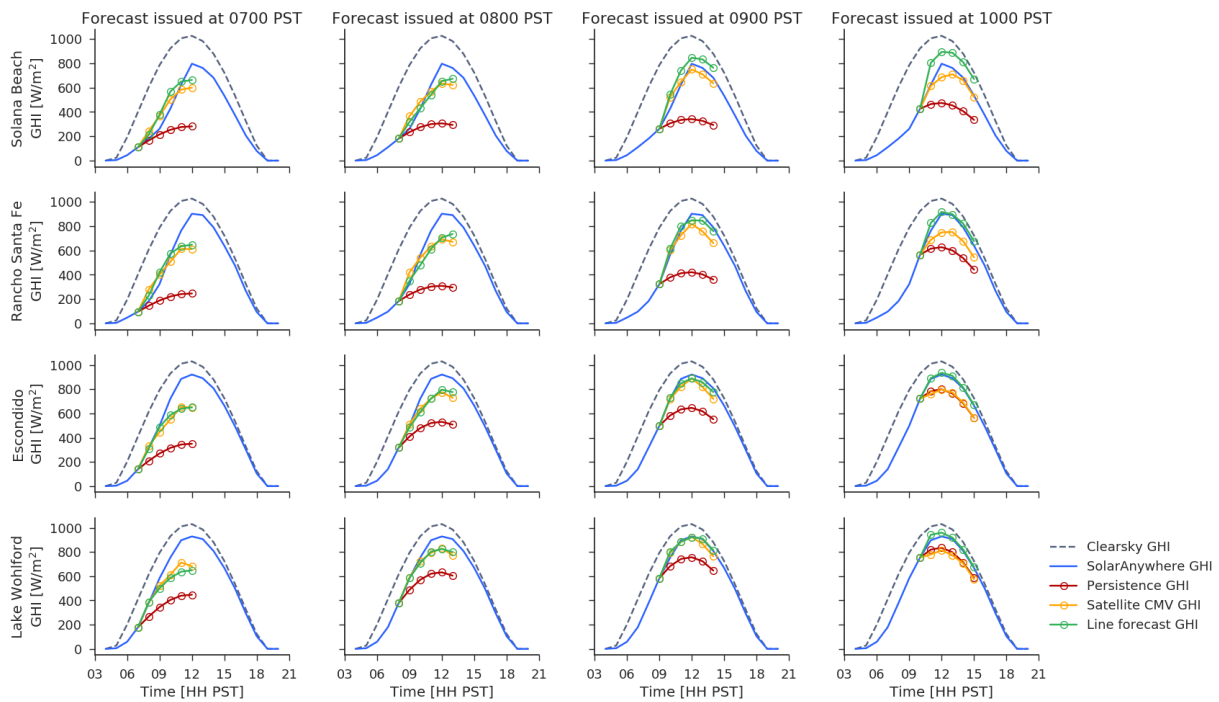
Figure 2.10: Hourly average of forecasted and satellite observed GHI for 5-15 June 2016 at Solana Beach, Rancho Santa Fe, Escondido, and Lake Wohlford. Each column represents a different forecast issue time. Note that each circle indicates the irradiance instantaneously at the hour, with the first circle corresponding to the real-time measured data, the second circle being the 1-h ahead forecast, and the sixth circle being the 5-h ahead forecast.
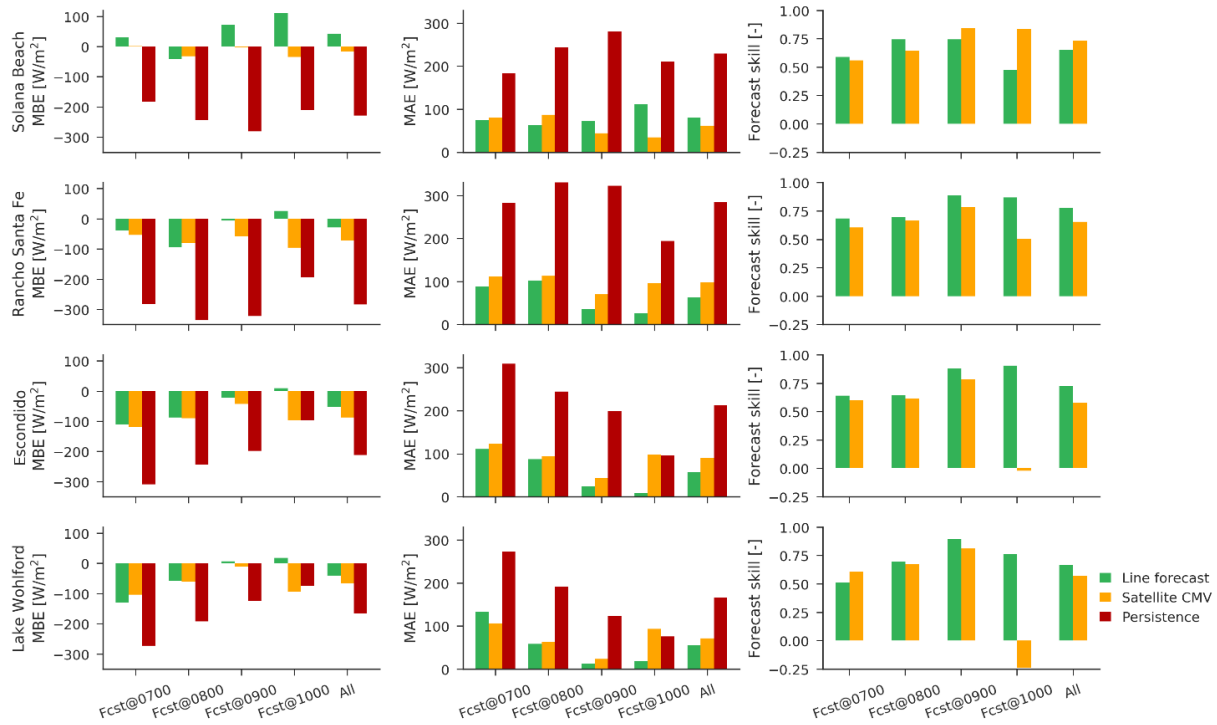
Figure 2.11: Averaged MBE, MAE, and FS for forecast horizons between 1 h to 5 h ahead for 5-15 June 2016 at Solana Beach, Rancho Santa Fe, Escondido, and Lake Wohlford.

is likely because of cold ocean advection and inhomogeneous horizontal entrainment between the clear and cloudy edge. For Santa Rosa, Saratoga, Salinas Valley, and San Luis Obispo, the line forecast exhibits a similar FS as for the sites in southern California, outperforming the persistence and CMV forecasts over all forecast horizons and forecast issue times. As these four sites are located away from the immediate coast, solar heating is likely the dominant factor that controls the burn-off time.

SolarAnywhere GHI in Figure 2.9 indicates that Sc clouds often persist for the whole day at San Francisco and Monterey. Among the four sites in central and northern California where Sc clouds dissipate before noon, it can be seen from the area between SolarAnywhere GHI and clear sky GHI curve (Figure 2.12) that Saratoga is the least cloudy station. Saratoga also has the highest land elevation among these four sites. Stations at the immediate coast have larger errors (e.g., San Francisco, Monterey) due to ambiguous cloud dissipation time or clouds persisting for the whole

day. This phenomenon happens more frequently at the immediate coast as cold advection from the ocean has a greater impact in this region. Ocean advection has a smaller impact further inland as the coastal land acts as a barrier for the advection. In some cases, mountain ranges act as a coastal land barrier between the ocean and the station, making it very difficult for clouds to come back after the initial dissipation. For example, the Santa Cruz mountains are located immediately to the west of Saratoga. As a result, it is unusual for ocean advection to have a strong impact at Saratoga, and clear sky is expected after the initial burn-off of the Sc cloud deck. Wind direction and coastline orientation also influence whether clouds will come back. The line forecast is expected to perform better at stations outside of the immediate coastal swath as good agreements between fitted k_t and dissipation time are found in Figure 2.9. In practice, the performance of the line forecast depends on the accuracy of forecasted cloud dissipation time. Figure 2.9 indicates the best-case scenario of the line forecast (i.e., with known cloud dissipation time).

In complex terrain, many different factors also control the dissipation time. Torregrosa et al. (2016) found that besides land elevation, terrain feature placement relative to wind direction and length of terrain feature are important factors controlling Sc cloud coverage. For example, low-lying gaps at Salinas Valley promote inland incursions of Sc clouds. Leeward coastlines (SW-S) are less cloudy than windward (W-NW) coastlines. This is the reason Eureka is cloudier than a station to the south where the coastline changes direction from NW to SW (e.g., Mendocino, located about 150 km south of Eureka) even if both locations have the same land elevation. While taking the median land elevation of the boundary would have falsely flagged places like Mendocino as cloudy, the way the line forecast predicts future k_t automatically corrects these points to clear. However, the line forecast is unable to correct the points that are falsely flagged as clear. This is evident in San Francisco and Monterey (Figure 2.12) where the line forecast over-predicts irradiance. In fact, satellite CMV forecasts perform better than the line forecast and persistence at these two locations. During the morning forecast issue time, the satellite CMV does not detect movement of Sc clouds, and no cloud advection is being forecasted at the coastal

stations. This is the reason satellite CMV forecast behaves similarly to persistence, except that the persistence forecast often suffers from using a fixed single k_t at forecast issue time while CMV averages k_t from previous times.

Geographical error distribution

To exhaustively quantify the usefulness of the line forecast, hourly SolarAnywhere GHI data at a horizontal resolution of 2 km is analyzed. Figure 2.14 is a spatial map of the line forecast FS averaged over all forecasts issued at 0800 PST in southern California, averaged across all forecast horizons, and Figure 2.15 is for all forecasts issued at 0800 PST in central and northern California. Note that FS has a maximum of 1, and a positive value of FS represents an improvement over persistence forecast.

For southern California, positive FS is found almost everywhere in the domain, making the line forecast a competitive forecast during Sc cloud days. The slightly negative FS around Santa Ana Mountains (33.7°N, 117.5°W) is associated with its high land elevation. Land elevation here is often higher than the inversion base height in this area, making it hard for Sc clouds to form (an example can be seen in Figure 2.1). For central and northern California, positive FS are found in regions slightly away from the coast, while negative FS are found at the immediate coast. Areas of negative FS vary along the coastline. The most negative FS is found along the coast of Monterey Bay a region with an abundant coverage of low clouds (Clemesha et al., 2016, Torregrosa et al., 2016). Although FS is negative at the San Francisco station chosen in Section 2.3.4, a gradient of FS can be seen near the San Francisco Bay. FS becomes positive about 20 km south of the chosen San Francisco station, including at the San Francisco International Airport where Sc clouds often hinder the use of parallel runways due to low visibility. The spatial distribution of FS suggests the use of different forecast systems in different regions. Specific local forecast models based on machine learning and NWP may be more skilled at forecasting Sc cloud lifetime at the immediate coast where clouds tend to persist for the whole day and where
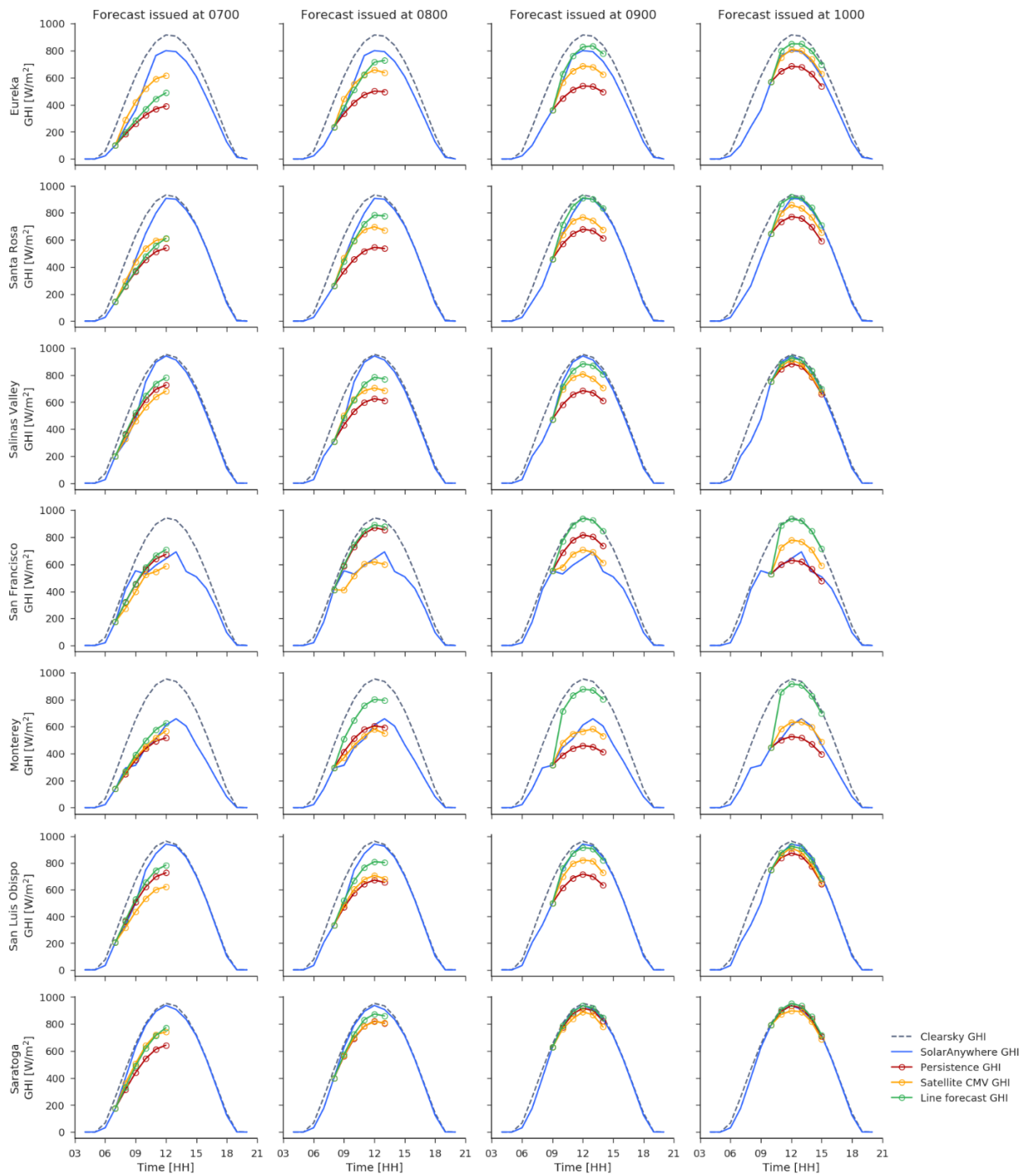
Figure 2.12: Hourly average of forecasted and satellite observed GHI for August 2016 at seven locations in central and northern California. Each column represents a different forecast issue time.
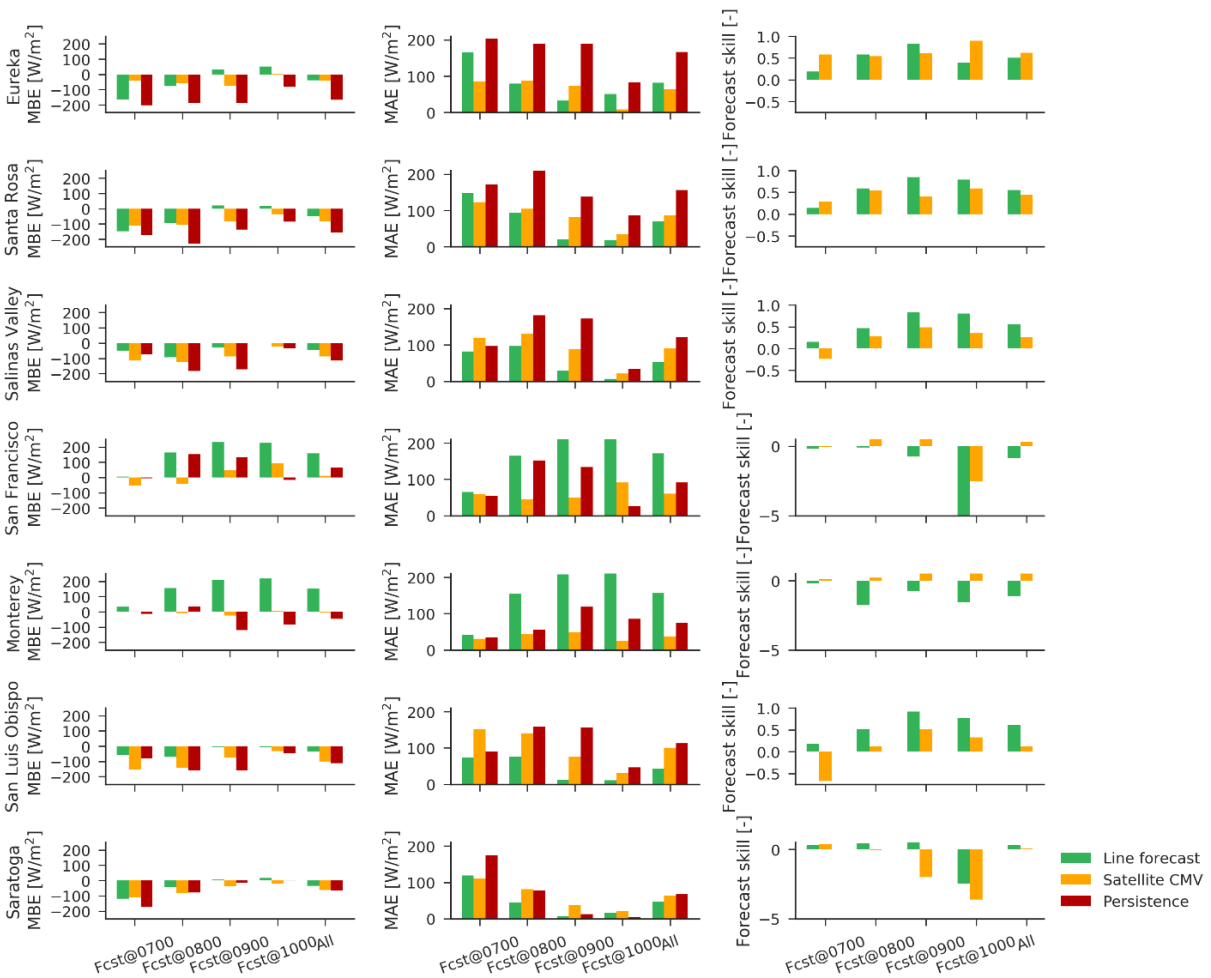
Figure 2.13: Hourly averaged MBE, MAE, and FS for forecast horizon between 1 h to 5 h ahead from August 2016 at 7 sites in central and northern California.

the line forecast FS are negative. Away from the coast where Sc clouds dissipate during the day and the line forecast FS are positive, the line forecast should be used to forecast GHI.
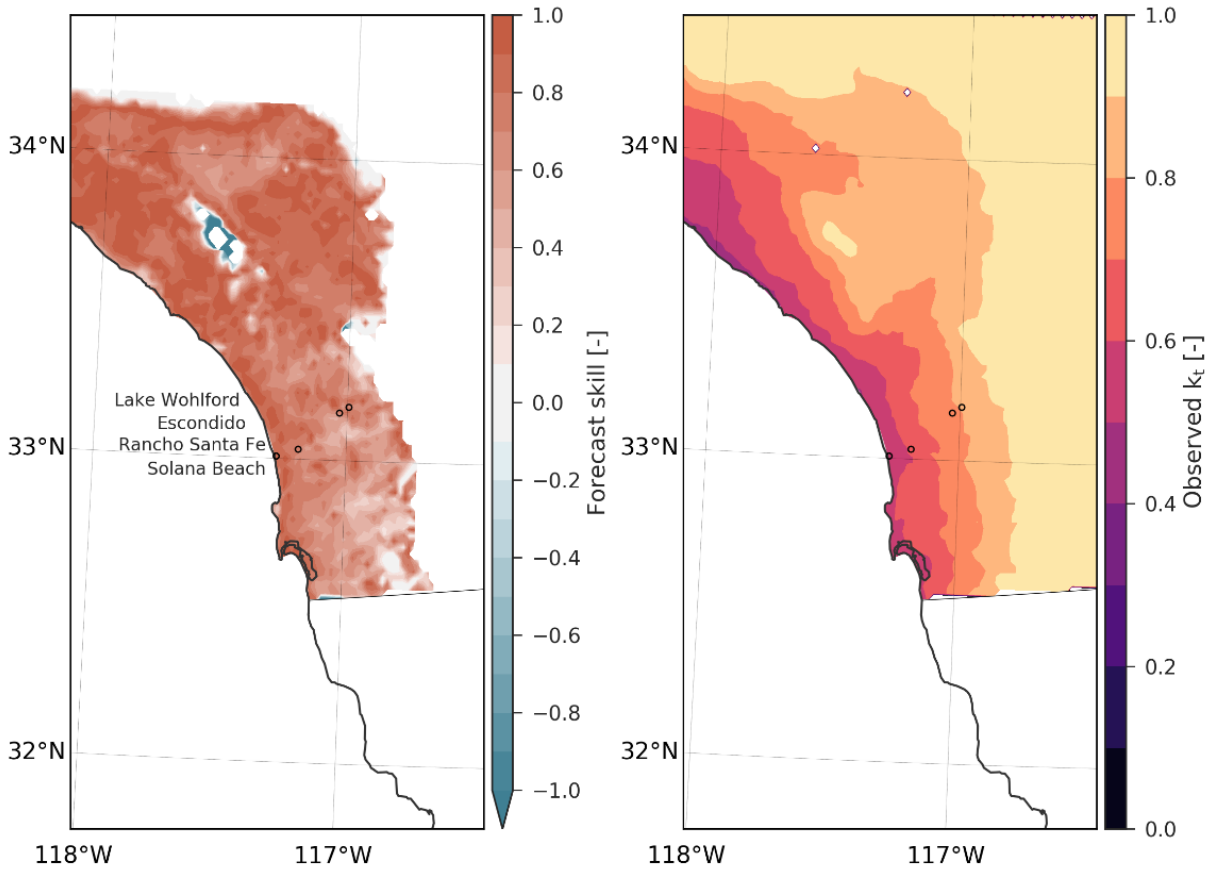
Figure 2.14: Left: Forecast skill of line forecasts issued at 8 PST, averaged over 1 h to 5 h ahead for 19 days in June 2016 for southern California. Right: Satellite derived kt averaged between 7 and 10 PST for the same 19 days.

2.5 Conclusions

A Sc cloud line forecast using GOES images is proposed and implemented in coastal California to improve the prediction of cloud dissipation time for forecast horizons between 15 hours ahead. The land elevation under the inland boundary of Sc clouds is used to track the cloud boundary and extrapolate it forward in time. This method assumes that solar heating is
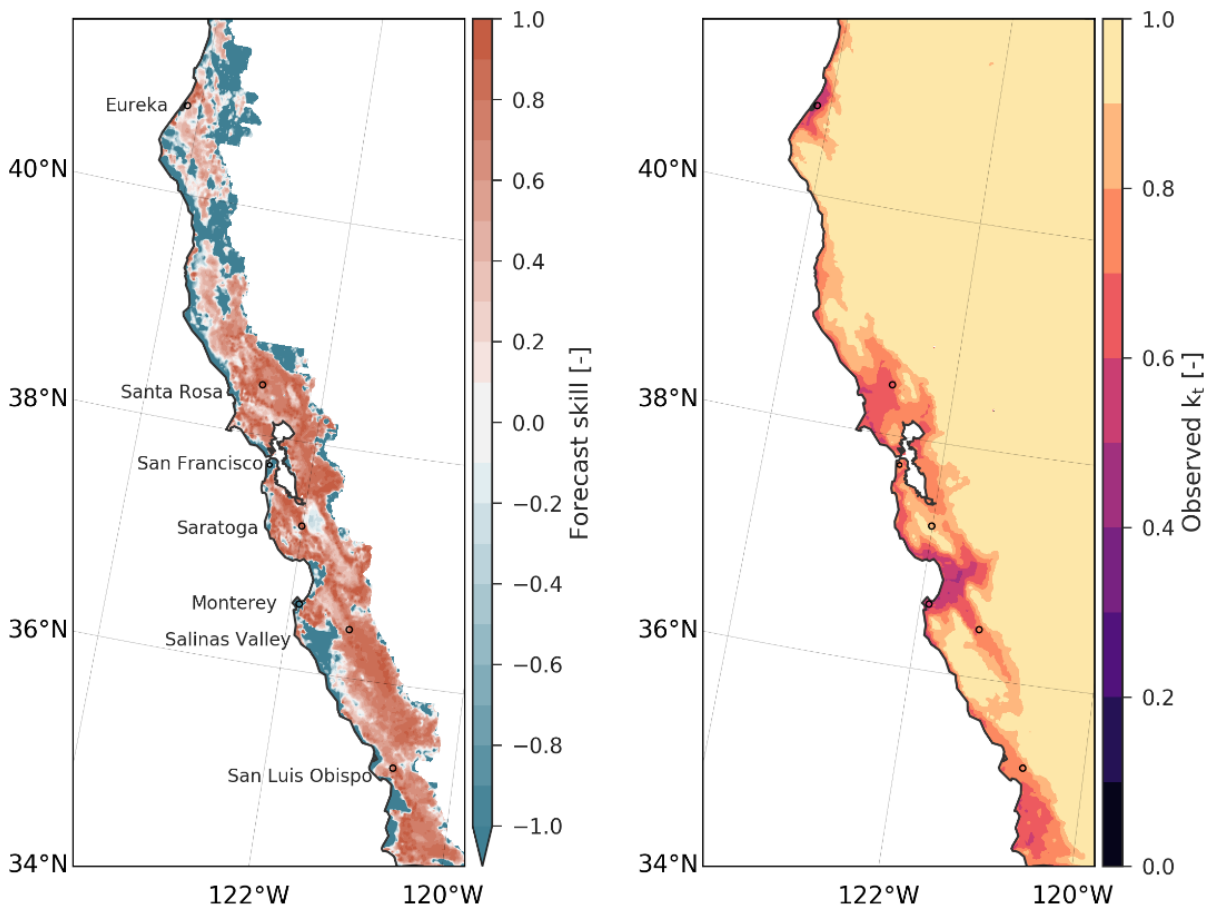
Figure 2.15: Forecast skill of line forecasts issued at 8 PST, averaged over 1 h to 5 h ahead for 25 days in August 2016 for central and northern California. Right: Satellite derived kt averaged between 7 and 10 PST for 25 days in August 2016.

the main factor controlling the dissipation of Sc clouds during the day, and a decrease in median land elevation at the boundary after sunrise is expected. This is because a strong temperature inversion marks the cloud top height, a lower land elevation means a larger mass of air above ground, and more heat is required to become cloud-free. Validation against satellite solar resource data shows that the line forecasts consistently outperform the persistence forecasts at 9 out of 11 stations. In addition, the line forecasts outperform the satellite CMV forecasts at 7 out of 11 stations. Supplementary validation at 2 km spatial resolution using the same satellite solar resource data shows superior performance to persistence forecasts in most places aside from the immediate coast where Sc clouds are more likely to persist for the whole day.

For the two regions validated in this study, the line forecast shows higher forecast skills in southern California than it does in central and northern California. The coastal topography likely plays an important role in the discrepancy in forecast skills (e.g., the simple topographic elevation distribution in San Diego favors the line forecast as it has more consistent meteorological conditions across the forecast domain). The lack of forecast skill at the immediate coast and the sharp gradient of dissipation time within a few kilometers of the coast suggest that at the immediate coast local processes are important in determining when the clouds dissipate. While the satellite CMV forecast performs the best at the immediate coast, it is inaccurate on days when the clouds do dissipate.

Improved Sc cloud forecasting is important because Sc cloud presence critically influences a broad array of applications. The novel Sc cloud forecast approach presented here may contribute to, among other applications, better management of the power system for the utilities and better planning for the aviation industry. Future work will focus on understanding factors controlling whether Sc clouds persist during the day at the immediate coast.

2.6 Acknowledgements

Chapter 2, in full with slight modifications, is a reprint of the material in the article "Coastal Stratocumulus cloud edge forecasts," published in *Solar Energy* (E. Wu, R. E. S. Clemesha, and J. Kleissl) in 2018 (Wu et al., 2018). The dissertation author was the primary investigator and author of this paper.

Chapter 3

Observation-Based Analog Ensemble Solar Forecast in Coastal California

3.1   Introduction

Solar generation can display high variability and an accurate solar forecast enables an improved operation of the electric grid. Despite steady improvements of forecasts from Numerical Weather Prediction (NWP) models, forecast skill is still limited by mean and conditional biases. In coastal California, solar production is often hindered by the formation and dissipation of Stratocumulus (Sc) clouds, which are most prominent in late spring and summer months. The majority of installed rooftop systems are located along the coast, posing a significant challenge. Sc clouds form in a shallow planetary boundary layer (PBL) at night and begin to dissipate after sunrise. Typical PBL height is often less than 1 km. Due to computational constraints, state-of-the-art NWP models have limited vertical resolution and parameterize the physical processes governing Sc clouds instead of directly solving them. This often leads to an erroneous representation of Sc clouds and thus an inaccurate solar forecast. While efforts have been made to improve the physical representation of Sc clouds in NWP models, imperfect initial conditions

and numerical and physical approximations still affect the accuracy of the forecast.

Statistical post-processing of NWP models (e.g., support vector regression, gradient-boosted regression, random forest regression) have been shown to improve the skill of solar forecasts (Gala et al., 2016, Gensler et al., 2016, Haupt and Kosovic, 2015). An analog ensemble (AnEn) for short-term solar forecast using historical runs from one NWP model (Regional Atmospheric Modeling System) outperformed quantile regression and persistence ensemble Alessandrini et al. (2015). In this study, we aim to build upon Alessandrini et al. (2015) and generate an observation-based AnEn to forecast day-ahead (sunrise to sunset) solar irradiance. The observation-based AnEn benefits from knowledge of the initial state, albeit it is often only available at a single location. Satellite data is employed to expand knowledge of the initial state.

3.2 Methods

3.2.1 Data

Satellite: Coastal low cloud identification

Geostationary Operational Environmental Satellites (GOES) provide images at both visible and infrared wavelengths. A GOES-based long-term coastal low cloudiness (CLC) dataset along the California coast Clemesha et al. (2016) identifies whether a 4 km pixel is covered with low clouds every 30 minutes. Each day in the CLC dataset is classified as Sc or non-Sc day, following criteria similar to Wu et al. (2018). The CLC cloud coverage percentage in three coastal and one ocean regions are used to generate the analogs.

Satellite: Solar irradiance

Another GOES derived product, SolarAnywhere (2019), provides half-hourly solar irradiance data at 1 km spatial resolution. For Sc days, each low-cloud pixel is labeled based on its

averaged normalized solar irradiance (k_t) between 0700 to 1000 Pacific Standard Time (PST), where k_t is defined as the ratio of global horizontal irradiance (GHI) to clear sky GHI. PST is 8 h behind Coordinated Universal Time (UTC) and will be used for the remainder of this study. Greater San Diego ($31.5° - 34.5°$N, $116.5° - 118.5°$W) with land elevation lower than 375 m is considered. Land pixels are classified as immediate (averaged $k_t < 0.6$), intermediate ($k_t < 0.7$), and extended coastal land ($k_t < 0.8$). One ocean region ($32.0° - 33.0°$N, $117.3° - 118.3°$W) is defined to capture Sc clouds over the ocean. Classifying three coastal land regions has two main advantages: (i) capturing more details of the Sc cloud location and (ii) determining whether Sc clouds exhibit dissipating signals during the early morning, which is commonly seen in the extended coast.

Radiosonde

Radiosonde data at the NKX Miramar Marine Corps Air Station in San Diego, CA (NKX: $32.85°$N, $117.11°$W) are reported at 0400 PST, describing the vertical structure of the PBL. When a single layer of Sc clouds is present, thermodynamic properties are nearly constant in height and the PBL is said to be well-mixed. On the other hand, decoupling describes a separated layer within the PBL and allows Cumulus clouds to form below the Sc cloud layer. Radiosonde profiles of temperature and moisture are used to classify each day's PBL state into: (i) cloudy and well-mixed, (ii) cloudy and decoupled following Ghate et al. (2014), and (iii) clear. The following variables are available from the radiosonde: inversion base height (z_i), PBL averaged liquid water potential temperature ($\theta_{l_{\text{BL}}}$), inversion strength ($\Delta\theta_l$), tropospheric total water mixing ratio ($q_{t_{3km}}$), lifting condensation level (z_b), surface temperature (T_{sfc}), surface dew point temperature (T_{dew}), precipitable water for the entire sounding (PW), and geopotential height difference between 1000 and 500 hPa (ΔZ). A detailed description of the retrieval of each variable can be found in Zamora Zapata et al. (2020).

Surface weather observations

Surface weather observations at NKX (32.86°N, 117.14°W) are used to retrieve zonal and meridional wind speed (u, v) at 10 m. Finally, sea surface temperature (SST) is retrieved from one buoy (Torrey Pines Outer: 32.933°N, 117.391°W). For surface observations and buoy measurements, only data corresponding to the radiosonde launch time (0400 PST) are used.

3.2.2 Analog ensemble implementation

The AnEn forecast is issued at NKX daily at 0400 PST, the time when radiosonde data are available. For cloudy well-mixed or cloudy decoupled days, 12 variables including low cloud coverage CC (over ocean CC_{ocean}, immediate CC_{im}, intermediate CC_{int}, and extended coastal land CC_{ext}), z_i (which is also the cloud top height), $\theta_{l_{BL}}$, $\Delta\theta_l$, $q_{t_{3km}}$, z_b (also known as cloud base height), u, v, and SST are used to find the closest match. For clear days, the number of variables decreases to eight, with z_i, T_{sfc}, T_{dew}, PW, ΔZ, u, v, and SST. For each scenario, the top matching days are selected, and their corresponding observed GHI timeseries are used to constitute the mean and median ensemble forecast. The top matches are determined following Delle Monache et al. (2011), where the metric used to rank past observations' similarity is:

$$L_{O,A} = \sum_{i=1}^{N} \frac{w_i}{\sigma_i} \left(O_i - A_i\right)^2, \tag{3.1}$$

where O is the current observation, A is the analog observation in the past, N is the number of physical variables, w_i and σ_i are the weight and standard deviation of each physical variable, and i denotes different variables. The rank metric $L_{O,A}$ is calculated each day at 0400 PST. Sensitivity on the number of analogs and variable weights will be discussed in the next section.

During the testing stage, $L_{O,A}$ is computed from May to September 2014-2017, excluding the test day. While this study focuses on issuing an AnEn forecast at one location, it can be extended to other sites within the domain as specified in section 3.2.1 as a similar PBL state is

43

expected.

Fig. 3.1 and Fig. 3.2 illustrate two sample AnEn forecasts where five analogs (gray lines) are used to generate the mean and median ensembles (blue and green lines). Fig. 3.1 shows an example of a cloudy and well-mixed case, where the cloud dissipation around 0800 PST is well captured by most of the analogs. Fig. 3.2 shows a cloudy and decoupled case that is highly variable throughout the day and that is very different from the previous day (orange line). The AnEn forecasts predict some of this variability as seen in the spread of the individual analogs.
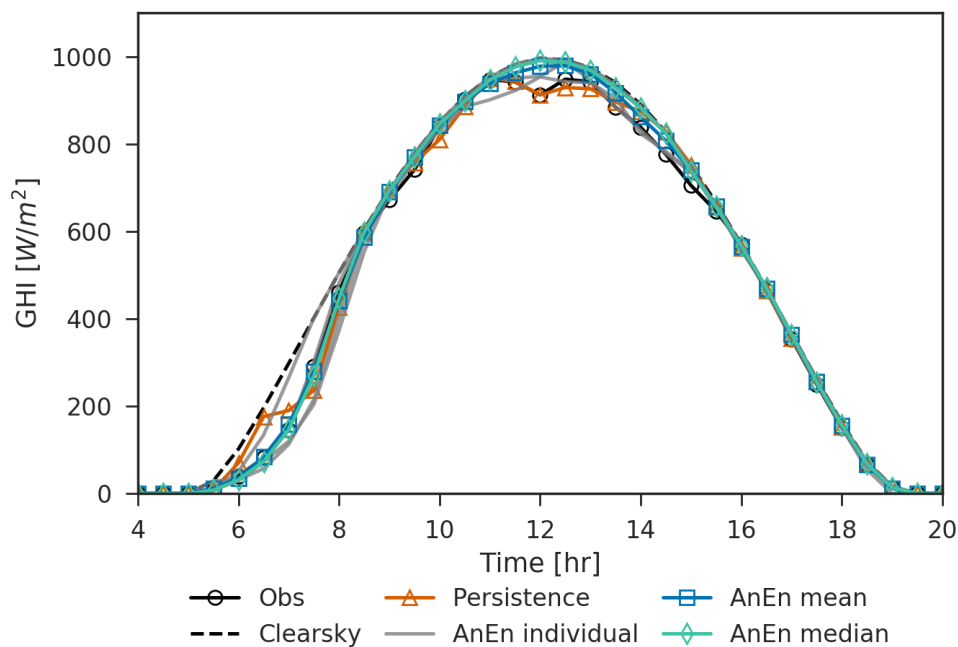
Figure 3.1: Example of a cloudy and well-mixed AnEn forecast at NKX: July 21, 2017.

3.2.3   Error metrics

The performance of the AnEn forecast is evaluated using the root mean square error (RMSE), which is decomposed into centered root mean square error (CRMSE) and bias (BIAS),
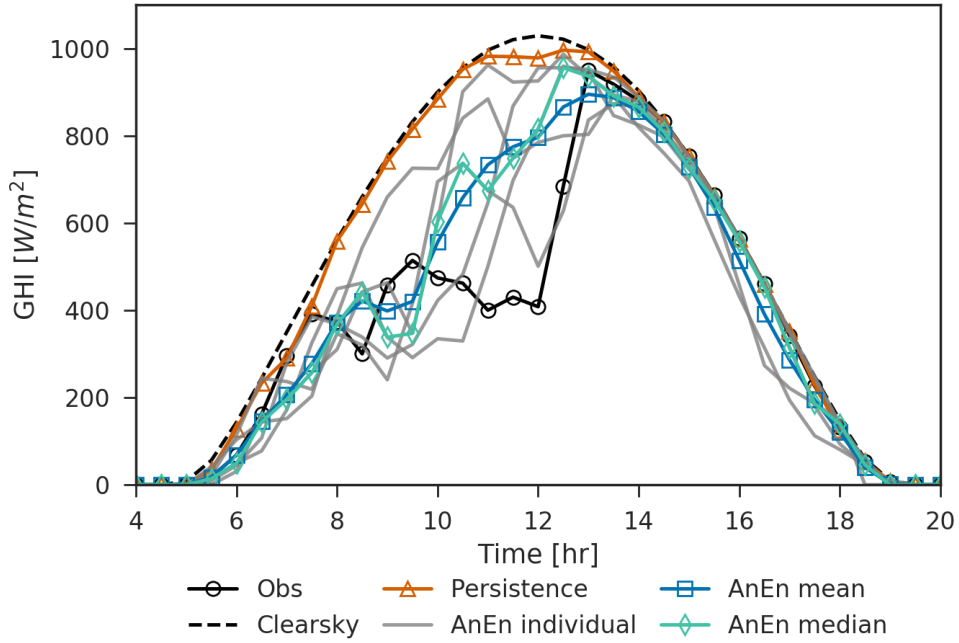
Figure 3.2: Example of a cloudy and decoupled AnEn forecast at NKX: May 26, 2016.

as represented in Delle Monache et al. (2011), Taylor (2001):

$$\text{RMSE}^2 = \frac{1}{N_P} \sum_{i=1}^{N_p} \left(F_i - O_i \right)^2 = \text{CRMSE}^2 + \text{BIAS}^2, \tag{3.2}$$

where

$$\text{CRMSE}^2 = \frac{1}{N_P} \sum_{i=1}^{N_p} \left[\left(F_i - \overline{F} \right) - \left(O_i - \overline{O} \right) \right]^2, \tag{3.3}$$

and

$$\text{BIAS} = \overline{F} - \overline{O}. \tag{3.4}$$

The quantity N_p is the number of available (F_i, O_i) pairs, where F_i and O_i denote a forecast and an observation pair. $\overline{F}$ and $\overline{O}$ are the average of forecasts and observations among the N_p pairs. CRMSE is the random component of RMSE and can be interpreted as the intrinsic predictive skill of the forecast. BIAS is the systematic error.

3.3 Discussions and Results

3.3.1 Determining the best number of analogs
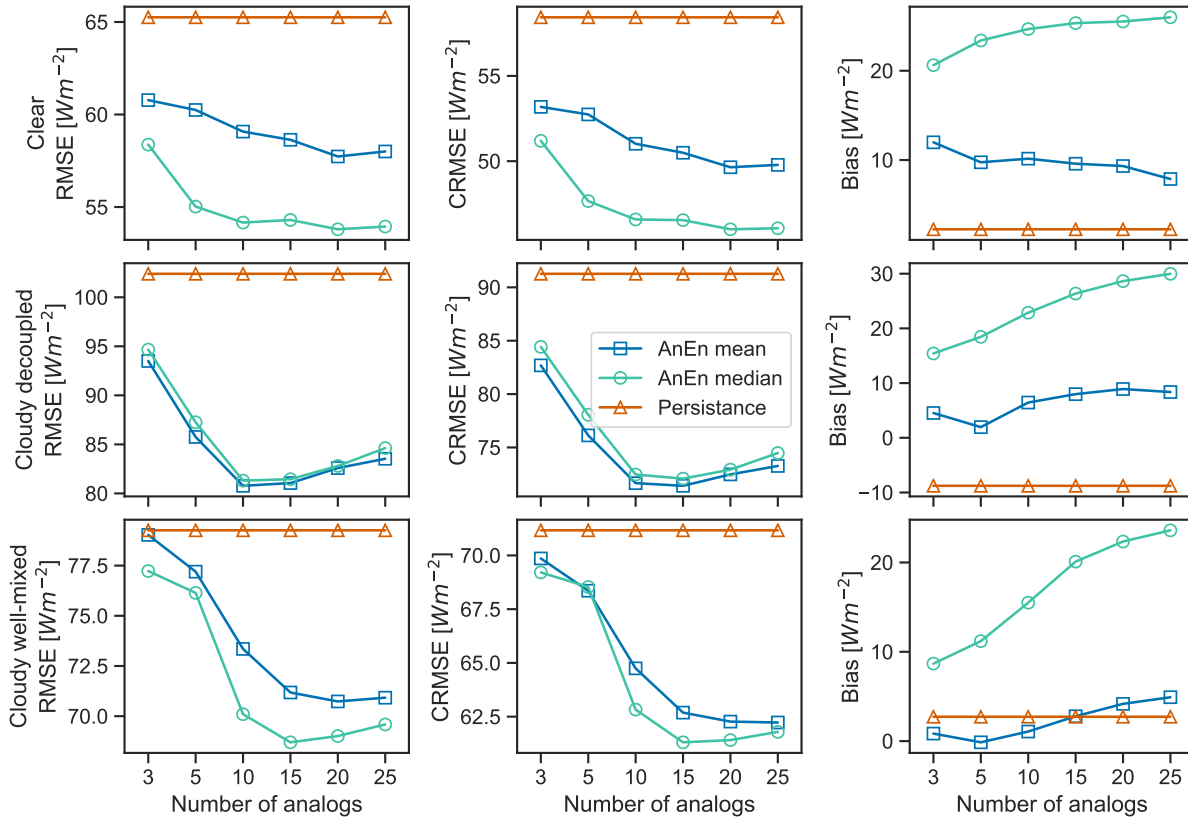
Figure 3.3: Error statistics with different number of analogs under clear, cloudy decoupled, and cloudy well-mixed days. AnEn mean, median, and persistence forecast are shown.

We study the sensitivity of the AnEn forecast to the number of analogs for a base setup of equal weights, and varying the number of analogs within [3, 5, 10, 15, 20, 25]. A small number of analogs is unlikely to be statistically consistent, while a large number of analogs will include irrelevant historical days and could be less accurate. Fig. 3.3 shows the error statistics for clear, cloudy decoupled, and cloudy well-mixed cases. The persistence forecast is defined as the observed GHI from the previous day and is thus insensitive to the number of analogs. For the AnEn mean and median, RMSE and CRMSE follow the same trend, while the trend for BIAS

differs in clear and cloudy cases. In general, RMSE and CRMSE decrease with the number of analogs and plateau around 15 analogs. In some cases, the error increases slightly after 15 analogs. We therefore conclude that 15 analogs are sufficient to reach statistical consistency. In this sensitivity test, equal weights are used for the clear cases, and a best guess of weights is used for the cloudy cases where weights are doubled for z_i, $\Delta\theta_l$, and CC_{ocean} while the other variables have equal weights.

3.3.2 Determining the best weights

In order to determine the weights that minimize the RMSE of ensemble mean and median forecasts, we explore the sensitivity of the method to different combinations of weights. In this section, we focus on cloudy decoupled and well-mixed cases. We begin with 12 variables as stated in Section 3.2.2. To establish a baseline reference, equal weights for all 12 variables are used (Sens1 in Fig. 3.4). In the next 12 sensitivity tests (Sens$2-13$), we double one variable weight while keeping the remaining 11 weights equal. Fig. 3.4 shows the RMSE of the baseline and sensitivity tests for cloudy decoupled and cloudy well-mixed days. We find that cloudy decoupled days have lower errors than the baseline (Sens1) when the weight for z_i or v is doubled (Sens$2,8$). For cloudy well-mixed days, lower errors are found when doubling the weight for z_i, $\Delta\theta_l$, $q_{t_{3km}}$, z_b, u, CC_{im}, or CC_{int} (Sens$2,4-7,11,12$). The results of this test suggest that the decoupled days may not have a lot of similarity associated with the radiosonde nor satellite variables. This is expected as the well-mixed assumption does not represent decoupled days, and as a result the detection of variables such as $\Delta\theta_l$, $q_{t_{3km}}$, z_b is questionable. The exception is z_i, since it is independent of the well-mixed assumption, and strongly decoupled PBLs typically show larger z_i. For cloudy well-mixed days, both radiosonde and satellite variables play an important role in generating a good AnEn forecast. Overall, the AnEn median has a lower RMSE than the AnEn mean.

The weight sensitivity test reveals that some variables impact the results of the AnEn

47

more than others. In order to find one set of optimal weights for all cloudy cases, we perform a sequential search on all possible weight combinations with some constraints based on the previous test (Fig. 3.4). We limit $w_i \geq 0.2$ for $i \in \{z_i, \Delta\theta_l, u\}$, and set increments of 0.1 for each weight, generating 715 possible weight combinations. The AnEn median is used to quantify the skill of AnEn forecast under each weight combination. Fig. 3.5 shows the distribution of RMSE for cloudy decoupled and cloudy well-mixed days. The AnEn for decoupled days is more sensitive to the different weight combinations as the spread is wider. Of the 715 cases, 105 (or 15%) runs have a smaller RMSE than the reference case (Sens1) for cloudy decoupled days. As for the cloudy well-mixed days, the number increases to 229 (or 32%). We select the optimal set of weights as the one that results in the lowest sum of RMSEs for cloudy decoupled and well-mixed days. The final weights are $w_{z_i} = 0.3$, $w_{\theta_{l_{BL}}} = 0.2$, $w_u = 0.2$, $w_{q_{t_{3km}}} = 0.1$, $w_{\text{SST}} = 0.1$, and $w_{\text{CC}_{\text{im}}} = 0.1$. The final configuration results in a reduction in RMSE of 3.0 W m^{-2} for decoupled days and 2.5 W m^{-2} for well-mixed days when compared to the reference case (Sens1).
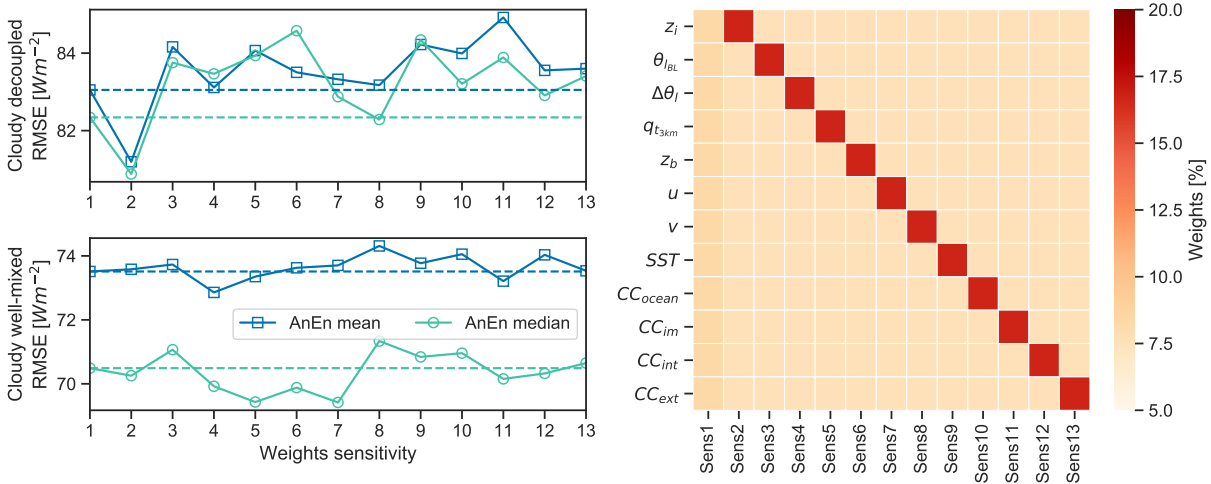
Figure 3.4: Sensitivity to different weights for cloudy decoupled and cloudy well-mixed days. Left panel: RMSE of AnEn mean and median. Right panel: the corresponding weights used in each sensitivity test. The dashed line indicates the RMSE from the reference case (*Sens*1).
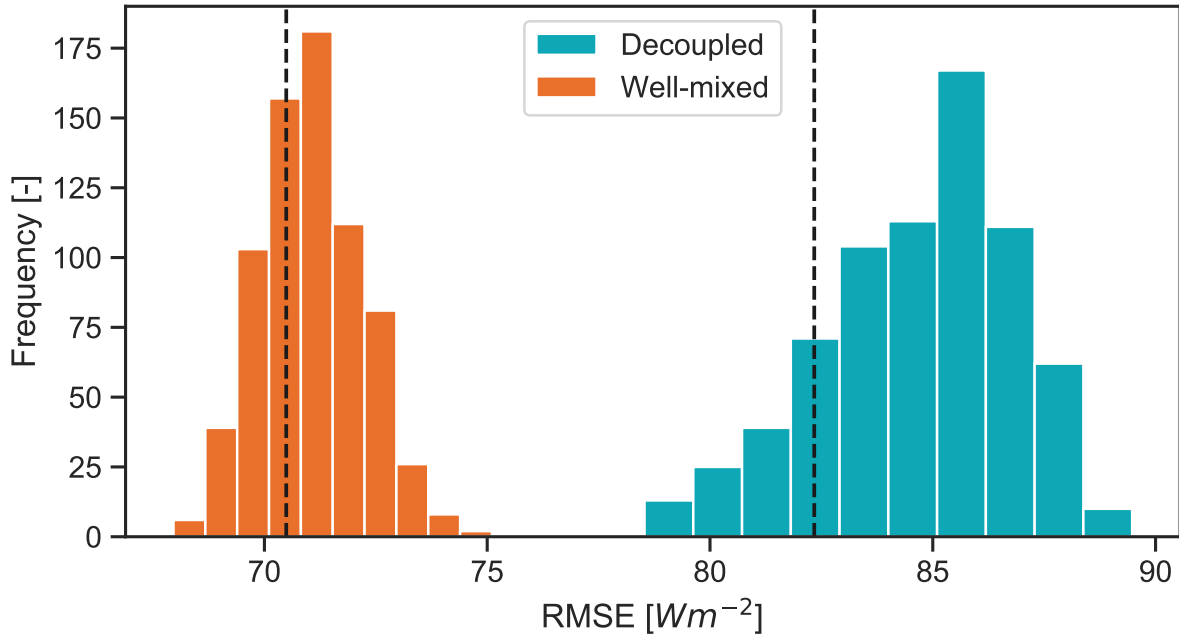
Figure 3.5: Histogram of RMSE for 715 combinations of weights for cloudy decoupled and cloudy well-mixed days using AnEn median. The dashed lines are the reference case (Sens1 in Fig. 3.4) RMSE.

3.3.3 Overall error statistics

We quantify the performance of the AnEn forecast with the optimal number of analogs (15) and weights. An additional NWP model– Weather Research and Forecasting (WRF)– is used as a baseline for comparison with the AnEn method. WRF is an in-house operational forecast issued for San Diego, with initial and boundary conditions derived from the 1600 PST North American Model (NAM) data. A more detailed description of the model setup can be found in Sahu et al. (2018). Table 3.1 shows the half-hourly averaged error metrics calculated for the testing dataset during May to September from 2014-2017. Both AnEn mean and median have a lower overall RMSE and CRMSE than the persistence forecast. Errors are consistently lower for the clear cases, since clear conditions are expected to prevail for the whole day (equal weights were used for clear days). In contrast, decoupled days show the largest errors, indicating that their higher variability is more difficult to capture with both the persistence and AnEn forecast. The

good performance of the AnEn forecast for the well-mixed cloudy cases indicates that the initial meteorological state is a good predictor of dissipation time. The differences between the mean and median forecast suggest that the distribution of the set of analogs is not Gaussian. AnEn forecasts have lower errors than WRF forecasts, especially for cloudy decoupled cases.

The skill of the AnEn method relies on historical similarity for local cloudy conditions. For Sc clouds, we expect similarity in meteorological conditions at 0400 PST to be a strong predictor of dissipation time. If clouds form again in the afternoon, the timing of these events might be harder to capture with 0400 PST conditions due to greater changes in synoptic conditions.

Higher GHI variability is observed for decoupled days, because Cumulus clouds can form underneath the Sc layer. There is a lack of knowledge on the dissipation of decoupled PBL clouds over coastal regions, but we expect them to dissipate later, as they usually have greater cloudiness over marine regions in comparison to Sc layers.

Table 3.1: Half-hourly averaged error statistics for three PBL states from 2014-2017: clear (122 days), cloudy and decoupled (106 days), cloudy and well-mixed (382 days).

PBL state	AnEn mean	AnEn median	Persistence	WRF[†]
	RMSE/CRMSE/Bias [Wm^{-2}]			
Clear	59/50/10	54/47/25	65/58/2	58/52/21
Cloudy decoupled	79/70/6	79/70/23	102/91/-9	96/86/11
Cloudy well-mixed	72/63/2	68/61/19	79/71/3	76/66/28

[†]Note that WRF forecast is only available in 2016 and 2017.

3.4 Conclusions

We developed and tested an observation-based AnEn in San Diego, CA. The AnEn takes observations from satellite, radiosonde, and surface stations to find the closest historical days (analogs) and blends them to generate a forecast of solar radiation for the whole day. Sensitivity to the number of analogs and weights were performed in order to minimize the errors. We found 15 to be the ideal number of analogs, and that the optimal weights highlight the importance

of the following variables: z_i, $\theta_{l_{BL}}$, u, $q_{t_{3km}}$, SST, and CC_{im} for cloudy days. Both AnEn mean and median forecasts have a lower RMSE and CRMSE compared to both persistence and WRF forecasts. The AnEn median method has the higher forecast skill of the two. The AnEn forecast is able to capture the Sc dissipation for the well-mixed cases in the early morning, but the variability in the decoupled cases is harder to capture, which leads to higher errors.

3.5   Acknowledgments

Chapter 3, in full with slight modifications, is a reprint of the material in the article "Observation-Based Analog Ensemble Solar Forecast in Coastal California," (E. Wu, M. Zamora Zapata, L. D. Monache, and J. Kleissl) presented at the 46th IEEE Photovoltaic Specialists Conference (PVSC) in 2019 (Wu et al., 2019). The dissertation author was the joint primary investigator and joint first author.

Chapter 4

On the Parameterization of Convective Downdrafts for Marine Stratocumulus Clouds

4.1   Introduction

Stratocumulus (Sc) clouds are one of the most common cloud types on Earth (Hahn and Warren, 2007). They form under strong temperature inversions and are prevalent off the western coast of continents, on the descending side of the Hadley cell. Their impact on the Earth's energy budget is significant as they strongly reflect incoming solar radiation, with a much weaker effect on outgoing longwave radiation (Wood, 2012). Accurate modeling of Sc clouds has high importance for several reasons: (i) they are one of the key sources of uncertainty in climate predictions (Bony and Dufresne, 2005, Zelinka et al., 2017), (ii) they affect solar power integration into the electric grid (Wu et al., 2018, Yang and Kleissl, 2016, Zhong et al., 2017), and (iii) they impact aviation by hindering the takeoff and landing of flights (Reynolds et al., 2012).

Physical processes governing the evolution of the stratocumulus-topped boundary layer

(STBL)— such as cloud-top radiative cooling, entrainment, evaporative cooling, surface fluxes, wind shear, and precipitation— widely range on spatial and temporal scales, and modeling Sc clouds is quite challenging as a result (e.g. Lilly, 1968, Stevens, 2002, Wood, 2012). Efforts through both observational campaigns (e.g. Crosbie et al., 2016, Malinowski et al., 2013, Stevens et al., 2003) and high resolution numerical modeling (e.g. Blossey et al., 2013, Chung et al., 2012, de Lozar and Mellado, 2015, Kurowski et al., 2009, Matheou and Teixeira, 2019, Mellado et al., 2018, Pedersen et al., 2016, Stevens et al., 2005, Yamaguchi and Randall, 2011) have significantly advanced our understanding of the physics of Sc clouds. These physical insights are important for numerical weather prediction (NWP) and general circulation models (GCMs) where grid resolution is coarse.

The picture emerging from those studies is that cloud-top radiative cooling is a critical source of STBL turbulence (Matheou and Teixeira, 2019), contributing to cloud-top entrainment (Mellado, 2017). The combined effect of both evaporative and radiative cooling— the former typically enhanced by wind shear (Mellado et al., 2014)— destabilizes the top of cloud layer through buoyancy reversal that leads to the formation of negatively buoyant weak downdrafts. This process is often considered responsible for the generation of cloud holes in largely unbroken Sc clouds (Gerber et al., 2005, Kurowski et al., 2009). Many small-scale phenomena (e.g., entrainment, shear, evaporative cooling, cloud microphysics) are at play in the origin of downdrafts and can strongly influence vertical mixing (Mellado, 2017). Exactly how these processes interact with each other remains a research challenge.

Turbulent transport in the STBL is the main driver to the formation, maintenance, and dissipation of Sc clouds. In coarse-resolution models, turbulent transport is typically parameterized using simplified one-dimensional planetary boundary layer (PBL) schemes. Global NWP models (e.g. Teixeira, 1999) and climate models tend to underestimate Sc clouds (Lin et al., 2014, Teixeira et al., 2011), although there is an improvement in the representation of the radiative properties by a newer generation of climate models (Engstrm et al., 2014). In terms of mesoscale

models, Ghonima et al. (2017) compared three different PBL schemes in the Weather Research and Forecasting (WRF) model and found that they all underestimate entrainment, producing too moist and cold STBLs. Huang et al. (2013b) compared five different WRF PBL parameterizations and highlighted the difficulties of simulating the STBL. Recent studies supported the importance of downdrafts in transporting turbulent heat and moisture flux in the PBL (Brient et al., 2019, Chinita et al., 2017, Davini et al., 2017) through analyzing LES of STBL. Brient et al. (2019) concluded that for a more accurate parameterization of turbulence within STBL, downdrafts should be explicitly included in climate models. Downdrafts were recently implemented by Han and Bretherton (2019) in a turbulent kinetic energy (TKE)-based moist Eddy-Diffusivity/Mass-Flux (EDMF) parameterization within the GFS model, and they found more accurate liquid water and wind speed profiles for marine STBLs.

This study introduces parameterized downdrafts into NWP and aims at investigating their impact on the evolution of the STBL. To test whether convective downdrafts are necessary to properly represent Sc clouds, we implement a new downdraft parameterization in WRF based on the EDMF approach that uses Mellor-Yamada-Nakanishi-Niino (MYNN) as the ED component. This differs from Han and Bretherton (2019) where different ED and MF models were used and additional features were implemented to advance the vertical turbulence mixing parameterization for not only STBL but also other conditions. We place a special emphasis on evaluating the role of non-local transport in STBL with gradual changes to the model in order to separate the effects coming from convective downdrafts. The new parameterization is evaluated in two typical STBL cases, frequently used in modeling studies.

Section 5.3 describes the EDMF and MYNN schemes as well as the updraft and downdraft implementation in WRF. The numerical design of the LES setup, WRF single column model (SCM), and updraft and downdraft properties are described in Section 4.3. WRF SCM results for both STBL cases are shown in Section 5.4. Finally, conclusions are presented in Section 5.5.

4.2 PBL scheme with downdrafts

In coarse resolution atmospheric models, the PBL scheme determines turbulent flux profiles within the PBL as well as the overlying air, providing tendencies of temperature, moisture, and horizontal momentum due to mixing and turbulent transport for the entire atmospheric column. This section first gives an overview of the EDMF framework, then the details of ED and MF models are presented (Sections 5.34.2.2 and 5.34.2.3). The properties of updrafts and downdrafts are diagnosed using LES and presented in Section 4.3 in order to quantify the validity of the parameterized mass-flux model.

4.2.1 The Eddy-Diffusivity/Mass-Flux (EDMF) Approach

Siebesma et al. (2007), Siebesma and Teixeira (2000), Teixeira and Siebesma (2000) introduced the eddy diffusivity/mass-flux (EDMF) approach for parameterizing turbulence in the dry convective boundary layer, and additional improvements have been made by Witek et al. (2011). The idea behind EDMF is to parameterize the turbulent fluxes as a sum of local (diffusive) transport through ED and non-local (convective) transport through the mass-flux contribution. The EDMF approach has been extended to represent moist convection since then (e.g. Angevine et al., 2010, 2018, Neggers, 2009, Neggers et al., 2009, Soares et al., 2004, Suselj et al., 2019a,b, 2013). For the moist extention, the updrafts start out as dry and condense when the saturation conditions are met. In other words, dry updrafts can continuously change into moist updrafts, without assuming any coupling between those two layers. In this sense, the EDMF approach provides a unified parameterization of the boundary layer and moist convection that makes it a convenient framework for modeling STBL.

4.2.2 ED scheme: The Mellor-Yamada Nakanishi and Niino (MYNN)

The ED component we use is the level 2.5 Mellor-Yamada Nakanishi and Niino (MYNN) model, which is a modified Mellor-Yamada turbulence closure scheme originally developed by Mellor and Yamada (1982), with significant improvements made over the years (Nakanishi and Niino, 2006, 2009). In MYNN, vertical turbulent fluxes are modeled according to K-theory:

$$\overline{w'\varphi'} = -K\frac{\partial \varphi}{\partial z}, \tag{4.1}$$

where eddy diffusivity K is parameterized as a function of the TKE (q), master length scale L, and stability correction functions $S_{h,m}$, which differ for heat and momentum:

$$K_{h,m}(z) = q(z)L(z)S_{h,m}(z). \tag{4.2}$$

The prognostic thermodynamic equations in MYNN use moist conserved variables: liquid water potential temperature θ_l and total water mixing ratio q_t. The prognostic dynamic variables are the horizontal components of wind u and v. An additional prognostic equation of the MYNN Level 2.5 model solves the (doubled) subgrid TKE: $q^2 = 2 \times TKE = \overline{u'^2} + \overline{v'^2} + \overline{w'^2}$, and is formulated as:

$$\frac{\partial q^2}{\partial t} = -\frac{\partial}{\partial z}\left(LqS_q\frac{\partial q^2}{\partial z}\right) - 2\left(\overline{u'w'}\frac{\partial U}{\partial z} + \overline{v'w'}\frac{\partial V}{\partial z}\right) + 2\frac{g}{\theta_0}\overline{w'\theta_v'} - 2\varepsilon. \tag{4.3}$$

Eq. 4.3 describes the tendency of TKE, due to turbulent and pressure transport, shear production, buoyant production, and turbulent dissipation. L is the master length scale as in Eq. 4.2, and $S_q = 3S_m$ is the stability correction function for TKE (see Nakanishi and Niino (2009) for detailed formulations). L is designed such that the smallest length scale out of three different formulations dominates at a given level. The first formulation is the surface length scale L_{sfc}, which is the Prandtl mixing length corrected for stability. It is small near the surface, but increases rapidly

with height. The second one, the turbulent length scale for a well-mixed layer L_{turb}, is formulated as a function of the vertically-integrated TKE, independent of height. Finally, the buoyancy length scale L_{buoy} is computed as a function of local stratification (i.e., $\frac{\partial \theta_v}{\partial z}$), and it decreases with increasing stratification. The buoyancy length scale is only active in stable conditions. The stability functions for heat and moisture $S_{h,m}$ contain empirical constants, which generally decrease with increasing stability, as they are inversely related to the Richardson number (Eq. 27 and 28 in Nakanishi and Niino, 2009). Finally, the dissipation rate is parameterized as $\varepsilon = \frac{q^3}{B_1 L}$, where B_1 is a closure constant ($B_1 = 24$ in the MYNN scheme).

4.2.3   Adding mass flux to MYNN

The MYNN Level 2.5 ED model determines turbulent mixing at each vertical level based on the gradients in scalars between immediately adjacent vertical levels (Eq. 4.1). When deep mixing due to larger eddies becomes important, the MYNN scheme has been shown to produce erroneous thermodynamic profiles (Huang et al., 2013b). Non-local models, such as the YSU and ACM2 schemes, account for this deep mixing by using a counter-gradient term (Hong et al., 2006) or a transilient mass flux matrix (Pleim, 2007). Another common approach is the EDMF framework, which decomposes the subgrid vertical mixing into local mixing through ED and non-local (mass-flux; MF) transport through convective plumes. Traditionally, PBL schemes, such as MYNN, model the turbulence within the PBL through only turbulent diffusion. In the EDMF framework, ED is used to model the turbulent transport in the non-convective environment, with an additional contribution from the convective mass flux.

Mass flux model overview

To represent non-local transport, we use the stochastic multi-plume EDMF model. The idea behind this model is that the horizontal subgrid domain is composed of an ensemble of convective plumes and the remaining non-convective environment. The multi-plume approach

is designed to account for the non-linear interactions between the plumes and the environment through the stochastic lateral entrainment. Following the same notation as Suselj et al. (2019a,b), the grid-mean value of any variable φ can be written as:

$$\overline{\varphi} = \sum_{n=1}^{N} a_{u_n} \varphi_{u_n} + \sum_{m=1}^{M} a_{d_m} \varphi_{d_m} + a_e \varphi_e, \tag{4.4}$$

where N/M is the total number of updrafts/downdrafts. The subscripts u_n, d_m, and e denote mean values from the $n-th$ updraft, $m-th$ downdraft, and the environment, while a_{u_n}, a_{d_m}, and a_e are the corresponding areas. In WRF, assuming the fractional area of updraft and downdraft are small, we approximate $\overline{\varphi} \approx \varphi_e$, and the turbulent flux can be written as (see Eqs. 7 in Suselj et al. (2019b)):

$$\overline{w'\varphi'} = \sum_{n=1}^{N} a_{u_n} (\varphi_{u_n} - \overline{\varphi})(w_{u_n} - \overline{w}) + \sum_{m=1}^{M} a_{d_m} (\varphi_{d_m} - \overline{\varphi})(w_{d_m} - \overline{w}) + a_e \overline{w'\varphi'}|_e, \tag{4.5}$$

where the vertical transport of non-convective environment $\overline{w'\varphi'}|_e$ is modeled using Equation 4.1.

Surface-driven updrafts

A version of EDMF including surface-driven updrafts (Olson et al., 2019) has been implemented as an add-on option in MYNN since WRF v3.8 and is used for NOAA's operational Rapid Refresh (RAP; Benjamin et al. (2016)) and High Resolution Rapid Refresh (HRRR) forecast systems. The original version of this dynamic multi-plume mass-flux scheme in WRF v3.8 ($bl\_mynn\_edmf = 1$) followed Suselj et al. (2013), but the version in the current WRF v4.0 contains considerable changes from the original form. We do not base our EDMF implementation ($bl\_mynn\_edmf = 3$) on what is currently available in WRF, but instead follow Suselj et al. (2013) and Suselj et al. (2019a,b). The numerical implementation is documented in Suselj et al. (2019b) (Appendix B).

The surface-driven updrafts are represented by an ensemble of steady-state plumes with

different initial conditions and stochastic entrainment rate profiles. The thermodynamic and dynamic properties of the n-th updraft $\varphi_{u_n} = \{\theta_{l,u_n}, q_{t,u_n}, u_{u_n}, v_{u_n}\}$ follow:

$$\frac{\partial \varphi_{u_n}}{\partial z} = \varepsilon_{u_n}(\overline{\varphi} - \varphi_{u_n}), \tag{4.6}$$

where ε_{u_n} is the entrainment rate. Note that an additional source term, due to microphysical processes in Suselj et al. (2019b), is not included here as it has no effect in non-precipitating STBL. The number of updrafts is fixed to ten ($n = 1, ..., N; N = 10$). The steady-state equation of the updraft velocity is:

$$\frac{1}{2}\frac{\partial w_{u_n}^2}{\partial z} = a_w B_{u_n} - (b_w \varepsilon_{u_n} + P_{w_{ud}})w_{u_n}^2, \tag{4.7}$$

where $a_w = 1$, $b_w = 1.5$ are model constants (de Roode et al., 2012, Suselj et al., 2019b, 2013). Variable $B_{u_n} = g(\theta_{v,u_n}/\overline{\theta}_v - 1)$ is the updraft buoyancy, and $\theta_v = \theta(1 + 0.61q_v - q_l)$ is the virtual potential temperature. $P_{w_{ud}}$ represents the dynamical pressure effects as updrafts approach the inversion and is parameterized as:

$$p_{w_{ud}} = \begin{cases} \frac{1 - exp((z_i - z)/z_{00} - 1)}{0.1(z_i - z)}, & z > (z_i - z_{00}) \\ 0, & z \leq (z_i - z_{00}), \end{cases} \tag{4.8}$$

where z_{00} denotes the distance from z_i when $p_{w_{ud}}$ starts to be in effect. For this work, we use $z_{00} = 100$ m. Assuming a normal distribution of the vertical velocity near the surface, the updrafts are thought to represent the positive tail of the distribution, between one and three standard deviations, divided into N bins. This results in a total updraft area of approximately 15% near the surface. The thermodynamic surface conditions for the updrafts are identical to Suselj et al. (2019a) (Appendix A). ε_{u_n} is the stochastic entrainment rate, computed as:

$$\varepsilon(\Delta z) = \frac{\varepsilon_0}{\Delta z}P\left(\frac{\Delta z}{L_\varepsilon}\right), \tag{4.9}$$

$$L_\varepsilon = L_0 exp(-c_{ent}z/z_i), \tag{4.10}$$

where $\varepsilon_0 = 0.2$ is the fractional mass of air entrained in a single entrainment event. $P(\lambda)$ is a random number drawn from the Poisson distribution with parameter $\lambda = \left(\frac{\Delta z}{L_\varepsilon}\right)$, which represents the number of entrainment events a single updraft experiences over height Δz. $L_0 = 100$ m denotes the distance a plume needs to travel to entrain once. The exponential term in Eqs. 4.10 represents the dynamic effect near strong temperature inversion, as the updrafts cannot penetrate above that layer and are assumed to entrain more and disintegrate; $c_{ent} = 0.5$ is a model constant controlling how fast entrainment length decreases with height. For STBL, we use the cloud-top height z_i (also known as the inversion height) to denote where this dynamic effect is at its strongest. z_i is defined as the last point near the PBL height where $q_l > 10^{-6}$ kg kg^{-1}, and cloud fraction is greater than 50%. This definition of z_i is identical to that in Olson et al. (2019), where they included an option for top-down buoyancy production in ED when Sc clouds were present. In the MYNN parameterization, there are three options to represent sub-grid cloudiness, which are controlled by *bl_mynn_cloudpdf* parameter. In this work, *bl_mynn_cloudpdf* $= 1$, for which a statistical partial condensation cloud scheme based on joint-Gaussian probability distribution function of θ_l and q_t is used (KuwanoYoshida et al., 2010). By default, the Gaussian PDFs are applied to the whole grid box (i.e., including non-convective environment and convective updrafts and downdrafts). We thus assume that Gaussian distributions of the thermodynamic variables (cf. Figure 4.1) yield reasonably accurate cloud cover and liquid water values for STBL. Cloud fraction would ideally be computed from Eqs. 4.4, and we use this approximation for simplicity. Note that for STBL, saturation conditions are usually met for most of the PDFs area.

While Suselj et al. (2013) did not include either the dynamical pressure effect (i.e. $P_{w_{ud}}$ term in Eqs. 4.7) or modification of entrainment length (L_ε) by proximity of inversion for the STBL simulation, we find that those modifications yield results that are more consistent with the plume statistics in LES, as discussed further in Section 4.3. The entrainment rate is the same for all variables (θ_{l,u_n}, q_{t,u_n}, u_{u_n} and v_{u_n}). Although Suselj et al. (2019b) used $\frac{1}{3}\varepsilon_{u_n}$ for u_{u_n} and v_{u_n},

we find that equal entrainment rate results in more consistent *u* and *v* profiles.

Since each updraft is characterized by different surface conditions and entrainment rates, the thermodynamic properties and termination heights also differ. Each plume is integrated independently in the vertical until the vertical velocity becomes negative. Condensation occurs within a plume if its total water mixing ratio exceeds the saturated water mixing ratio. Therefore, there exist dry and partly moist plumes among the *N* updrafts, and the fate of each plume is determined by its initial conditions, dynamical pressure effect, and lateral entrainment. Since each individual updraft is integrated independently, whenever the vertical velocity becomes negative and the updraft terminates, the total updraft area is reduced. This is common in regions with strong lateral entrainment rates.

Cloud-top triggered downdrafts

Several important physical processes are at play near the STBL top. Radiative and evaporative cooling produces cooled downdrafts and drives buoyant production of turbulence in the PBL. Entrainment from the free troposphere can impact downdrafts near the cloud-top: warm air from the free troposphere counteracts the radiative cooling and buoyant production of turbulence. When the PBL is less turbulent, the entrainment rate decreases, indicating a negative feedback loop (Wood, 2012). Surface-driven updrafts may also affect the downdrafts. As updrafts approach the inversion, they begin to diverge and can help initiate or enhance downdrafts (Davini et al., 2017, Kurowski et al., 2009). This enhances the downdraft vertical velocity and, in turn, the turbulence in the PBL. In the proposed 1D parameterization of downdrafts, those dependencies are important for the formulation of the downdraft initial conditions. Our downdraft parameterization in MYNN can be activated by specifying $bl\_mynn\_edmf\_dd = 1$ in the namelist. The numerical implementation follows Suselj et al. (2019b) (see Appendix C).

Similar to the surface-driven updrafts, downdrafts are also represented by an ensemble of steady-state plumes with stochastic lateral entrainment. The thermodynamic and dynamic

properties of the *m*-th downdraft $\varphi_{d_m} = \{\theta_{l,d_m}, q_{t,d_m}, u_{d_m}, v_{d_m}\}$ follow:

$$\frac{\partial \varphi_{d_m}}{\partial z} = -\varepsilon_{d_m}(\overline{\varphi} - \varphi_{d_m}).\tag{4.11}$$

$\varepsilon_{d_m} = \frac{\varepsilon_0}{\Delta z}P\left(\frac{\Delta z}{L_\varepsilon}\right)$ is the entrainment rate similar to Equation 4.9, where $L_\varepsilon = L_0$, and the values of L_0 and ε_0 are the same as for the updrafts. The entrainment rate is same for $\theta_{l,dm}$ and $q_{t,dm}$, however, it is increased 1.4 times for u_{dm} and v_{dm}. We find that increasing entrainment rate for momentum results in more consistent u and v profiles. The additional source term due to microphysical processes described in Suselj et al. (2019b) is neglected here. The number of downdrafts is fixed to ten ($m = 1,...,M$; $M = 10$). The steady-state equation of the downdraft velocity is identical to Suselj et al. (2019b) :

$$\frac{1}{2}\frac{\partial w_{d_m}^2}{\partial z} = a_w B_{d_m} + (b_w \varepsilon_{d_m} + p_{w_{dd}})w_{d_m}^2,\tag{4.12}$$

where $p_{w_{dd}}$ represents the dynamical pressure effects as downdrafts approach the surface and is parameterized as:

$$p_{w_{dd}} = \begin{cases} \frac{1 - exp(z/z_{00} - 1)}{2z}, & z \leq z_{00} \\ 0, & z > z_{00}, \end{cases}\tag{4.13}$$

where $z_{00} = 100$ m. This is equivalent to the dynamical pressure effect in updraft, except we replace z_i with 0.

We assume that downdrafts are initiated randomly in the upper half of the cloud layer. We avoid starting all downdrafts at z_i to avoid numerical instabilities in this region during the model spin-up time (not shown; see next section for details). Similarly to the updraft parameterization, we assume that the downdrafts represent the negative tail of the vertical velocity distribution which is assumed to be normal (between negative one and three standard deviations), resulting in a total downdraft area of approximately 15% slightly below cloud-top. The formulation of cloud-top conditions for downdrafts is similar to the formulation for surface-driven updrafts

(Suselj et al., 2019a). The difference lies in the parameterization of the variances of vertical velocity σ_w, total water mixing ratio σ_{q_t}, and virtual potential temperature σ_{θ_v}. The strength of downdraft vertical velocity is proportional to σ_w:

$$\sigma_w = c_1 w_{*,dd}, \tag{4.14}$$

where $c_1 = 0.3$ is a model constant. $w_{*,dd}$ is the the convective vertical velocity scale which takes into account both the intensity of surface-driven updrafts and cloud-top radiative cooling and is similar to the entrainment parametrization in Ghonima et al. (2017):

$$w_{*,dd} = \left[0.15(w_*^3 + 5u_*^3) + 0.35w_{rad}^3 \right]^{1/3}, \tag{4.15}$$

where $w_* \equiv (g/\theta_v)\overline{w'\theta_v'}|_s z_{top}$ is the Deardorff convective velocity scale, u_* is the surface friction velocity, and $w_{rad} \equiv (g/\theta_v)\overline{w'\theta_v'}|_{rad} z_{top}$ is a velocity scale based on the net radiative flux divergence at the cloud-top where $\overline{w'\theta_v'}|_{rad} = \frac{F_{rad}}{\rho c_p}$ (Lock and Macvean, 1999). In WRF, F_{rad} is defined as the radiative flux divergence between cloud-top and cloud base.

The framework for parameterizing σ_{q_t} and σ_{θ_v} is similar to that described by Kohler (2006). The downdraft initial total mixing ratio deficit is proportional to σ_{q_t}:

$$\sigma_{q_t} = c_2 q_*, \tag{4.16}$$

where $c_2 = 30$ is a model constant, and $q_* \equiv \frac{\overline{w'q_t'}_{ent}}{w_{rad}}$ is the moisture scale due to mixing with entrained air. The entrainment fluxes $\overline{w'\varphi'}_{ent}$ are modeled according to the flux-jump relation $\overline{w'\varphi'}_{ent} = w_e \Delta\varphi_{z_{inv}}$ (Lilly, 1968), where $\Delta\varphi_{z_{inv}} = \varphi_{z_{inv+1}} - \varphi_{z_{inv}}$ represents the jump value of the scalar φ across the inversion. w_e is the entrainment velocity and is parameterized following

Ghonima et al. (2017):

$$w_e = -\frac{\theta_{v0}}{g\Delta\theta_{v,inv}z_{inv}}\left[0.15(w_*^3 + 5u_*^3) + 0.35w_{rad}^3\right]. \tag{4.17}$$

In WRF, the jump in moisture, Δq_t, is defined as the difference in q_t at 700 hPa and the surface.

The downdraft initial virtual potential temperature is proportional to σ_{θ_v}:

$$\sigma_{\theta_v} = c_3\theta_{v,*}, \tag{4.18}$$

where $c_3 = 1$ is a model constant, and $\theta_{v,*} \equiv \frac{\overline{w'\theta'_{v_{ent}}}}{w_{*,rad}}$ is the buoyancy scale due to mixing with entrained air and radiative cooling. The jump in heat, $\Delta\theta_v$, is similar to (Wood and Bretherton, 2006):

$$\Delta\theta_v = (\theta_{v,700} - \theta_{v,0}) - \Gamma_{FT}(z_{700} - z_{inv}), \tag{4.19}$$

where $\theta_{v,700}$ is θ_v at p = 700 hPa, $\theta_{v,0}$ is θ_v at the surface, Γ_{FT} is the free tropospheric adiabat, and z_{700} is the height of the $p = 700$ hPa surface. Since difference in θ_v at 700 hPa and the surface is a combination of temperature increase across the capping inversion and the accumulated static stability between this inversion and the 700 hPa reference level, we subtract $\Gamma_{FT}(z_{700} - z_{inv})$ to focus on temperature jump across the inversion. We find this definition of inversion jumps to be more systematic and consistent than attempting to diagnose the exact point where the temperature inversion begins and ends.

Similar to the updrafts, equations for each downdraft are independently integrated in the vertical until the downdraft velocity vanishes. Condensation occurs within a downdraft if its total water mixing ratio exceeds the saturated water mixing ratio. Similarly to updrafts, there can exist dry and partly moist plumes among the M downdrafts, and the fate of each plume is determined by its initial conditions, dynamical pressure effect near the surface, and lateral entrainment. Since each individual downdraft is integrated independently, whenever vertical

Table 4.1: Summary of large eddy simulation setups in UCLA-LES, including uniform horizontal grid spacing $\Delta x, y$, vertical grid spacing at the inversion $\Delta z_{inv}[m]$, horizontal domain size $L_{x,y}$, and divergence of large-scale winds D.

Case	$\Delta x, y[m]$	$\Delta z_{inv}[m]$	z_{inv}	$L_{x,y}[m]$	$L_z[m]$	$D[s^{-1}]$
DYCOMS-II RF01	35	5	837	3,360	1568	3.75×10^{-6}
CGILS S12 Control	25	5	677	2,400	1572	1.68×10^{-6}

velocity becomes zero/positive and the downdraft terminates, the total downdraft area is reduced.

4.3 Design of Numerical Experiments

4.3.1 LES Setup

Large eddy simulations are performed using the UCLA-LES model (Stevens, 2010) and treated as "ground truth." Two idealized non-drizzling marine Sc cases are chosen as baseline simulations: the DYCOMS-II RF01 (Stevens et al., 2005) and CGILS S12 Control (Blossey et al., 2013) (hereinafter DYCOMS and CGILS). The experiments are set up following the respective intercomparison studies. Interactive radiation is treated differently in the two cases. Specifically, a simplified model of radiative forcing matching the δ-four stream transfer code (Stevens et al., 2005) is used in DYCOMS. As for CGILS, a full radiative transfer code is used, which utilizes Monte Carlo sampling of the spectral integration (Pincus and Stevens, 2009). The DYCOMS case is run for 4 h, and the CGILS case is run for 24 h. While we focus our analysis of the updraft and downdraft properties on nocturnal quasi-steady conditions (first 4 h), the 24 h simulation of CGILS provides reference to the generalization of the parameterization during the day. In both experiments, a non-uniform vertically-stretched grid is used with 5 m resolution around the inversion, and a several times coarser resolution in the horizontal. This LES setup is identical to that in Ghonima et al. (2017). A summary of the model setups is provided in Table 4.1.

Determining plume properties

Simulation outputs are stored at one minute intervals from hour three to four in order to diagnose updraft and downdraft properties. The statistics are averaged over one hour. We use the joint normal probability density function (PDF) between vertical velocity w, total water mixing ratio ($q_t = q_v + q_l$), virtual potential temperature ($\theta_v = \theta(1 + 0.61q_v - q_l)$), and liquid water potential temperature ($\theta_l = \theta - (L_v q_l)(c_p \pi)^{-1}$) to define LES updrafts and downdrafts. L_v is the latent heat of vaporization, c_{pd} is the specific heat of dry air at constant pressure, π is the Exner function, and subscripts are v for vapor, l for liquid. We define the normalized variable to be $\varphi' = \frac{\varphi - \overline{\varphi}}{\sigma_\varphi}$, where $\overline{\varphi}$ is the slab mean and σ_φ is the standard deviation of φ. By carefully investigating the joint PDFs, we define updrafts to be the LES grid-points that conform to the following conditions: $w' > 1$, $q_t' > 0$, and either $\theta_l' < 0$ or $\theta_v' > 0$. We define downdrafts to be $w' < 0$, $q_t' < -1$, and $\theta_l' > 0$. Specifically, this definition of downdrafts captures the negative tail in the joint normal PDF. Figure 4.1 shows the joint normal PDF for DYCOMS at a normalized height close to the cloud-top ($z/z_i = 0.97$). A strong negative tail is observed in Figure4.1A, where $w' < 0$ and $q_t' < -1$. We also confirm that grid-points satisfying these criteria correspond well with negatively buoyant ($\theta_v' < 0$) parcels that are warmer in terms of the liquid water potential temperature ($\theta_l' > 0$). While the definitions of updraft and downdraft used here are not as rigorous as in Brient et al. (2019), Chinita et al. (2017), Davini et al. (2017), we find that the overall properties are consistent with their study.

The mean downdraft and updraft properties are shown in Figure 4.2 for DYCOMS and Figure 4.3 for CGILS. Updraft and downdraft areas are comparable in the middle of the PBL (Figure 4.2A & 4.3A), with updrafts decreasing near cloud-top and downdrafts decreasing before reaching the surface. Figure 4.2B & C and Figure 4.3B & C show partial contributions to the total heat and moisture fluxes from the environment, updrafts, and downdrafts. Similar results are found in both STBL cases: cloud-top entrainment heat flux is largely from updrafts; the peak in downdraft heat and moisture transport is slightly below the peak in updrafts ($\approx$100 m
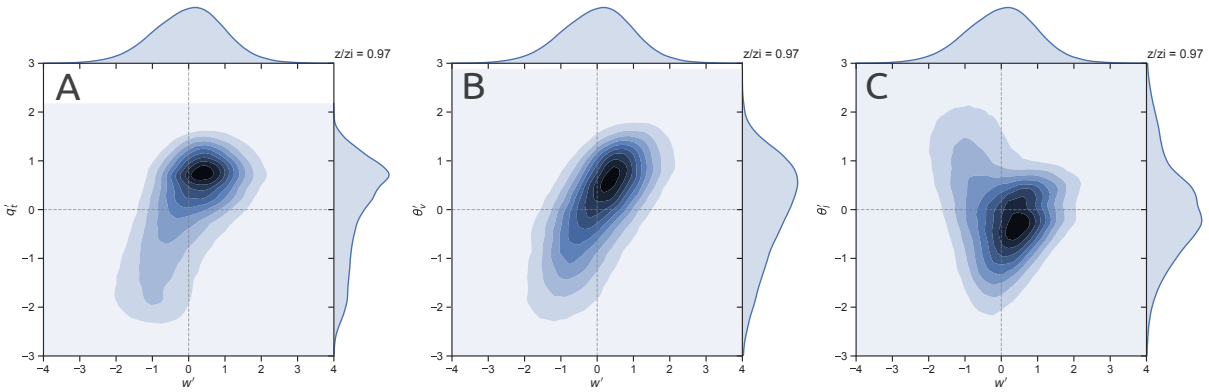
Figure 4.1: Joint probability density function (PDF) of normalized vertical velocity fluctuations w' and (A) normalized total mixing ratio fluctuations q_t', (B) normalized virtual potential temperature fluctuations θ_v', and (C) normalized liquid water potential temperature fluctuations θ_l' near cloud-top ($z/z_i = 0.97$). Each tick represents one standard deviation away from the mean. LES results from hour 3-4 are shown.

lower); heat and moisture transport from downdrafts is stronger than updrafts in cloudy region; environmental mean of w, θ_l, θ_v, q_t, and q_l is very close to the grid mean. Both cases have similar updraft and downdraft properties: downdrafts terminate before reaching the surface (Figure 4.2A & Figure 4.3A); updraft and downdraft vertical velocity are approximately a mirror image of each other (Figure 4.2D & Figure 4.3D); downdrafts become negatively buoyant ($\theta_v' < 0$) slightly below cloud-top (Figure 4.2F & Figure 4.3F); updrafts correspond to thicker cloud regions and downdrafts are co-located with cloud holes (Figure 4.2H & Figure 4.3H). Since the peak in downdraft heat and moisture transport is slightly below the peak in updraft, the choice of starting downdrafts randomly between cloud-top and half way through cloud-base is consistent with the findings in LES.

The properties shown in these two STBL cases compare well to the case in Brient et al. (2019), where the First ISCCP Regional Experiment (FIRE) study was simulated for 24 h to study the diurnal cycle of coherent updraft and downdraft properties. Specifically, the nighttime results of Brient et al. (2019) show that the areas of updrafts and downdrafts are comparable in the middle of the PBL (around 12%) and the downdraft area decreases quickly to zero below 100 m, which corresponds well with our findings for DYCOMS. CGILS results show a slightly
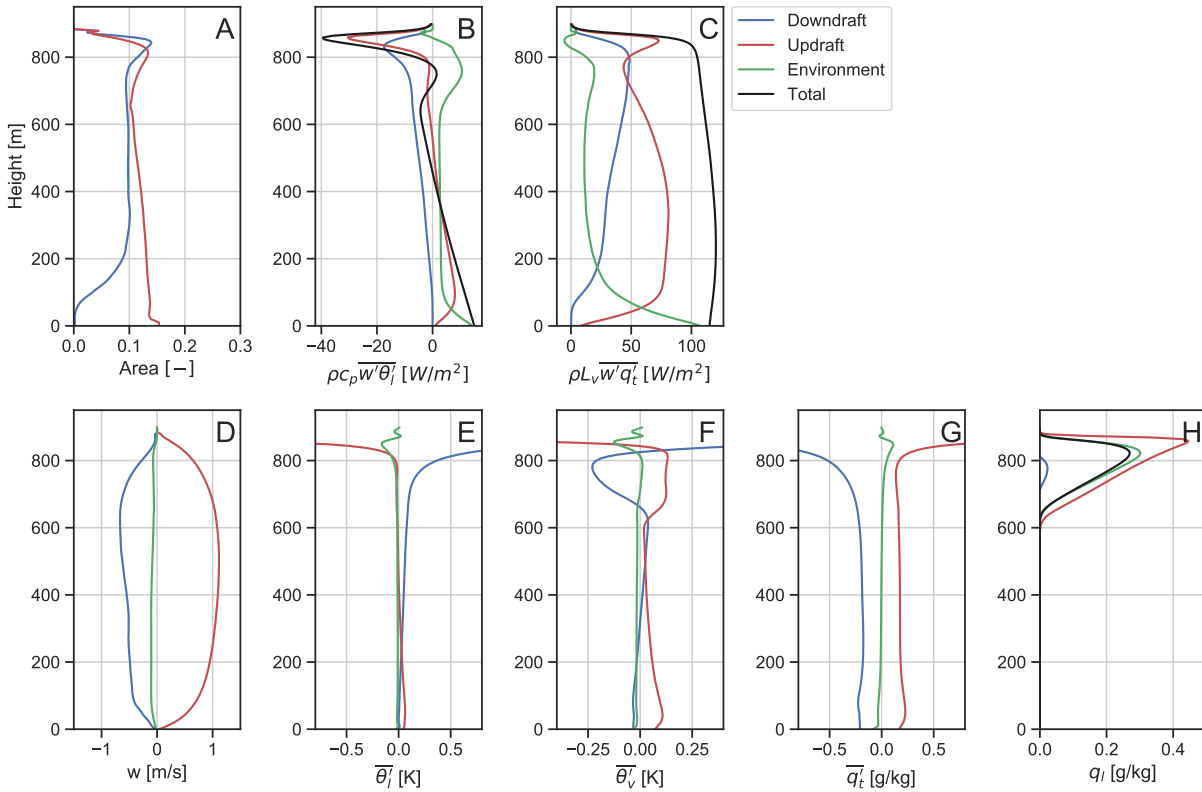
Figure 4.2: DYCOMS case: Updraft and downdraft area (A), vertical velocity (D), difference from mean liquid water potential temperature (E), virtual potential temperature (F), total water mixing ratio (G), and actual liquid water mixing ratio (H). (B) and (C) show the contribution to total heat and moisture flux from updrafts, downdrafts, and the environment. For this and all following figures, WRF results from hour 3-4 are shown.

smaller downdraft area in the middle of the PBL (around 9%). The turbulent heat flux in Brient et al. (2019) shows that the transport of heat by updrafts is the strongest at cloud-top, the peak of the downdraft heat transport is slightly below that for the updrafts ($\approx$50 m lower), and the heat transport by updrafts in cloudy region is nearly zero when downdrafts dominate. This corresponds well with DYCOMS, while updrafts in CGILS have a slightly positive heat transport in the cloudy region. As for the turbulent moisture flux, Brient et al. (2019) shows that updrafts dominate from the surface up to slightly above cloud base, while downdrafts dominate in the cloud layer. Moisture flux is similar in DYCOMS and CGILS, but our results show a positive peak of updraft moisture flux near cloud-top, making the updraft contribution to the moisture flux a dominating
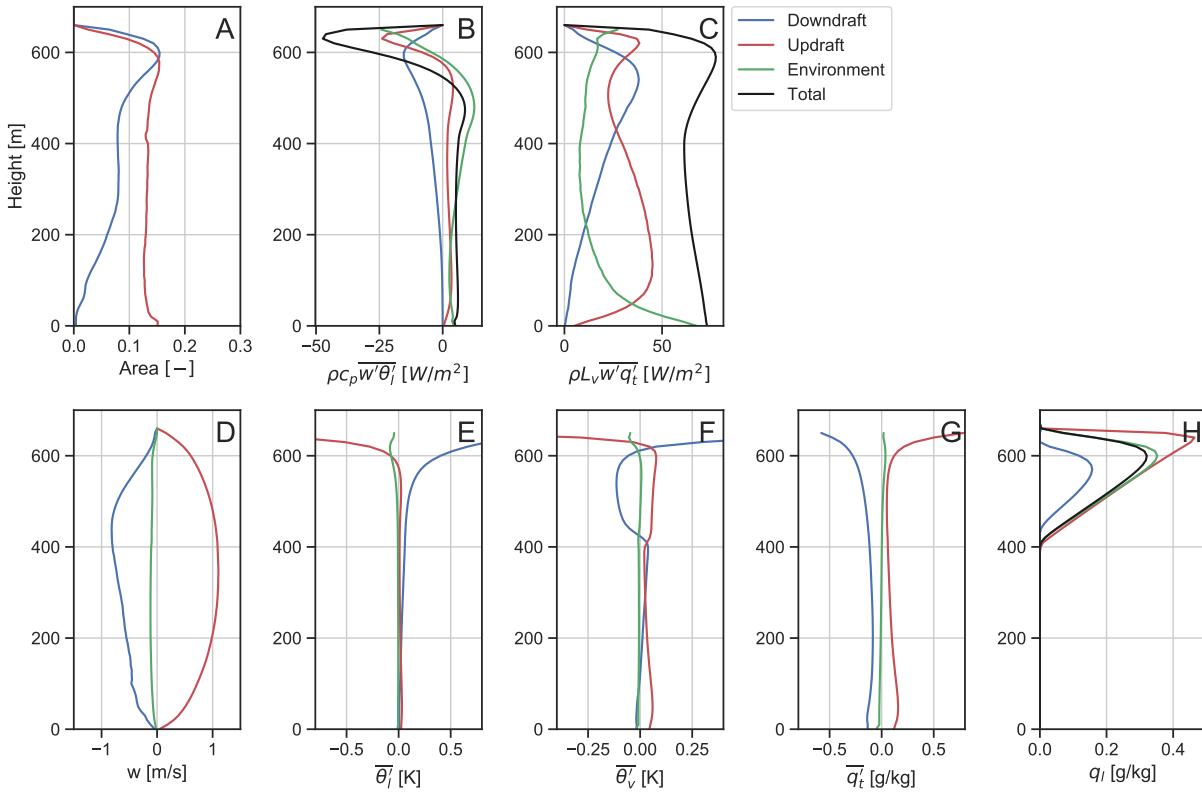
Figure 4.3: CGILS case: Updraft and downdraft area (A), vertical velocity (D), difference from mean liquid water potential temperature (E), virtual potential temperature (F), total water mixing ratio (G), and actual liquid water mixing ratio (H). (B) and (C) show the contribution to total heat and moisture flux from updrafts, downdrafts, and the environment.

term around cloud-top. Chinita et al. (2017) shows large differences in the contribution of updrafts and downdrafts to total flux for DYCOMS in the cloud layer. In general, they find that updrafts account for most of the organized motions near the surface, while downdrafts are more important near the boundary layer top. While the overall properties are similar, updraft and downdraft areas in Chinita et al. (2017) are 5 to 10 % larger.

4.3.2   WRF single column model

DYCOMS and CGILS case are simulated using the Weather Research and Forecasting (WRF) v4.0 single column model (SCM) and compared against LES. Initial conditions and forcing are identical to that in LES (i.e., fixed surface fluxes for DYCOMS and CGILS, large-scale

subsidence as in Table 4.1) and was used previously in Ghonima et al. (2017). The SCM vertical domain includes 116 levels to resolve the lowest 12 km of the troposphere, which comes out to be $\Delta z \approx 20$ m in the first 1 km. A simulation time step of 40 s is used. In Section 5.44.4.3, we show that results are insensitive when the time step is decreased. Three different versions of one PBL scheme are used to determine the importance of the introduced changes: 1) the original Mellor-Yamada-Nakanishi-Niino scheme (MYNN; hereinafter ED) (Nakanishi and Niino, 2006, 2009), 2) MYNN with updrafts ($EDMF_U$), and 3) MYNN with updrafts and downdrafts ($EDMF_{UD}$). For $EDMF_U$ and $EDMF_{UD}$, the MYNN scheme is used as a parameterization of local transport in the non-convective environment. The radiation scheme is RRTMG (Iacono et al., 2008). No microphysics or cumulus schemes are used since both cases represent non-precipitating STBL.

4.4 Results

4.4.1 DYCOMS-II RF01

Figure 4.4 shows the mean fields of θ_l, q_t, q_l, u, n, heat flux ($\rho c_p \overline{w'\theta_l'}$), and moisture flux ($\rho L_v \overline{w'q_t'}$). Figure 4.5 shows the time series of liquid water path (LWP), boundary layer averaged heat (θ_l), and moisture (q_t) for the three tested PBL schemes and LES. ED has a cold and moist bias in the PBL (Figure 4.5B and C), resulting in an overestimation of LWP for the entire simulation. The underestimation of entrainment flux is likely the cause of this behavior as ED fails to model heat and moisture transport between the free-troposphere and the PBL (Figure 4.4G & H). Moreover, ED does not have a transition in horizontal wind between the PBL and the free troposphere, indicating that ED does not capture the momentum transport properly (Figure 4.4E & F). $EDMF_U$ has a weaker cold and moist bias, and the bias in LWP is minimal during hour 3 to 4. However, inversion base height is slightly lower than ED. This is a result of updrafts overshooting into the free troposphere in the early time of the simulation, mixing out the initial inversion base height. $EDMF_{UD}$ has a much smaller bias in boundary layer averaged

70

heat and moisture and has a more well-mixed profile in q_t than EDMF$_U$. Inversion base height is also slightly lower in EDMF$_{UD}$. Both EDMF$_U$ and EDMF$_{UD}$ capture the entrainment heat and moisture flux well. Among the three tested PBL schemes, EDMF$_U$ has the best match in horizontal wind in the PBL, and EDMF$_{UD}$ overestimates u but underestimates v in the PBL.
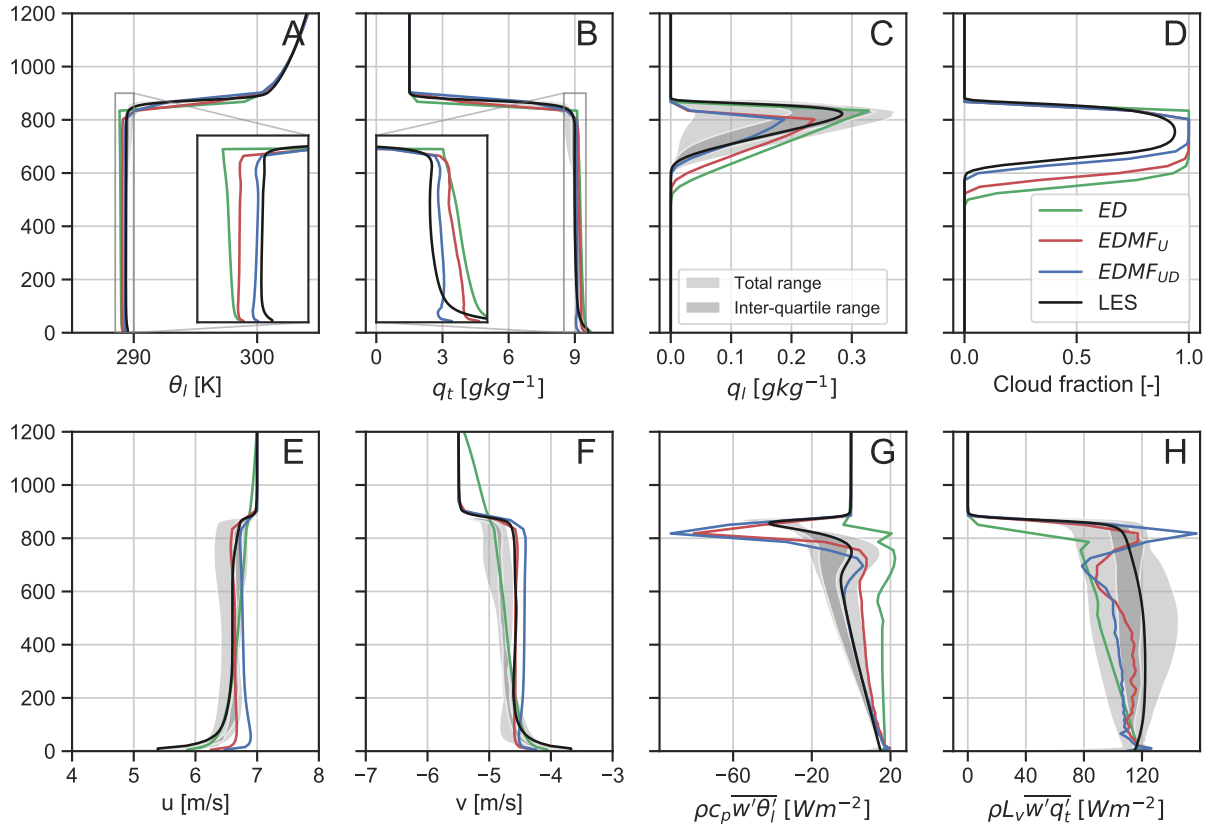
Figure 4.4: DYCOMS case: WRF SCM hour 3-4 averaged results for mean field of liquid water potential temperature (A), total water mixing ratio (B), liquid water mixing ratio (C), cloud fraction (D), zonal wind (E), meridional wind (F), total heat flux (E), and total moisture flux (H). The black line is the result from UCLA-LES, while the shaded range is from an LES inter-comparison study Stevens et al. (2005). Note that grid-mean liquid water mixing ratio is calculated using a statistical partial condensation ($bl\_mynn\_cloudpdf = 1$), the condensation routine is called at the end of PBL scheme after mixing from both ED and MF are completed.

Figures 4.6 and 4.7 show the vertical flux contribution from the individual components: environment (ED), updraft, and downdraft. Figure 4.6 is for EDMF$_U$, which includes only ED and updraft. Note that LES transport in 4.6A & D includes LES environmental and downdraft transport because in the case of updrafts only, the remaining area is considered to be the environment and
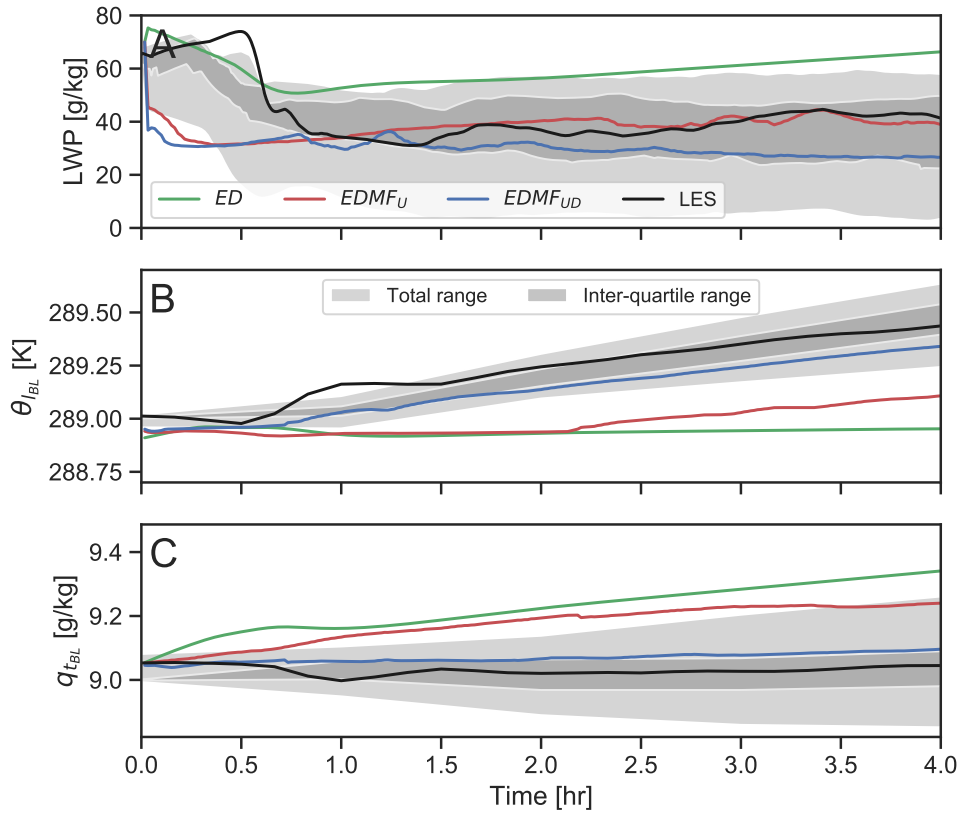
Figure 4.5: DYCOMS case: time series of liquid water path, boundary layer averaged heat (θ_l), and moisture (q_t).

should therefore be modeled by ED. Updraft contribution to the heat flux matches the profile in LES well, however it is overestimated in most of PBL and the cloud-top entrainment heat flux is too strong. It is important to note that cloud-top entrainment is not fully understood even in LES. We find here that even though entrainment heat flux appears to be strong, boundary layer averaged temperature in $EDMF_U$ is still too cold compared to LES (Figure 4.5B). However, $EDMF_U$ produces a warmer boundary layer compared to ED, which strongly underestimates entrainment heat flux. Updraft contribution to the moisture flux is overestimated throughout the PBL, but ED component is underestimated and the total moisture flux matches LES well. The initial updraft starting θ_l and q_t are stronger than LES (not shown) and eventually leads to overestimation of moisture flux. This indicates that the formulation of updraft surface condition in STBL may be different from shallow convection since we retain the same updraft starting condition used in

Suselj et al. (2019a). In shallow convection, surface fluxes are the main driver for updraft surface conditions. Whether other physical processes are at play in the parameterization of updraft surface conditions in STBL should be investigated in the future. We find that in the current configuration, ED compensates for the overestimation of updraft moisture flux, resulting in a good match with LES in the total moisture flux.
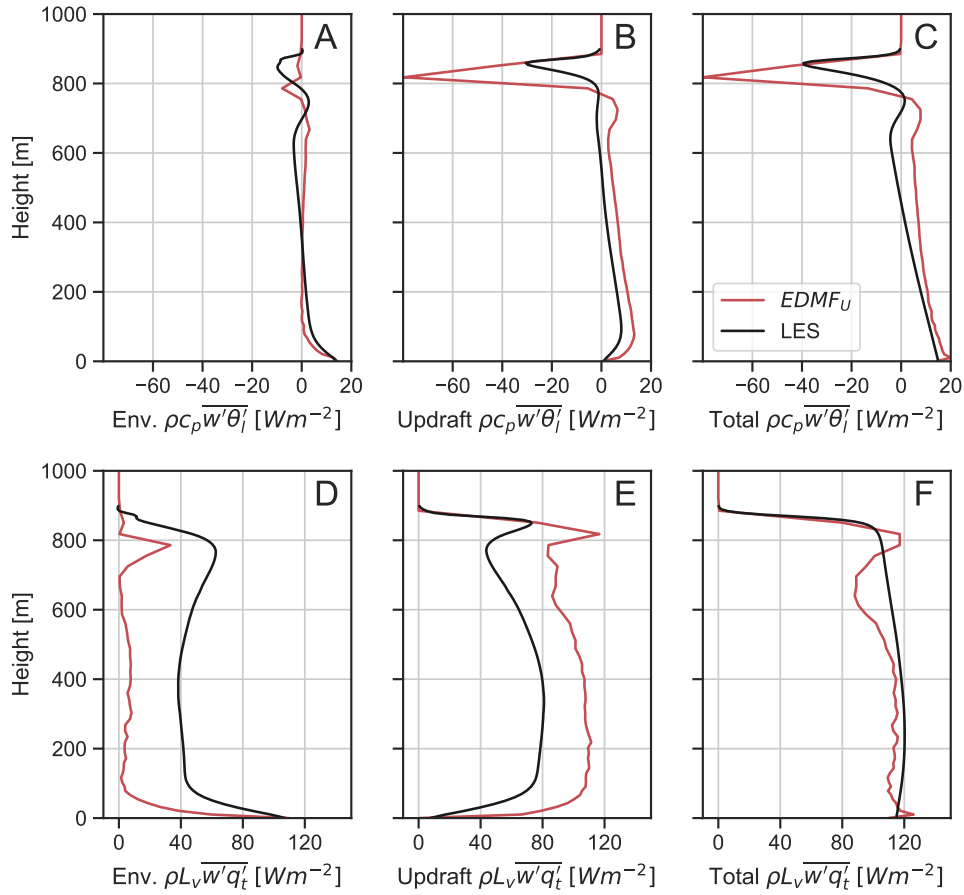
Figure 4.6: DYCOMS case: WRF SCM heat and moisture flux contribution from eddy diffusivity (A and D), updraft mass flux (B and E), and total flux (C and F).

Based on 800 additional simulations, exploring the parameter space, with different lateral entrainment rates and dynamical effects (varying L_0 and c_{ent} in Eq. 4.10 from and 10 to 100 m 0.5 to 5 m^{-1}, as well as varying z_{00} in Eq. 4.8 from 50 to 200 m; not shown), we observe that the most important impact of the updraft is the transport near cloud-top because ED models an insufficient
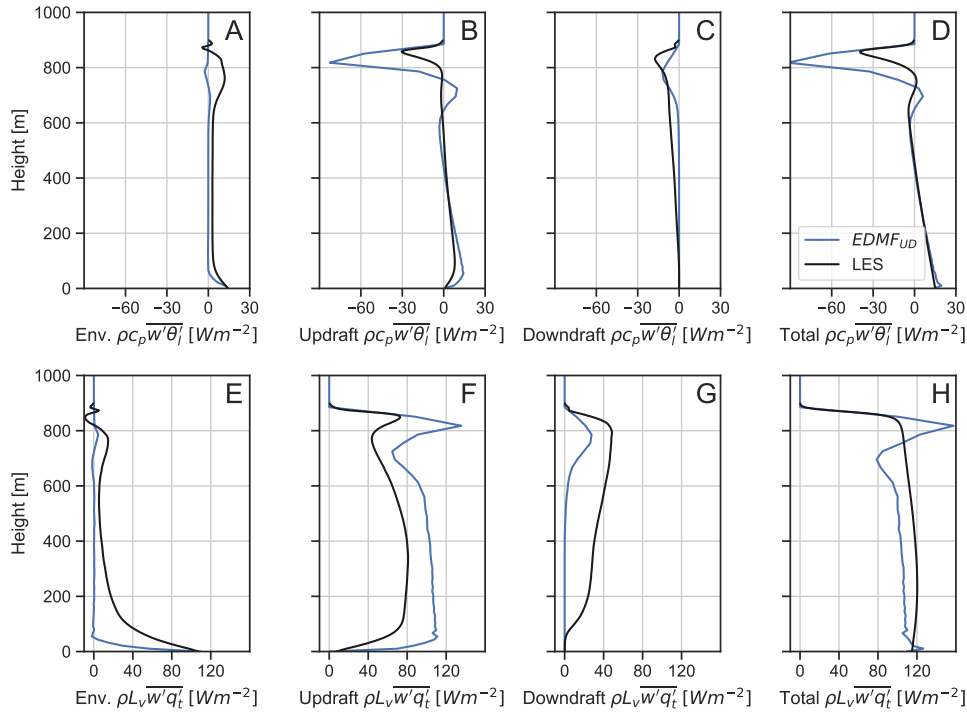
Figure 4.7: DYCOMS case: WRF SCM heat and moisture flux contribution from eddy diffusivity (A and E), updraft mass flux (B and F), downdraft mass flux (C and G), and total flux (D and H).

heat and moisture transport in this location, causing a cold and moist bias. Additionally, ED does not accurately represent a well-mixed layer, while EDMF$_U$ has a better well-mixed profile in both θ_l and q_t. The final configuration was chosen to have the best match in the mean field of θ_l, q_t, and total heat and moisture transport with LES.

For EDMF$_{UD}$, Figure 4.7 shows partial contributions to the total transport from ED, updrafts, and downdrafts. Comparing Figures 4.6 and 4.7, we argue that the downdraft transport is implicitly included in the ED contribution in EDMF$_U$ (Figure 4.6A & D) as the sum of heat and moisture transport for EDMF$_U$ versus EDMF$_{UD}$ is similar. Averaged plume properties from EDMF$_{UD}$ are shown in Figure 4.8. For downdraft contribution to total fluxes, EDMF$_{UD}$ underestimates the strength in heat and moisture flux. More spefically, downdraft heat transport decreases too quickly before reaching the surface (Figure 4.7C). For moisture tansport, downdraft q_t also decrease quickly, and the starting downdraft q_t is underestimated (Figure 4.8C). Updraft

contribution to heat transport (Figure 4.7B) is similar to that in EDMF$_U$, and they both slightly overestimate compared to LES. This can be seen in the overestimation of updraft area and vertical velocity (Figure 4.8A, B), and is a result of the positive bias in updraft starting surface conditions, espicially updraft starting vertical velocity. For updraft moisture transport, updrafts in EDMF$_{UD}$ do not overestimate as strongly as EDMF$_U$. This is likely due to downdrafts transporting dry and warm air in the PBL and causing updrafts to mix differently. On top of that, the mean fields of θ_l and q_t are different in EDMF$_U$ and EDMF$_{UD}$. Note that since the definition of updrafts and downdrafts in LES is somewhat arbitrary, the total transport should be the main indicator of success for a parameterization. Nevertheless, the definition of updrafts and downdrafts as in Section 4.3 is a reference point for bench-marking updraft and downdraft parameterizations. Overall, general agreement of plume properties are found between the SCMs and LES. For DYCOMS, downdraft transport decreases too quickly for both heat and moisture. We find that modeling downdraft transport in the upper part of the boundary layer correctly is more important than retaining downdraft throughout the PBL. The mean fields respond more to changes in turbulent transport in the upper part of the PBL. Indeed, the q_t profile is most well-mixed in EDMF$_{UD}$, signaling the importance of downdraft moisture transport. This is consistent with the hypothesis in Suselj et al. (2013), suggesting that the inclusion of downdrafts could increase vertical mixing in the upper part of the boundary layer. In STBL, mixing from the surface provides moisture and entrainment from the free troposphere dries the boundary layer. However, in the heat profile, both the surface and entrainment from the free troposphere heats the boundary layer. We find here that downdrafts help provide stronger moisture mixing near cloud-top and keep the bias in total moisture low. In addition, EDMF$_{UD}$ has the least bias in boundary layer averged θ_l, as downdrafts also contribute to transporting warm air in the PBL.

Downdraft model coefficients and final lateral entrainment configuration are chosen to have the best match against LES in the mean field of θ_l, q_t, u, and v. EDMF$_U$ and EDMF$_{UD}$ have the same updraft lateral entrainment configuration.
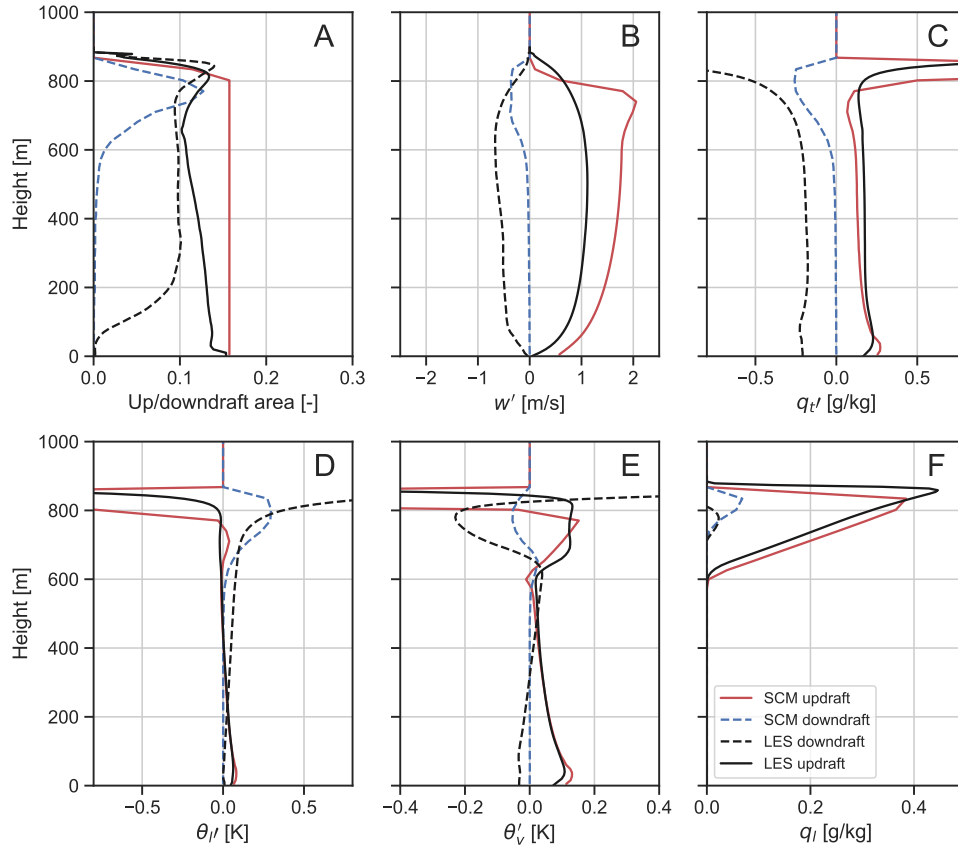
Figure 4.8: DYCOMS case: WRF EDMF$_{UD}$ plume properties of (A) area, (B) vertical velocity perturbations, (C) total water mixing ratio perturbations, (D) liquid water potential temperature perturbations, (E) virtual potential temperature perturbations, and (F) liquid water content for both updraft (red solid) and downdraft (blue dashed). LES results as in Fig 4.2 are in solid dark (updraft) and dashed dark (downdraft) line.

Comparing EDMF$_U$ with SCM results from Suselj et al. (2013), a resemblance of the updraft transport of heat and moisture is found. The formulations of updrafts are identical except for the added entrainment and dynamical pressure effect near cloud-top in EDMF$_U$. It is no surprise that some differences are seen, given the different assumptions made in ED. Specifically, the vertical transport in the middle of the boundary layer is different in the two models. While EDMF$_U$ shows positive transport from updraft in the cloudy region for heat, the updraft model in Suselj et al. (2013) shows a negative heat transport. For moisture, EDMF$_U$ produces stronger transport. This is likely due to the added entrainment dynamic effect in our

updraft model, different subgrid cloud assumption, and different ED model for the non-convective environment. In the end, the total heat and moisture transport is similar between the two models as ED compensates for the difference, and they both match LES well.

Comparing EDMF_{UD} with SCM results from Han and Bretherton (2019), we found contrary conclusions for the effect of the downdraft parameterization. While Han and Bretherton (2019) found a slight overprediction for θ_l and overmixing for q_t in their DYCOMS experiment, we found slight underprediction for θ_l and undermixing for q_t.

4.4.2 CGILS S12 Control

Figure 4.9 shows the mean fields of θ_l, q_t, q_l, u, n, heat flux ($\rho c_p \overline{w'\theta_l'}$), and moisture flux ($\rho L_v \overline{w'q_t'}$) during hr 3 to 4, and the 24 h time series of liquid water path (LWP), boundary layer averaged heat (θ_l), and moisture (q_t) for the three tested PBL schemes are shown in Figure 4.10. ED shows a strong cold and moist bias throughout the entire simulation. For EDMF_U, boundary averaged heat and moisture both follow LES closely up to hr 10, then the moisture does not increase as much as in LES. Around hr 15, EDMF_U begins to cool when compared to LES. This is likely a result of different radiation treatment used in LES and WRF. For EDMF_{UD}, similar trend is observed. Boundary layer averaged heat is warmer and moisture is direr than EDMF_U. Both EDMF_U and EDMF_{UD} match LWP in LES well. EDMF_{UD} produces a slightly thinner cloud in the first half of the simulation, while EDMF_U produces a slightly thicker cloud in the second half of the simulation.

During hours 3 to 4, EDMF_U and EDMF_{UD} show small bias in heat and moisture profile, whereas ED is too cold and too moist. This causes the overestimation of LWP in ED. The cloud-top height in EDMF_{UD} is one grid point above ED, likely due to the stronger entrainment flux near cloud-top from mass-flux. EDMF_{UD} overestimates u and underestimates v in the PBL. ED shows similar results as DYCOMS, where the horizontal wind does not have a strong transition between the PBL and the free troposphere. EDMF_U shows a very good match in
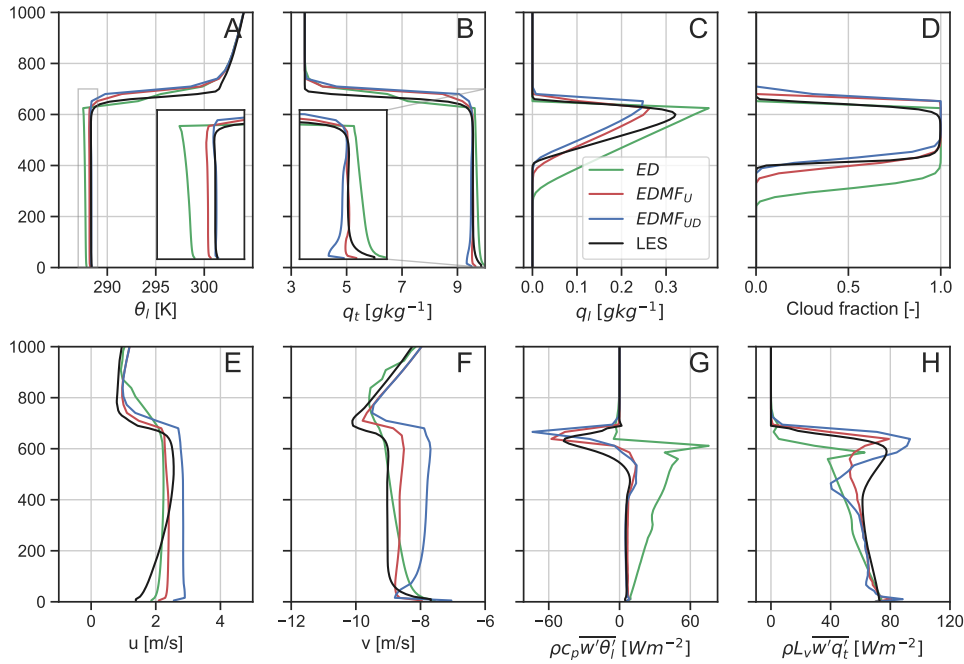
Figure 4.9: CGILS case: WRF SCM hour 3-4 averaged results for mean field of liquid water potential temperature (A), total water mixing ratio (B), liquid water mixing ratio (C), cloud fraction (D), zonal wind (E), meridional wind (F), total heat flux (E), and total moisture flux (H).

total heat and moisture transport, while EDMF$_{UD}$ has a slightly stronger moisture transport near cloud-top. Similar to DYCOMS, ED does not capture cloud-top entrainment flux. Figures 4.11 and 4.12 show the vertical flux contribution from each individual component: environment (ED), updrafts, and downdrafts. In both EDMF$_U$ and EDMF$_{UD}$, updraft heat and moisture transport are overestimated. However, in the presence of downdrafts, updraft moisture transport decreases more strongly in-cloud. Downdrafts in EDMF$_{UD}$ partially compensate for these changes, resulting in a similar total transport. Averaged plume properties from EDMF$_{UD}$ are shown in Figure 4.13. In CGILS, a good agreement of plume properties is found between the SCMs and LES. Again, we find that simulation results are more sensitive to the modeling of downdraft transport in the upper part of the PBL. In the end, we select model parameters that result in realistic mean profiles of θ_l, q_t, u, and v for both DYCOMS and CGILS. While the parameterized downdrafts terminate too quickly in DYCOMS, we find that they mostly reach the surface in CGILS.
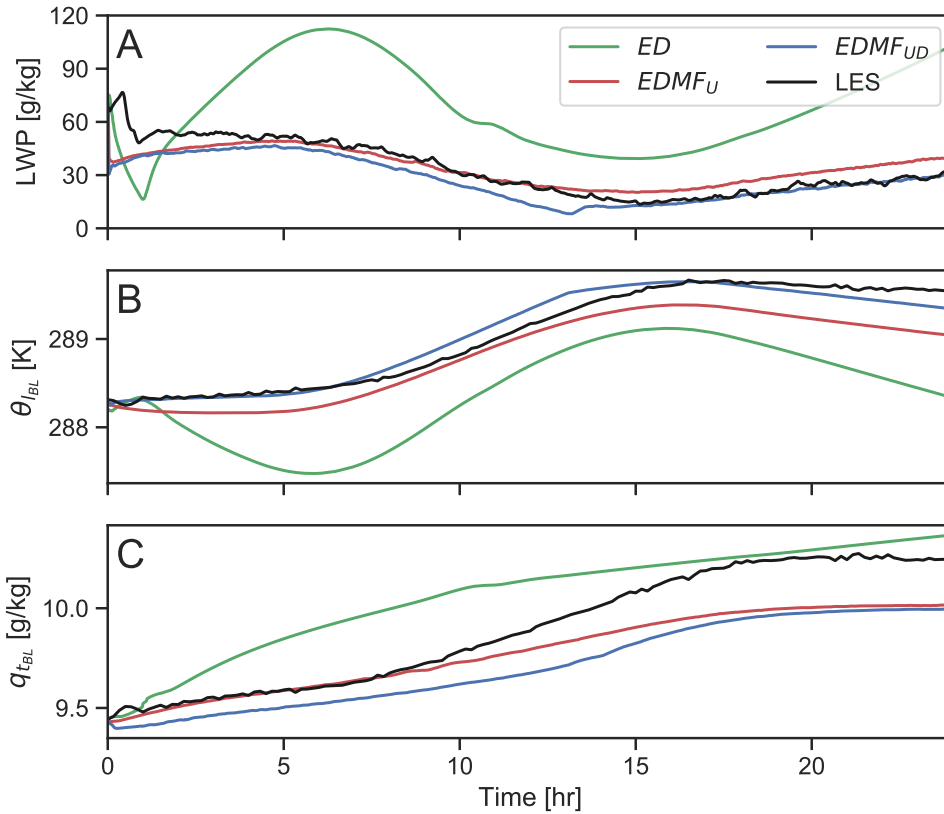
Figure 4.10: CGILS case: time series of liquid water path, boundary layer averaged heat (θ_l), and moisture (q_t).

In the present study, we develop our updraft and downdraft parameterization using their nocturnal properties. The 24 h simulation of CGILS suggests that updrafts and downdrafts may play different roles during the day time. This is also observed in the study done by Brient et al. (2019). Parameterization of updrafts and downdrafts during the day should be investigated in the future.

4.4.3 Simulation time step and run-time

To test the numerical stability of the scheme and the convergence of the results, we also run simulations with different time steps: 5, 10, 20, 30, and 40 s as shown in Fig. 4.14. Note that the figures shown in this study use a time step of 40 s. The obtained results confirm that
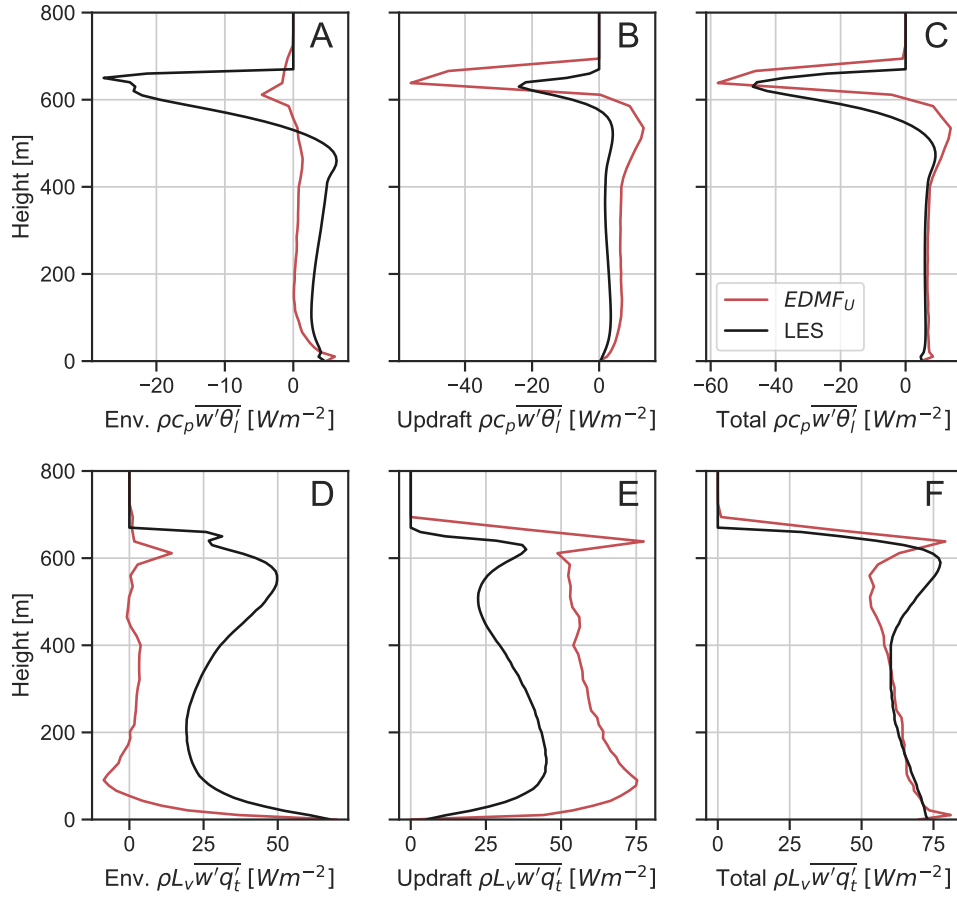
Figure 4.11: CGILS case: WRF SCM heat and moisture flux contribution from eddy diffusivity (A and D), updraft mass flux (B and E), and total flux (C and F).

both EDMF$_U$ and EDMF$_{UD}$ are not sensitive to the imposed time step changes, proving high robustness of the scheme. The LWP, and the boundary-layer-averaged heat and moisture amounts all converge to the same values at the end of the simulation. Additionally, we record simulation run times normalized by the ED-simulation run time for different time steps (Table 4.2). On average, including the updrafts slows the simulation down by approximately 5%, while including both updrafts and downdrafts slows it down by 7%. This indicates that EDMF is a numerically inexpensive scheme.
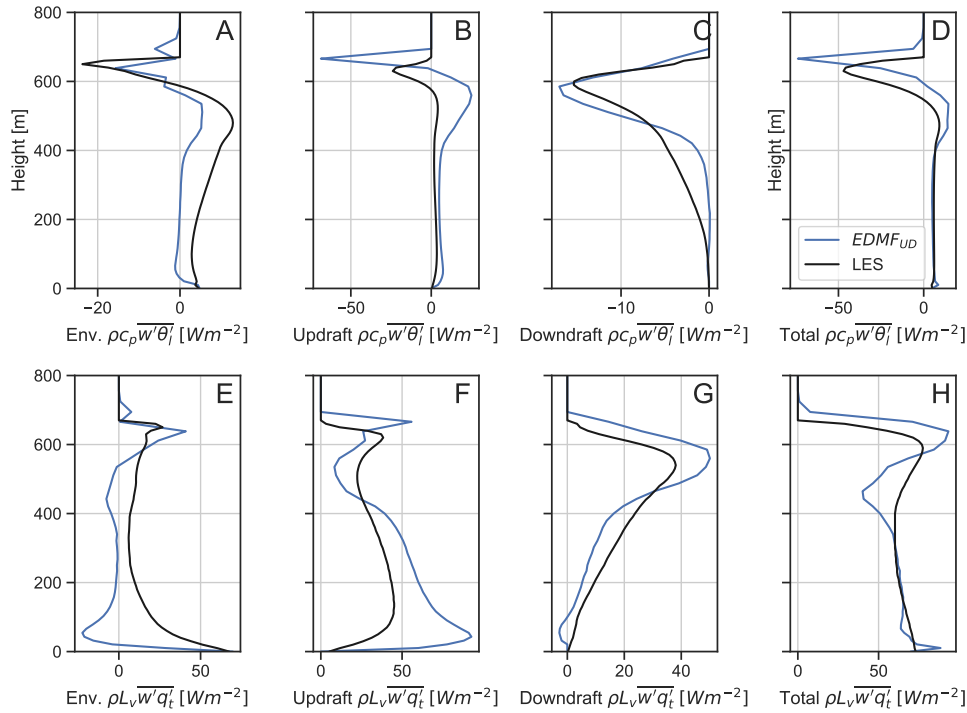
Figure 4.12: CGILS case: WRF SCM heat and moisutre flux from individual component– eddy diffusivity (A and E), updraft mass flux (B and F), downdraft mass flux (C and G), and total flux (D and H).

Table 4.2: EDMF$_U$ and EDMF$_{UD}$ run time normalized by ED using different time steps.

Time step [s]	5	10	20	30	40	Avg
EDMF$_U$	1.07	1.01	1.02	1.11	1.04	1.05
EDMF$_{UD}$	1.10	1.01	1.04	1.10	1.08	1.07

4.5 Summary and conclusions

In this study, we investigated the role of non-local transport on the development and maintenance of the STBL in coarse-resolution atmospheric models. A special emphasis has been put on the evaluation of downdraft contribution, recently suggested as an important missing element of convection/turbulence parameterizations (Brient et al., 2019, Chinita et al., 2017, Davini et al., 2017). A new parameterization of cloud-top triggered downdrafts has been proposed along with a complementary parameterization of surface-driven updrafts. The parameterization was validated against large-eddy simulations of two marine stratocumulus cases: DYCOMS and
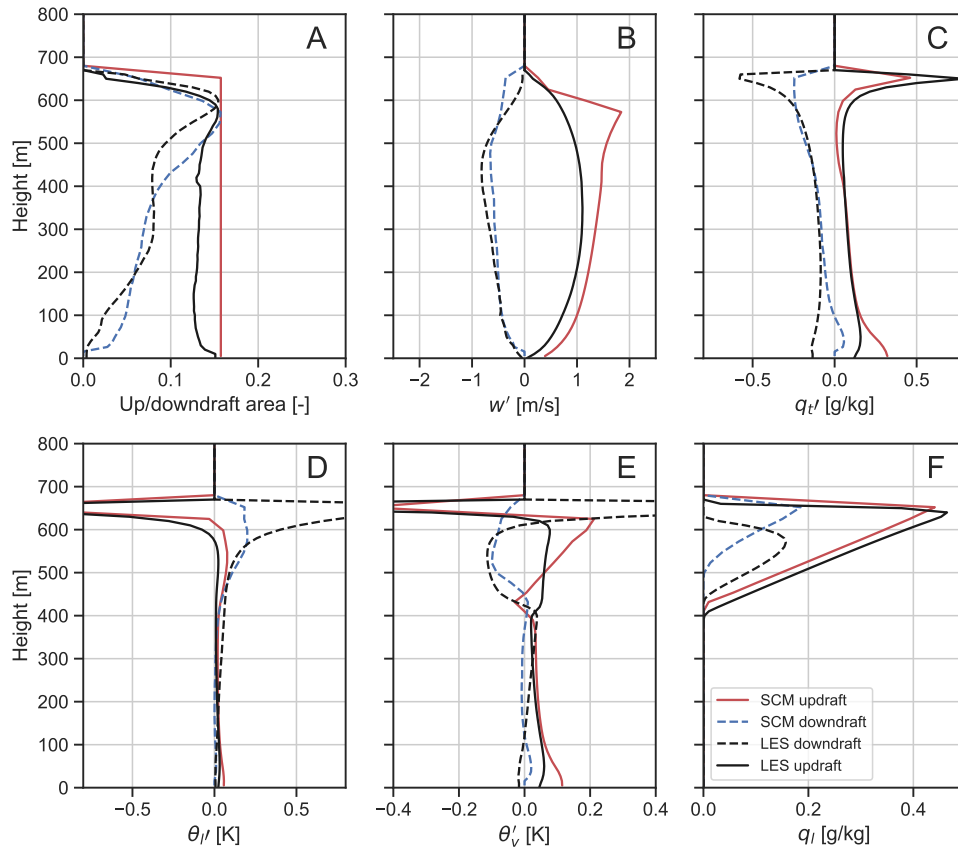
Figure 4.13: CGILS case: WRF EDMF$_{UD}$ plume properties of (A) area, (B) vertical velocity perturbations, (C) total water mixing ratio perturbations, (D) liquid water potential temperature perturbations, (E) virtual potential temperature perturbations, and (F) liquid water content for both updraft (red solid) and downdraft (blue dashed). LES results as in Fig 4.3 are in solid dark (updraft) and dashed dark (downdraft) line.

CGILS. The applied non-local mass-flux scheme is part of the stochastic multi-plume EDMF approach decomposing the turbulence into the local and non-local contributions. The local transport in the boundary layer is represented by the MYNN scheme. The EDMF scheme has been implemented and tested in the WRF single-column modeling framework.

In the new parameterization, the thermodynamic and dynamic properties of downdrafts are controlled by stochastic lateral entrainment affecting their dilution along the vertical development. The number of downdrafts is fixed to 10 for a time step of 40 s, and all downdrafts are assumed to start randomly in the upper half of cloud layer, with the total starting area of approximately 15%,
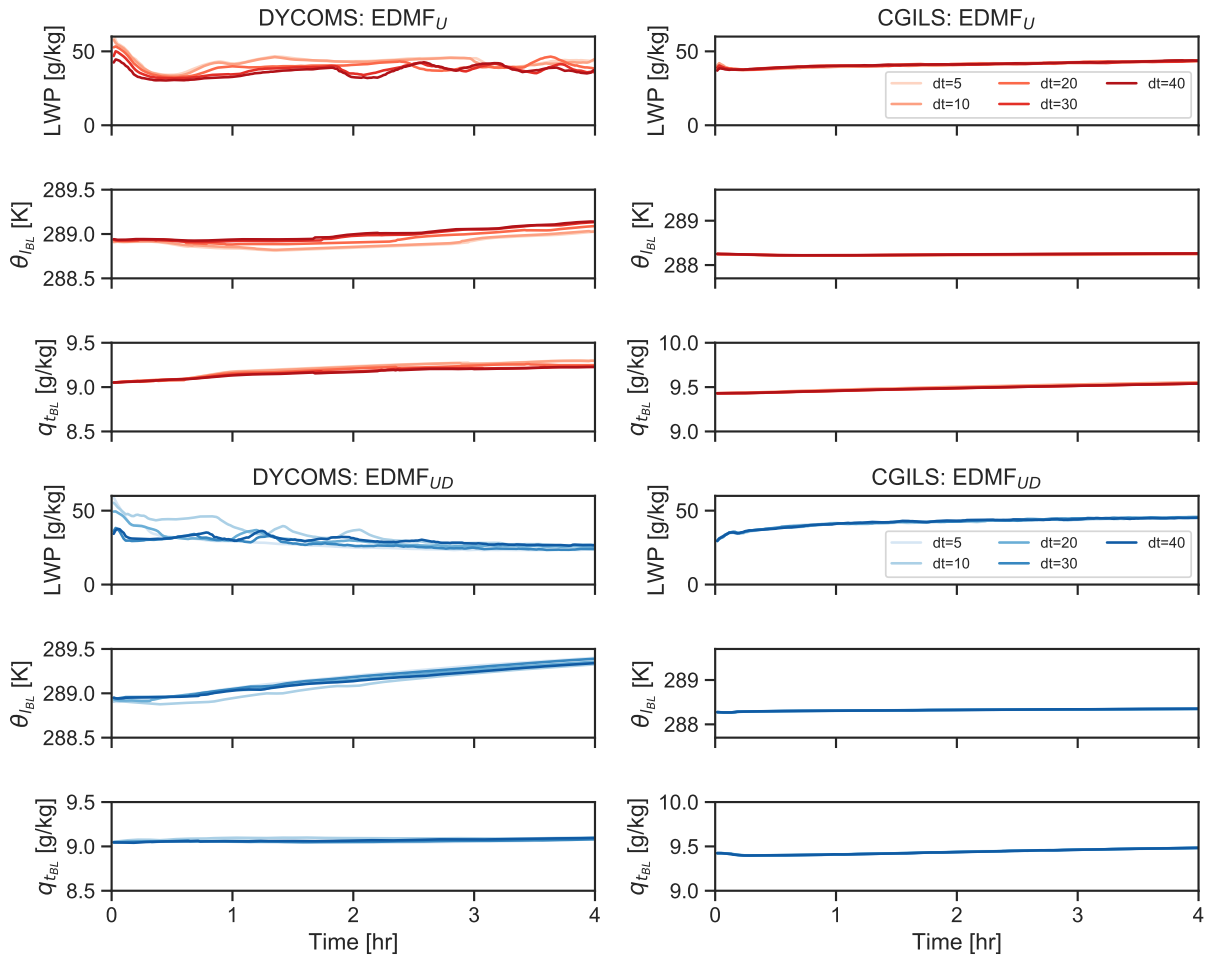
Figure 4.14: Simulation results using different time step in $EDMF_U$ and $EDMF_{UD}$ for both DYCOMS and CGILS.

similarly to updrafts. The strength of the downdraft vertical velocity is formulated as a combined effect of the intensity of the surface-driven updrafts and cloud-top radiative cooling. The starting downdraft thermodynamic properties are proportional to the entrainment flux at the STBL top, which is determined by the jump values of heat or moisture across the inversion.

To evaluate the importance of the updraft and downdraft contributions, we run three different SCM simulations for the tested STBLs: without mass flux (ED), with updrafts only ($EDMF_U$), and with both updrafts and downdrafts ($EDMF_{UD}$). When there is no mass-flux (neither updraft nor downdraft), ED underestimates the cloud-top entrainment flux, yielding

a cold and moist bias that leads to a strong overestimation of LWP. The inclusion of updrafts increases the cloud-top entrainment flux and keeps the mean STBL profiles more well-mixed and reduces the temperature and moisture biases. We find that including downdrafts increases vertical mixing in the upper part of the boundary layer especially for q_t, and it results in a warmer and drier STBL than for EDMF$_U$. Overall, the proposed parameterization reproduces the LES profiles because of the addition of downdraft heat and moisture transport in the WRF SCM. However, we find that differences in EDMF$_U$ and EDMF$_{UD}$ are not significant.

Based on the results from the two STBL cases, we conclude that, for the tested version of the WRF model, it is necessary to include updrafts as part of the non-local mass-flux as ED does not represent correctly the cloud-top entrainment flux. An addition of downdrafts shows some improvements in these two cases. However, further investigations are needed to determine whether downdrafts play a greater role in different meteorological conditions. We hypothesize that ED would have a better match with LES when there is less cloud-top entrainment (e.g., when the PBL is less turbulent), and that the inclusion of downdrafts would be necessary when surface fluxes are small. A recent study by Matheou and Teixeira (2019) compared various LESs of STBL for different physical processes included and concluded that surface fluxes, surface shear, and cloud-top radiative cooling all contribute substantially to the turbulence in STBL. Whether the EDMF parameterization responds similarly in such conditions will be investigated in the future.

4.6 Acknowledgments

and Thijs Heus for constructive comments. We also thank Minghua Ong for proofreading the manuscript. The WRF model is freely available at `https://github.com/wrf-model/WRF`, the modifications made in this paper can be found at `https://github.com/elynnwu/EDMF_JPL`.

Chapter 4, in full with slight modifications, is a reprint of the material as it is expected to appear in "On the Parameterization of Convective Downdrafts to Represent Marine Stratocumulus Clouds" (E. Wu, H. Yang, J. Kleissl, K. Suselj, M. J. Kurowski, and J. Teixeira) in Monthly Weather Review (submitted 09/2019, revised 12/2020). The dissertation author was the primary investigator and author of this paper.

Chapter 5

Sensitivity to the Parameterization of Convective Updrafts and Downdrafts in Marine Stratocumulus Clouds

5.1 Introduction

The formation, maintenance, and dissipation of Stratocumulus (Sc) clouds are controlled by the turbulent transport in the boundary layer. Observational campaigns (e.g. Crosbie et al., 2016, Malinowski et al., 2013, Stevens et al., 2003) and high resolution numerical modeling of Sc clouds (e.g. Blossey et al., 2013, Kurowski et al., 2009, Matheou and Teixeira, 2019, Stevens et al., 2005, Yamaguchi and Randall, 2011) have greatly improved our understanding of the interplay of the physical processes (e.g., cloud-top radiative cooling, entrainment, evaporative cooling, surface fluxes, wind shear) responsible for the turbulent transport. However, accurate modeling of Sc clouds in coarse resolution atmospheric models remains a research challenge as these processes range widely in both spatial and temporal scales (e.g. Ghonima et al., 2017, Lin et al., 2014, Teixeira et al., 2011). For example, the cloud-top entrainment layer often lies

within a few tens of meters, while vertical mixing due to surface-driven convection or cloud-top radiative cooling can reach up to several hundred meters. As a result, parameterization of these physical processes is challenging.

Recent studies showed that cloud-top triggered downdrafts contribute strongly to the total heat and moisture transport in stratocumulus-topped boundary layer (STBL) (Brient et al., 2019, Chinita et al., 2017, Davini et al., 2017). This specific process has recently been implemented in two numerical weather prediction models: GFS (Han and Bretherton, 2019) and WRF (Wu et al., 2020) (Chapter 4). Both studies adopted the eddy-diffusivity/mass-flux (EDMF) framework, decomposing turbulence into local and non-local contributions where downdrafts represent one component of the non-local transport. While both studies showed some improvements in the modeling of Sc clouds when both updrafts and downdrafts are explicitly represented, it remains unclear if the roles of updrafts and downdrafts change under different meteorological conditions. A recent study by Matheou and Teixeira (2019) compared various LES and concluded that multiple physical processes contribute substantially to the turbulence in STBL.

This study builds upon the framework in Chapter 4 which uses Mellor-Yamada-Nakanishi-Niino (MYNN) (Nakanishi and Niino, 2006, 2009) as the ED component for modeling the non-convective environment and stochastic multi-plume as the MF component. We place a special emphasis on evaluating the role of updrafts and downdrafts in turbulent transport under different physical STBL conditions (same experiments in Matheou and Teixeira (2019))– without radiation, without surface fluxes, and without wind shear. A new updraft and downdraft parameterization is designed and implemented in WRF to better represent the non-local transport observed in large eddy simulation (LES).

Section 5.2 documents the LES cases used in this study, updraft and downdraft properties from these cases, and the numerical setup of WRF single column model (SCM). Section 5.3 describes the EDMF and MYNN schemes as well as the updraft and downdraft implementation in WRF. Section 5.4 shows the results for all cases in WRF SCM. Finally, conclusions are presented

in Section 5.5 and direction for future work is outlined in Section 5.6.

5.2 Methodology

5.2.1 Large eddy simulation (LES) model and parametric study

The LES model used in this work is the UCLA-LES (Stevens, 2010). We begin with DYCOMS-II RF01 (Stevens et al., 2005) as the baseline case (DYCOMS) as shown in Chapter 4, Table 1. The simplified model of radiation matching the δ-four stream transfer code (Stevens et al., 2005) is used. The case is run for 4 h beginning at midnight. We limit our analysis of the updraft and downdraft properties to quasi-steady conditions unperturbed by the diurnal cycle. In the base case, the following values are used: divergence of large-scale winds $D = 3.75 \times 10^{-6}$ m s^{-1}, geostrophic wind $u_g = 7$ m s^{-1}, $v_g = -5.5$ m s^{-1}, sensible heat flux $= 15$ W m^{-2}, and latent heat flux $= 115$ Wm^{-2}. We vary the physical processes in DYCOMS one at a time to understand the roles of updrafts and downdrafts under different meteorological conditions. First, radiative forcing is turned off (DYCOMS–noRad) to isolate effects from radiative cooling and explore how radiation impacts updrafts and downdrafts. Second, sensible and latent heat fluxes are changed to zero (DYCOMS–noSfx) to understand the role of the surface in generating updrafts and downdrafts. Additionally, large scale horizontal divergence is also changed to zero in order to avoid a rapid decrease of the boundary layer depth. Lastly, the initial wind profile and the geostrophic wind are set to zero (DYCOMS–noWind) to separate their effects from wind shear. Table 5.1 summarizes the four cases.

5.2.2 Determining plume properties

We determine updraft and downdraft properties following Chapter 4, where updrafts are LES grid-points that conform to the following conditions: $w' > 1$, $q_t' > 0$, and either $\theta_l' < 0$ or

Table 5.1: Summary of the parametric study in large eddy simulation. Sensitivities to physical processes include radiation (noRad), surface fluxes (Sfx), and wind (noWind). True flags denote a parameter that is used as default, and False flags indicate processes that are turned off or set to zero.

Case	D	Wind	Radiation	Surface fluxes
DYCOMS	True	True	True	True
DYCOMS–noRad	True	True	False	True
DYCOMS–noSfx	False	True	True	False
DYCOMS–noWind	True	False	True	True

$\theta'_v > 0$. For downdrafts, the following conditions are used: $w' < 0$, $q'_t < -1$, and $\theta'_l > 0$. In the previous study, no restriction is put on whether a plume is contiguous (i.e., sharing either a face, an edge, or a corner). In this study, to consider only coherent structures, we restrict the plumes to have a minimum contiguous volume. This restriction reduces the heat and moisture transport of updrafts and downdrafts due to the decrease in total plume area. Figure 5.1 shows updraft and downdraft heat and moisture transport under different volume thresholds. The highest volume threshold results in the smallest mass-flux transport. We select a minimum volume of 20,000 grid-points (0.24 km^3) as final criterion and apply this to all other cases.

Results of updraft, downdraft, and environmental contributions to the total heat and moisture transport for all cases are shown in Figure 5.2. For DYCOMS, updraft and downdraft contributions to the total heat and moisture transport are comparable (Figure 5.2A & E). Cloud-top entrainment flux mostly comes from updrafts. The peak in downdraft transport is slightly below updraft. These results are not identical to those in Chapter 4 because an additional volume filter is applied here.

When radiation is turned off, the in-cloud heat transport seen in DYCOMS disappears (Figure 5.2B between 600 and 800 m), indicating that radiative cooling is responsible for this transport. Total moisture transport in the upper half of the PBL is strongly reduced (Figure 5.2F). Radiative cooling is likely the driver of moisture transport from the cloud-top. In-cloud, updraft and downdraft heat flux is comparable in DYCOMS–noRad, suggesting that radiative cooling
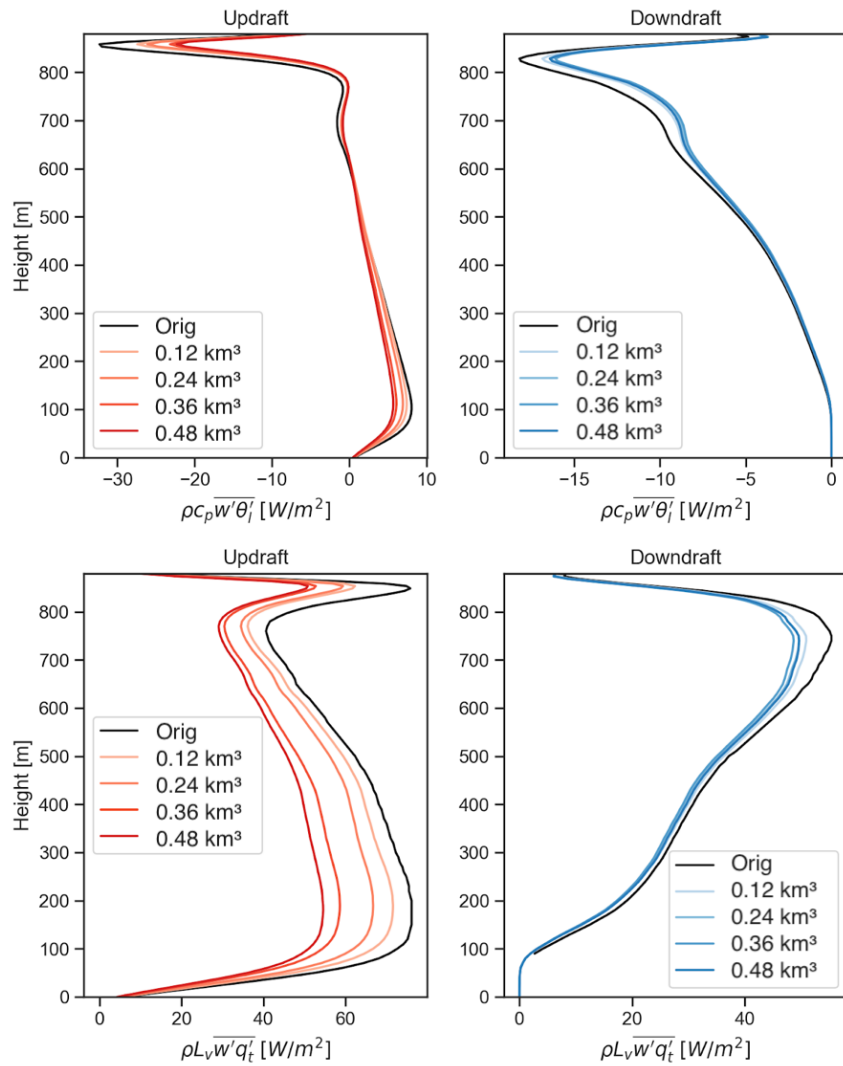
Figure 5.1: DYCOMS turbulent transport of heat and moisture under different updraft and downdraft volume filter: no filter (Orig), 10,000 (0.12 km^3), 20,000 (0.24 km^3), 30,000 (0.36 km^3), 40,000 (0.48 km^3) grid-points.
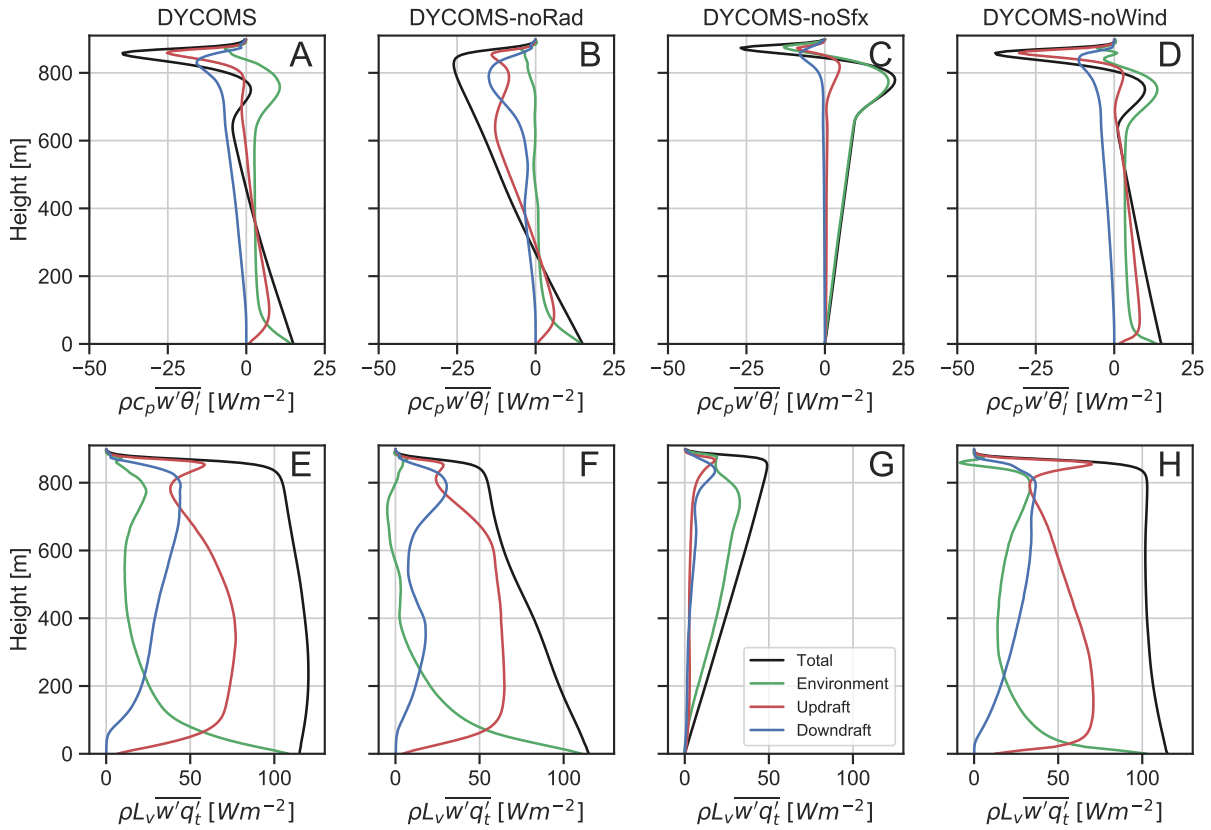
Figure 5.2: Comparison of heat and moisture turbulent transport for DYCOMS (A & E), DYCOMS–noRad (B & F), DYCOMS–noSfx (C & G), DYCOMS–noWind (D & H) from the environment, updrafts, and downdrafts.

is not the only driving force for downdraft heat transport. Similar observations are found in the moisture transport, where downdraft is only comparable to updraft in-cloud and quickly drops off below 600 m.

When surface fluxes (both sensible and latent heat flux) are set to zero, the total heat and moisture transport in the lower half of the PBL increase with height due to the lack of heat and moisture supply from the surface (Figure 5.2C & G). Total cloud-top entrainment heat flux is comparable to that in DYCOMS, while total entrainment moisture flux is much weaker. Updraft and downdraft transport are very weak in most of the PBL, except near cloud-top, and most of the transport is due to the environment. This suggests that while surface fluxes are important in generating updraft and downdraft, other factors are at play near cloud-top.

When the mean wind is removed and the geostrophic wind is set to zero, total updraft heat and moisture transport are similar to the baseline DYCOMS (Figure 5.2D & H). Some differences are found near the surface where moisture transport decreases slightly with height (versus a slight increase in DYCOMS), and near the cloud-top where moisture transport does not decrease in-cloud as is the case in DYCOMS. This suggests that surface wind shear also plays a role in the moisture transport near the surface. We observe that updraft contributions to cloud-top entrainment heat and moisture flux are even stronger when compared to the baseline case. Moreover, in the middle of the PBL, the environmental moisture transport is almost comparable to that from downdrafts (versus much weaker in DYCOMS), suggesting that wind shear plays a role in intensifying downdraft moisture transport.

Updraft and downdraft area, vertical velocity, perturbation from grid-mean liquid water potential temperature, total water mixing ratio, virtual potential temperature, and liquid water mixing ratio are shown in Figure 5.3 for DYCOMS, Figure 5.4 for DYCOMS–noRad, Figure 5.5 for DYCOMS–noSfx, and Figure 5.6 for DYCOMS–noWind. The updraft area is fairly consistent across all cases, while the downdraft area shows two peaks in DYCOMS–noRad (Figure 5.4A) and is significantly smaller in DYCOMS–noSfx (Figure 5.5A). Updraft vertical velocity peaks around 1 m s^{-1} in the middle of the PBL for all cases. Downdraft vertical velocity decreases strongly in DYCOMS–noRad (Figure 5.4B) while staying around -1 ms^{-1} in all other cases. Updraft perturbation of θ_l from the grid-mean ($\overline{\theta_l'}$) is similar in DYCOMS and DYCOMS–noWind, but decreases strongly in DYCOMS–noRad (Figure 5.4C) and stays close to zero in DYCOMS–noSFX (Figure 5.5C). Perturbations in θ_v behave similarly. For downdrafts, $\overline{\theta_l'}$ is similar in DYCOMS and DYCOMS–noWind, but $\overline{\theta_l'}$ increases strongly in DYCOMS–noRad (Figure 5.4C) and stays close to zero in DYCOMS–noSFX (Figure 5.5C). Again, $\overline{\theta_v'}$ behaves similarly, and the minimum $\overline{\theta_v'}$ is found near cloud-top in DYCOMS and DYCOMS–noWind. Updraft perturbations of total moisture from the grid-mean ($\overline{q_t'}$) are strongest in DYCOMS–noRad (Figure 5.4E) and weakest in DYCOMS-noSfx (Figure 5.5E). For downdrafts, $\overline{q_t'}$ is similar in

DYCOMS, DYCOMS-noRad, and DYCOMS-noWind, but much smaller in DYCOMS–noSfx. For q_l, updrafts are found in the thickest part of the cloud across the cases, and downdrafts are co-located with the cloud holes (Figure 5.3F, 5.4F, 5.5F, 5.6F).
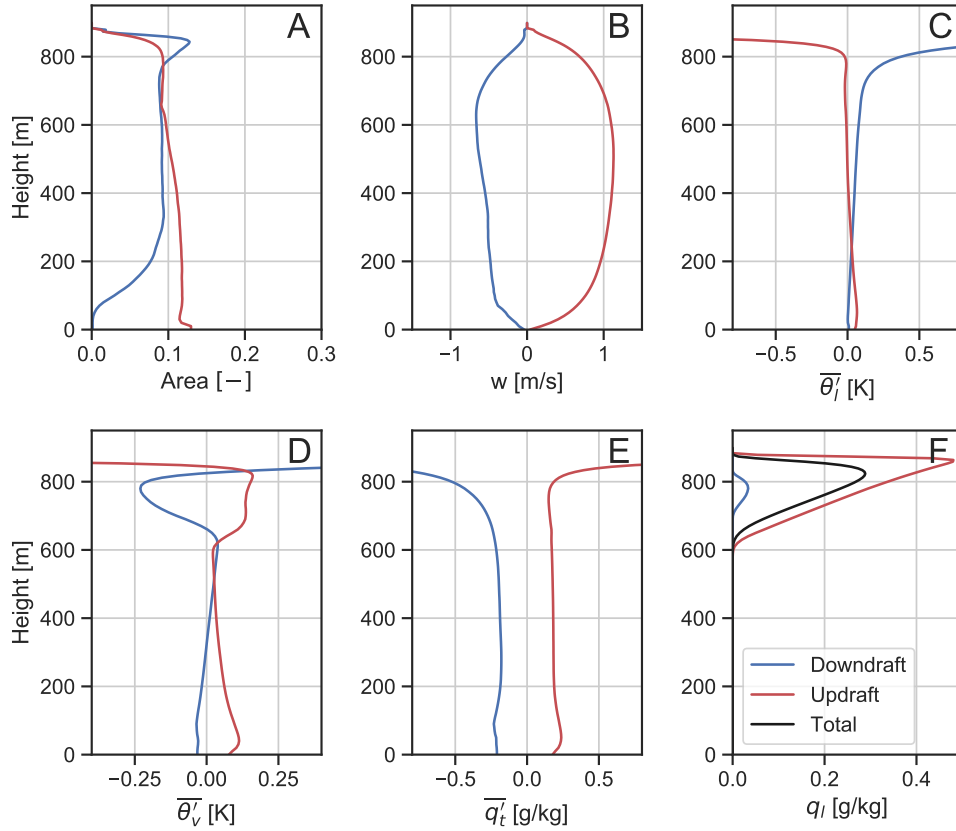
Figure 5.3: DYCOMS: Vertical profiles of updraft and downdraft area (A); vertical velocity (B); grid-mean difference in liquid water potential temperature (C), virtual potential temperature (D), and total water mixing ratio (E); and liquid water mixing ratio (F).

5.2.3   WRF single column model (SCM)

The WRF setup is the same as in Chapter 4, which includes 116 levels in the vertical domain ($\Delta z \approx 20$ m in the first 1 km) and a time step of 40 s. Initial conditions and forcings are identical to that in LES. Fixed surface fluxes are used in all cases. Three PBL configurations are used (identical to that in Chapter 4): 1) the original Mellor-Yamada-Nakanishi-Niino scheme
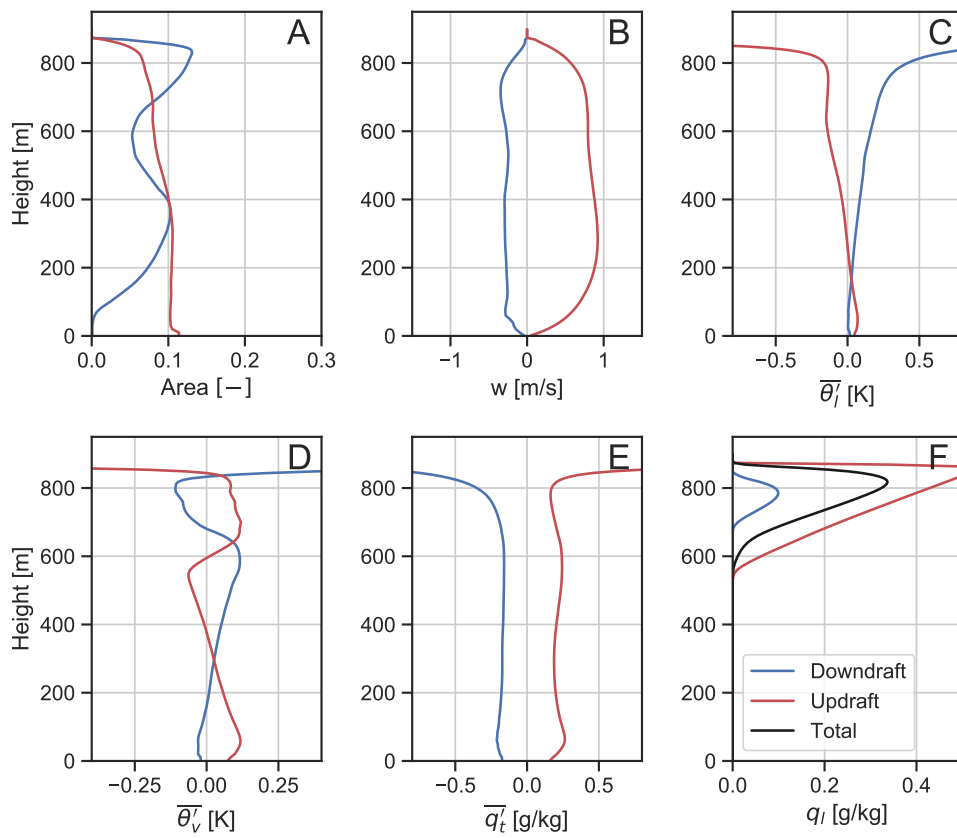
Figure 5.4: Same as Fig. 5.3 for DYCOMS–noRad.
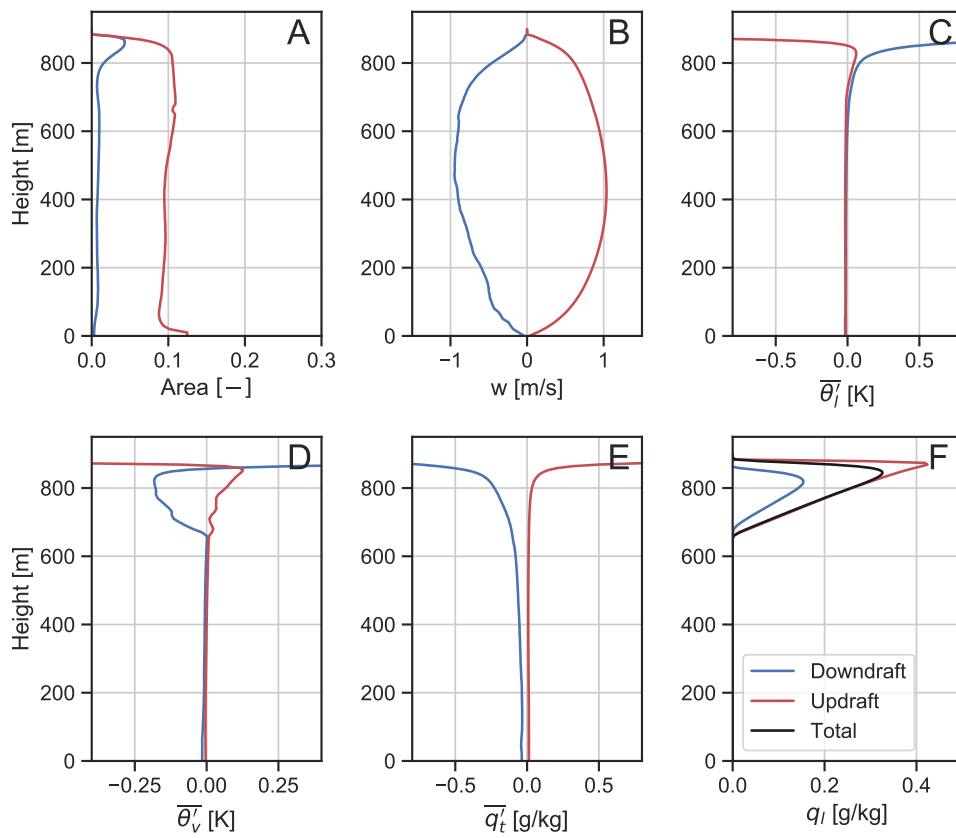
Figure 5.5: Same as Fig. 5.3 for DYCOMS–noSfx.
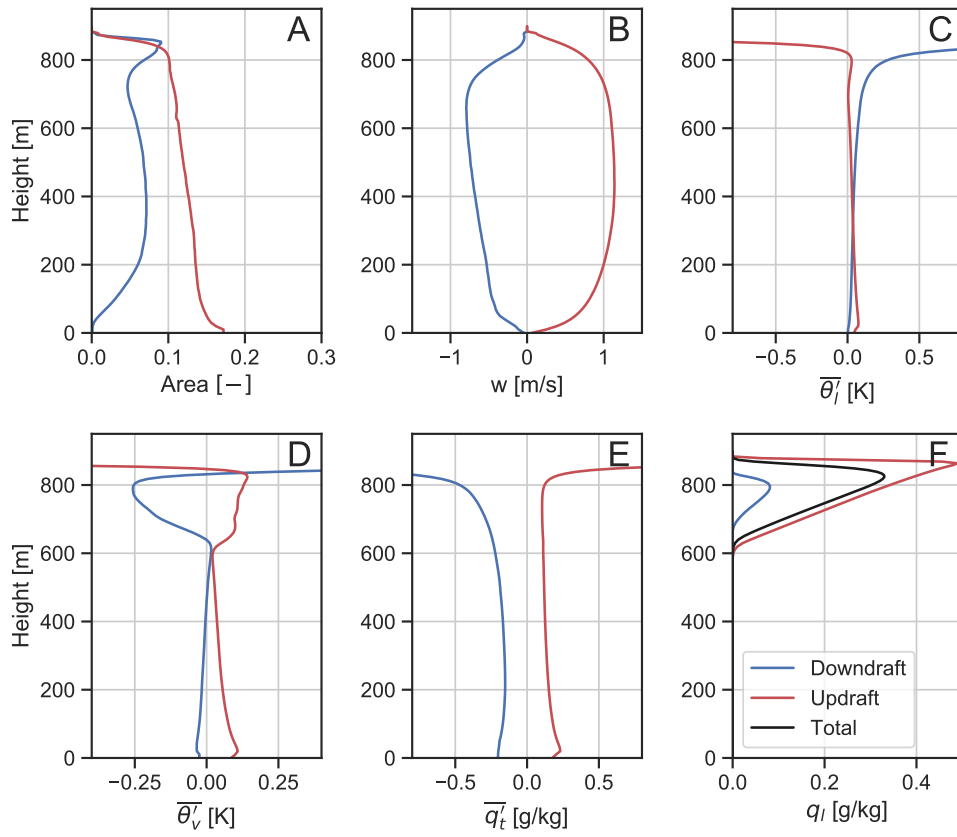
Figure 5.6: Same as Fig. 5.3 for DYCOMS–noWind.

(MYNN; hereinafter ED) (Nakanishi and Niino, 2006, 2009), 2) MYNN with updrafts (EDMF$_U$), and 3) MYNN with updrafts and downdrafts (EDMF$_{UD}$).

5.3 Description of PBL scheme

5.3.1 The Eddy-Diffusivity/Mass-Flux (EDMF) Approach

The EDMF framework for parameterizing turbulence has been used in dry convective boundary layers, shallow convection, deep convection, and recently STBL. The idea behind EDMF is to model the non-convective environment and the convective area separately. Typically, a local ED model is used to model the non-convective environment, while a non-local MF model including updrafts or downdrafts is used to represent the convective area. In the STBL case, Chapter 4 shows that pairing the MYNN local ED model with stochastic multi-plume updrafts and downdrafts captures the turbulent transport well. In this study, we use the same framework and modify how mass-flux is initialized.

5.3.2 Modification to surface-driven updrafts

Previously, surface-driven updrafts were controlled by surface fluxes only. This is a good assumption for surface-driven convection conditions, where other physical processes do not play an important part in turbulence production of the PBL. However, other physical processes do play a role in STBL. Matheou and Teixeira (2019) performed various LES of STBL with various physical conditions and found that surface fluxes, surface shear, and cloud-top radiative cooling all contribute to turbulence production significantly. Moreover, in the LES simulation without surface fluxes shown in Section 5.2.2, updraft vertical velocity was comparable to the reference case (Figure 5.5B), indicating that surface fluxes are not the only driving force for updraft vertical velocity. To account for these processes, we modify the initialization of updrafts so that the

97

strength of updrafts depend not only on surface fluxes but also on surface shear and radiative cooling. This is analogous to how downdrafts are parameterized in Chapter 4 where the initial condition of downdrafts depend on multiple physical processes.

Updraft thermodynamic and dynamic properties follow the same equation as in Chapter 4. The difference here is on how updrafts are initialized. Following Appendix A from Suselj et al. (2019a), surface starting vertical velocity for the i-th plume is formulated as:

$$w_i|_s = \frac{\sigma_w}{\sqrt{2\pi}} \frac{e^{-w_{min,i}^2/(2\sigma_w^2)} - e^{-w_{max,i}^2/(2\sigma_w^2)}}{\overline{a_i}|_s}, \tag{5.1}$$

where s denotes surface, σ_w is the standard deviation of vertical velocity near the surface, w_{min} and w_{max} are the minimum and maximum vertical velocity of all the plumes, and a is the plume area. We assume surface-driven updrafts to be the positive tail of the vertical velocity distribution where $w_{min} = 1\sigma_w$ and $w_{max} = 3\sigma_w$. Equation 5.1 shows that σ_w and a control the strength of the starting updraft vertical velocity. Since we fix w_{min} and w_{max}, the total starting area of updrafts is constant ($\approx 15\%$). This leaves σ_w to be the free parameter and it is parameterized as follows:

$$\sigma_w = 1.34 w_* \left(\frac{z_0}{z_i}\right)^{1/3} \left(1 - 0.8\frac{z_0}{z_i}\right), \tag{5.2}$$

z_i is the PBL height, $w_* = (g/\theta_v)\overline{w'\theta_v'}|_s z_i$ is the convective velocity scale, and $z_0 = 0.1 z_i$. To include effects of surface wind shear and radiative cooling, we propose to replace w_* with a updraft convective velocity scale:

$$w_{*,ud} = \left(c_1 w_*^3 + c_2 u_*^3 + c_3 w_{rad}^3\right)^{1/3}, \tag{5.3}$$

where u_* is the surface friction velocity, $w_{rad} \equiv (g/\theta_v)\overline{w'\theta_v'}|_{rad} z_i$, and c_1, c_2, and c_3 are model constants. w_{rad} is the velocity scale based on the net radiative flux divergence $\left(\overline{w'\theta_v'}|_{rad} = \frac{F_{rad}}{\rho c_p}\right)$. F_{rad} is taken as the radiative flux divergence between cloud-top and cloud base. This formulation

allows the starting updraft vertical velocity to depend on the strength of surface fluxes (w_*), surface shear (u_*), and radiation (w_{rad}). To quantify the relative contributions of the three processes, the values of c_1, c_2, and c_3 are investigated later.

The updraft starting virtual potential temperature for the i-th plume is formulated as:

$$\theta_{v,i}|_s = \overline{\theta_v}|_s + c(w,\theta_v)w_i|_s \frac{\sigma_{\theta_v}}{\sigma_w},\tag{5.4}$$

where $c(w,\theta_v)$ is the correlation coefficient between w and θ_v, and σ_{θ_v} is the standard deviation of θ_v near the surface. As seen in the simulations without surface fluxes, we find that although the updraft θ_v' is small near the surface, it increases in-cloud, causing updrafts to still have a significant contribution to the total heat transport. We therefore also modify how σ_{θ_v} is parameterized so that updrafts are still properly modeled if the surface fluxes are zero. To this end, entrainment from the free troposphere is expected to affect updraft starting temperature as it brings warm and dry air into the PBL. Since including an entrainment term would take the radiative effect into account, we propose to parameterize σ_{θ_v} both in terms of surface fluxes and entrainment:

$$\sigma_{\theta_v} = 1.34\theta_{*,ud}\left(\frac{z_0}{z_i}\right)^{-1/3},\tag{5.5}$$

$$\theta_{*,ud} = c_4 \frac{\overline{w'\theta_v'}|_s}{w_*} + c_5 \frac{\overline{w'\theta_v'}|_{ent}}{w_{rad}},\tag{5.6}$$

where c_4 and c_5 indicate how strong each process contributes to the starting temperature. Note that the original formulation only includes surface effect as the temperature scale is only dependent on surface fluxes ($\theta_* = \frac{\overline{w'\theta_v'}|_s}{w_*}$).

Updraft starting total mixing ratio for the i-th plume is formulated as:

$$q_{t,i}|_s = \overline{q_t}|_s + c(w,q_t)w_i|_s \frac{\sigma_{q_t}}{\sigma_w},\tag{5.7}$$

where $c(w, q_t)$ is the correlation coefficient between w and q_t, and σ_{q_t} is the standard deviation of q_t near the surface. Similar to the modification to σ_{θ_v}, we also formulate the starting total mixing ratio to depend on surface fluxes and entrainment:

$$\sigma_{q_t} = 1.34 q_{t_*} \left(\frac{z_0}{z_i} \right)^{-1/3}, \tag{5.8}$$

$$q_{t_*,ud} = c_6 \frac{\overline{w'q_t'}|_s}{w_*} + c_7 \frac{\overline{w'q_t'}|_{ent}}{w_{rad}}, \tag{5.9}$$

where c_6 and c_7 indicate how strong each process contributes to the starting moisture. Note that the original formulation only includes the surface effect as the moisture scale only depends on surface fluxes ($q_{t,*} = \frac{\overline{w'q_t'}|_s}{w_*}$). The relative importance of each process on the starting temperature and moisture depends on the values of c_4, c_5, c_6, and c_7, which are investigated later.

While traditional parameterizations of updrafts require surface fluxes to be positive, we find significant updraft heat and moisture transport in the upper part of the PBL even when surface fluxes are zero (Figure 5.2C & G). As a result, we modify the updraft criteria to take into account radiative cooling in addition to positive surface fluxes. In the modified criteria, either positive surface fluxes or strong radiative flux divergence between cloud-top and cloud base ($F_{rad} > 10$ Wm^{-2}) can trigger updrafts. Under this modification, whenever surface fluxes are zero, updraft starting θ_v or q_t can still exist due to entrainment heat and moisture flux (Eqs. 5.6 & 5.9).

5.3.3 Modification to cloud-top triggered downdrafts

Downdraft thermodynamic and dynamic properties follow the same equation as in Chapter 4 while their initialization is modified. We retain the parameterized standard deviation of vertical velocity but modify the model coefficients in the velocity scale:

$$w_{*,dd} = \left(c_{1_{dd}} w_*^3 + c_{2_{dd}} u_*^3 + c_{3_{dd}} w_{rad}^3 \right)^{1/3}. \tag{5.10}$$

Note that this formulation is identical to that for updrafts (Equation 5.3). However, we expect the constants ($c_{1_{dd}}$, $c_{2_{dd}}$, $c_{3_{dd}}$) to be different (e.g., surface fluxes are likely to have less influence on downdraft starting w). We also retain the formulation for the standard deviation of θ_v and q_t for downdrafts while modifying the temperature and moisture scale:

$$\theta_{*,dd} = c_{4_{dd}} \frac{\overline{w'\theta_v'}|_s}{w_*} + c_{5_{dd}} \frac{\overline{w'\theta_v'}|_{ent}}{w_{rad}}, \tag{5.11}$$

$$q_{t_{*,dd}} = c_{6_{dd}} \frac{\overline{w'q_t'}|_s}{w_*} + c_{7_{dd}} \frac{\overline{w'q_t'}|_{ent}}{w_{rad}}. \tag{5.12}$$

As is the case for $w_{*_{dd}}$, we expect the constants to be different from updrafts and thus distinguish them with the subscript dd. In summary, the paramterization of standard deviation (σ_w, σ_{θ_v}, σ_{q_t}) for updraft and downdraft is identical except for model constants.

5.3.4 Parameterization constants

Since the model constants in Eqs 5.3, 5.6, 5.9, 5.10, 5.11, 5.12 are used to parameterize the corresponding standard deviation of each variable (e.g., for updrafts, σ_w depends on c_1, c_2, and c_3 in Eqs 5.3), the actual LES standard deviations are used to obtain the optimal model constants. Table 5.2 shows standard deviation of w, θ_v, and q_t for each LES case near the surface and cloud-top. σ_w near the surface is fairly consistent across the cases, with DYCOMS–noWind being the strongest and DYCOMS–noRad being the smallest (27% difference). For σ_w near the cloud-top, a similar trend is found, but the difference is even larger between the two cases (38%). This is also seen in the downdraft vertical velocity in Figure 5.4A since downdraft vertical velocity are strongly correlated with σ_w. In terms of σ_{θ_v}, DYCOMS–noSfx has the smallest value for both surface and cloud-top. However, the difference among the cases is more pronounced for $\sigma_{\theta_{v_{sfc}}}$ than for $\sigma_{\theta_{v_{z_i}}}$. As for σ_{q_t}, we observe that DYCOMS–noSfx again has the smallest value among the cases.

Table 5.2: LES results: standard deviation of w, θ_v, and q_t near the surface ($z/z_i = 0.1$) and the cloud-top ($z/z_i = 0.9$)

Case	$\sigma_{w_{\text{sfc}}}[ms^{-1}]$	$\sigma_{\theta_{v_{\text{sfc}}}}[10^{-2}K]$	$\sigma_{q_{t_{\text{sfc}}}}[g/kg]$	$\sigma_{w_{z_i}}[ms^{-1}]$	$\sigma_{\theta_{v_{z_i}}}[10^{-2}K]$	$\sigma_{q_{t_{z_i}}}[g/kg]$
DYCOMS	0.42	4.41	0.16	0.46	13.44	0.21
DYCOMS–noRad	0.34	4.08	0.16	0.33	18.93	0.17
DYCOMS–noSfx	0.38	1.00	0.02	0.46	7.00	0.06
DYCOMS–noWind	0.47	3.63	0.13	0.53	9.93	0.14

Table 5.3: Optimal SCM model constants as determined from LES.

Case	c_1	c_2	c_3	c_4	c_5	c_6	c_7
Updraft	0.31	0.49	0.25	0.69	0.05	0.89	0.15
Downdraft ($c_{x_{dd}}$)	0.27	0.95	0.41	0.67	0.15	0.31	0.23

To obtain the model constants, a list of values between 0.01 and 1.01 is generated for each constant (c). The final values are selected to minimize the euclidean distance from the standard deviation in LES across the four cases. Table 5.3 shows the model constants that will be used in the SCM. It is important to note that because w_*, u_*, and w_{rad} do not necessarily have the same magnitude (u_* is often smaller), the absolute value of c_1, c_2, and c_3 do not represent how strong each component contributes to the parameterization of σ_w. Instead, comparing c_1 and $c_{1_{dd}}$ reveals how much w_* contributes to updraft and downdraft σ_w. For example, w_* contributes more strongly to updrafts ($c_1 > c_{1_{dd}}$), while u_* and w_{rad} contribute more strongly to downdrafts ($c_{2_{dd}} > c_2$, $c_{3_{dd}} > c_3$). Surface fluxes are equally important in the parameterization of σ_{θ_v} as seen in the similar value in c_4 and $c_{4_{dd}}$, while entrainment heat flux is more important in downdrafts ($c_{5_{dd}} > c_5$). For the parameterization of σ_{q_t}, surface fluxes are more important for updrafts than downdrafts ($c_6 > c_{6_{dd}}$), and entrainment moisture flux is more important in downdraft than updraft ($c_{7_{dd}} > c_7$).

5.4 Results

5.4.1 DYCOMS

We begin the comparison between WRF SCM and LES with the baseline DYCOMS case. Figure 5.7A, E, I show the mean field of θ_l, q_t, and q_l from WRF SCM. Figure 5.8A, E show the total heat and moisture flux, and Figure 5.9A, E, I show time series of liquid water path (LWP), boundary layer averaged heat and moisture. ED shows cold and moist bias when compared to LES, leading to an overestimation of liquid water. This is a result of the lack of entrainment heat and moisture flux in ED. $EDMF_U$ and $EDMF_{UD}$ show very similar results in the mean fields of θ_l, q_t, and q_l, and they are warmer and dryer when compared to ED. While the difference in $EDMF_U$ and $EDMF_{UD}$ is very small, it can be seen that $EDMF_{UD}$ is slightly colder in-cloud. Moreover, the moisture profile of $EDMF_{UD}$ is dryer below-cloud and more moist in-cloud. These slight differences are a result of the different total heat and moisture flux, as seen in Figure 5.8A,E. $EDMF_{UD}$ has a stronger entrainment heat and moisture flux when compared to $EDMF_U$ (Figure 5.8A,E), resulting in a slightly warmer and dryer boundary layer averaged temperature and moisture (Figure 5.9E,I). The lack of entrainment heat and moisture flux in ED leads to strong cold and moist biases, and overestimation of LWP (5.9A). Both $EDMF_U$ and $EDMF_{UD}$ produce similar LWP as LES.

5.4.2 DYCOMS–noRad

For DYCOMS–noRad, Figure 5.7B, F, J shows the mean field of θ_l, q_t, and q_l. Figure 5.8B, F shows the total heat and moisture flux, and Figure 5.9B, F, J shows time series of LWP, boundary layer averaged heat and moisture. In the no radiation case, total entrainment heat and moisture flux are much weaker than the baseline case. Higher entrainment velocities are expected in more turbulent PBLs, and the entrainment velocity parameterization (e.g. Fang et al., 2014, Ghonima et al., 2016) is often formulated as a combination of the buoyancy flux generated by
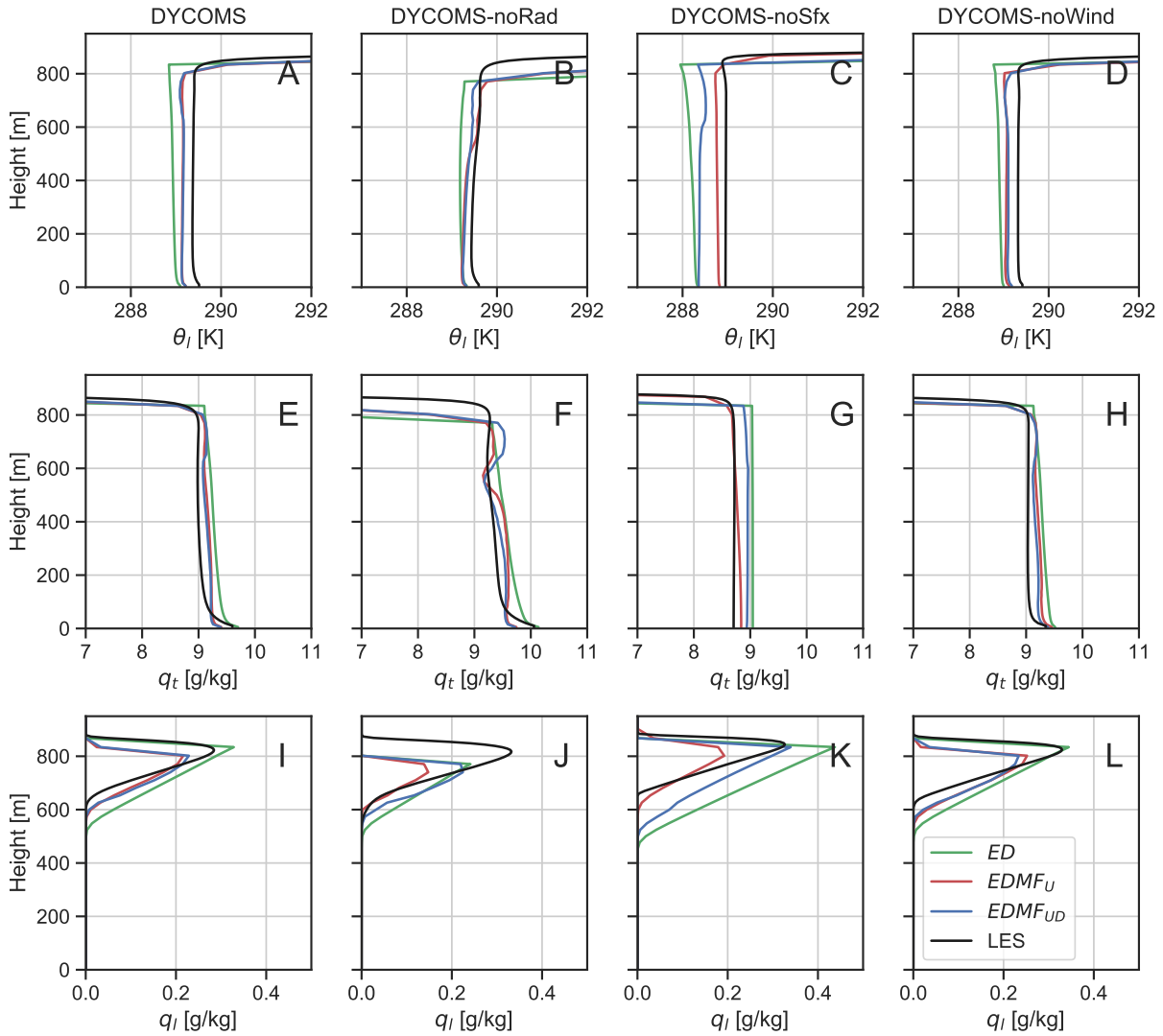
Figure 5.7: WRF SCM results of liquid water potential temperature, total water mixing ratio, and liquid water mixing ratio for DYCOMS (A,E,I), DYCOMS–noRad (B,F,J), DYCOMS–noSfx (C,G,K), and DYCOMS–noWind (D,H,L). Results are averaged over simulation hour 3-4.
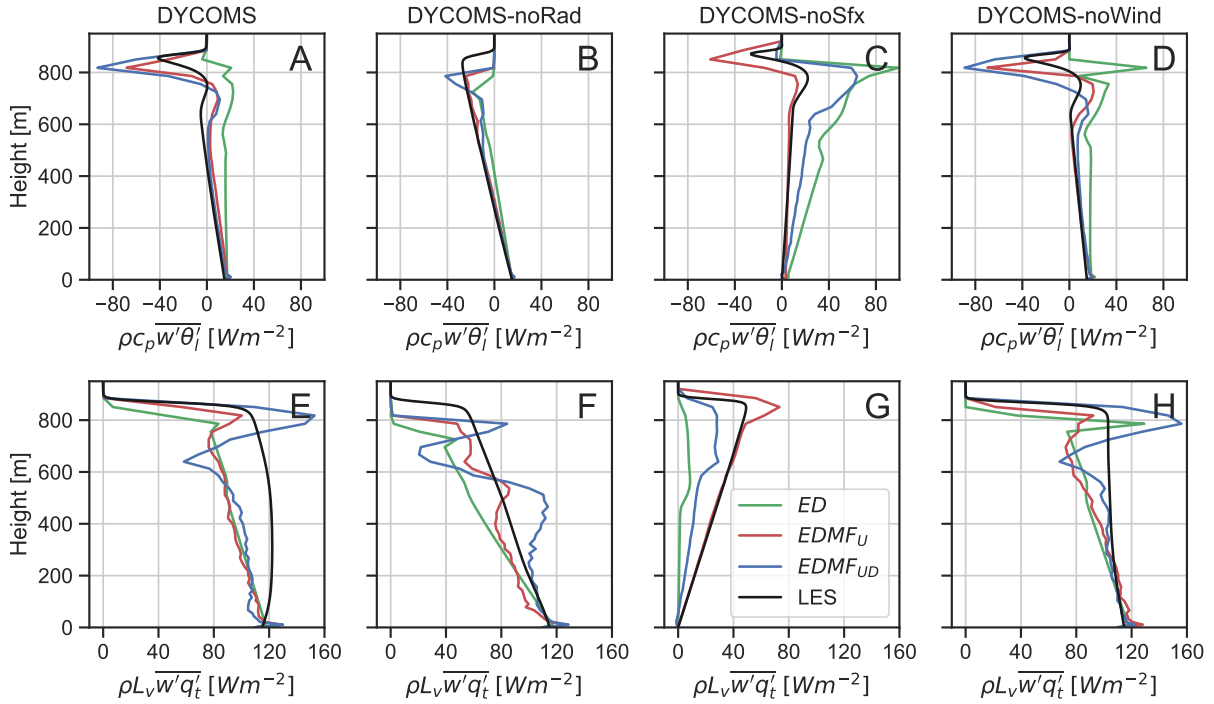
Figure 5.8: WRF SCM results of total heat and moisture flux for DYCOMS (A,E), DYCOMS–noRad (B,F), DYCOMS–noSfx (C,G), and DYCOMS–noWind (D,H). Results are averaged over simulation hour 3-4.

radiative divergence and the buoyancy flux generated at the surface. It is therefore expected that DYCOMS–noRad has weaker entrainment heat and moisture flux.

ED, EDMF$_U$, and EDMF$_{UD}$ all produce a lower PBL height compared to LES. ED simulates the coldest and most moist PBL among the three simulations. Both EDMF$_U$ and EDMF$_{UD}$ produce decoupled θ_l and q_t profiles. While decoupling is also seen in LES, the extent is much weaker. The decoupling of the θ_l and q_t profiles signals the importance of radiative cooling in providing turbulence and mixing θ_l and q_t from cloud-top to the surface. ED does not produce any decoupling, likely because only local mixing is modeled. The difference in *EDMF$_U$* and *EDMF$_{UD}$* is larger than the baseline case. θ_l in *EDMF$_{UD}$* is slightly more well-mixed than *EDMF$_U$* (colder θ_l in-cloud), while q_t is more decoupled (more moist in-cloud and drier in the lower part of the PBL). Since the in-cloud θ_l and q_t are different between *EDMF$_U$* and *EDMF$_{UD}$*, their q_l are different. In terms of total heat flux, EDMF$_U$ produces the closest profile
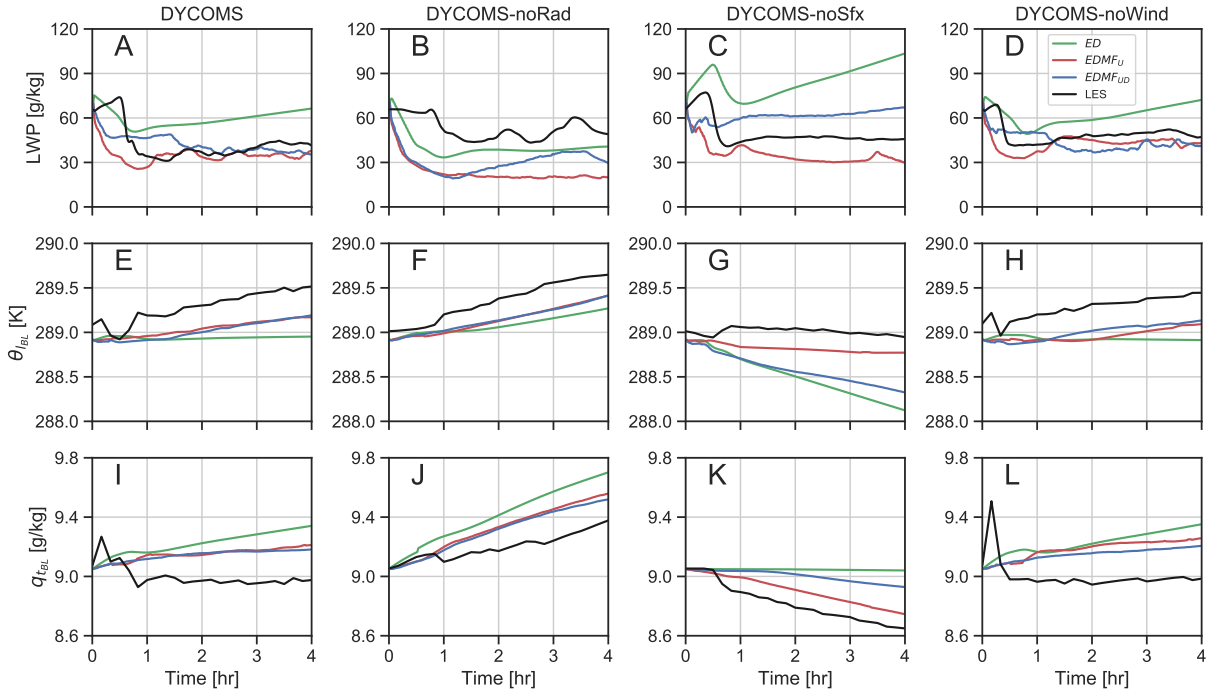
Figure 5.9: WRF SCM time series of liquid water path, boundary layer averaged heat and moisture for DYCOMS (A,E,I), DYCOMS–noRad (B,F,J), DYCOMS–noSfx (C,G,K), and DYCOMS–noWind (D,H,L).

compared to LES. However, all three simulations show reasonable profiles of heat flux (Figure 5.8B). Note that ED is not negatively affected by the lack of entrainment heat flux since the no radiation case has much weaker entrainment. Boundary layer averaged θ_l of all three simulations is similar (Figure 5.9F). For total moisture flux, $EDMF_U$ simulates the best match compared to LES. ED underestimates the moisture flux throughout the whole PBL, while $EDMF_{UD}$ produces two distinct peaks in moisture transport (just below cloud-base and near cloud-top). The strong decoupling of q_t in $EDMF_{UD}$ is likely a result of this. Downdraft moisture transport (not shown) decreases too strongly after initiation, and updraft moisture transport is overestimated in the lower part of the PBL. In contrast, updraft moisture transport matches LES well in $EDMF_U$.

ED and $EDMF_U$ simulate stable LWP during simulation hour 3 to 4 (Figure 5.9B), while $EDMF_{UD}$ changes more during this time likely because its q_t is decoupled. Even though ED simulates the closest match of LWP compared to LES, its boundary layer averaged θ_l and q_t are

most biased. Comparing DYCOMS–noRad to DYCOMS, LES shows more increase in θ_l at the end of the simulation. LES also shows an increase in boundary layer averaged q_t, as opposed to stable q_t in DYCOMS. For WRF SCM, all three simulations show increases in θ_l (ED is constant in DYCOMS). All three simulations show increases in q_t in the PBL, with ED increasing the most among the three (EDMF$_U$ and EDMF$_{UD}$ are constant in DYCOMS). This suggests that the role of radiation in simulating PBL heat and moisture is consistent between LES and WRF PBL paramterization for all three SCM simulations.

5.4.3   DYCOMS–noSfx

For DYCOMS–noSfx, Figure 5.7C, G, K shows the mean field of θ_l, q_t, and q_l. Figure 5.8C, G shows the total heat and moisture flux, and Figure 5.9C, G, K shows time series of LWP, boundary layer averaged heat and moisture. EDMF$_U$ simulates the closest match with LES in the mean field of θ_l and q_t, while ED shows the largest cold and moist bias. Additionally, EDMF$_U$ has the most well-mixed profile of θ_l, while its q_t profile is slightly under-mixed in the lower half of the PBL ($\approx$400 m and below). EDMF$_{UD}$ fails to mix the warm and dry air in the top part of the PBL to the surface, causing slight decoupling of θ_l and q_t. ED also fails to mix the warm air in the upper part of the PBL to the surface, but it is capable of maintaining a well-mixed profile of q_t. EDMF$_U$ simulates the closest q_l profile among the three, with ED and EDMF$_{UD}$ having too low of a cloud-base.

In terms of total heat and moisture flux, EDMF$_U$ again has the closest match among the three. The lack of entrainment heat and moisture flux in ED causes θ_l and q_t to be too cold and too moist. Similar findings are found in EDMF$_{UD}$, though the entrainment moisture flux is better simulated here. In the parameterization, both updrafts and downdrafts initial temperature and moisture depend strongly on surface fluxes (c_4, c_5, $c_{6_{dd}}$, and $c_{6_{dd}}$ in Table 5.3). As a result, updraft and downdraft heat transport are weak near the surface and cloud-top. In the case of EDMF$_U$, we find that while the starting updraft heat transport is very weak near the surface, it

remains slightly positive and is able to reach the top of the PBL. At the top of the PBL, updrafts contribute strongly to the entrainment heat flux as seen in Figure 5.8C. For moisture transport, the updrafts contribution to total moisture transport is also very weak near the surface, but the updrafts eventually reach the top of the PBL and contribute strongly to the entrainment moisture flux. For EDMF$_{UD}$, a different picture emerges. While the downdraft contributions to total heat and moisture transport are very weak near cloud-top, they increase strongly as they descend. Due to the removal of surface fluxes and the reduced entrainment velocity (also depends on surface fluxes), downdraft starting q_t is very close to the grid-mean. This leads to too much condensation in downdrafts, and downdraft θ_l becomes smaller than the grid-mean. This is opposite of downdrafts observed in LES (Figure 5.5C,E,F). Because of the increased transport in downdrafts, updrafts in EDMF$_{UD}$ are not able to reach the top of the PBL. As a result, a very different mean field of heat and moisture are found between EDMF$_{UD}$ and EDMF$_U$. While it is possible to specifically modify the model coefficients for downdrafts in EDMF$_{UD}$ to better match the downdrafts in LES, we retain the same model coefficients for all cases to develop parameterization that can be generalized.

Without surface fluxes, the boundary layer averaged θ_l stays mostly constant and q_t decreases throughout the simulation in LES. In SCM, EDMF$_U$ simulates relatively constant boundary layer averaged θ_l and decreasing q_t in time (Figure 5.7G, K). EDMF$_{UD}$ simulates decreasing of boundary layer averaged θ_l due to insufficient entrainment heat and moisture flux, but it is able to capture the decrease of q_t. ED simulates the strongest decrease in boundary layer averaged θ_l, while q_t stays relatively constant. This suggests that the role of surface fluxes in simulating PBL heat and moisture is consistent between LES and EDMF$_U$. For ED and EDMF$_{UD}$, simulation results against the baseline case show that they are trending in the right direction but fail to maintain constant θ_l when surface fluxes are removed. ED simulates constant q_t, but fails to simulate the decreasing q_t. Both ED and EDMF$_{UD}$ overestimate LWP (Figure 5.7C), with ED being the more severe of the two. In contrast, EDMF$_U$ slightly underestimates but has a relatively

stable LWP.

5.4.4 DYCOMS–noWind

For DYCOMS–noWind, Figure 5.7D, H, L show the mean field of θ_l, q_t, and q_l. Figure 5.8D, H show the total heat and moisture flux, and Figure 5.9D, H, L show time series of LWP, boundary layer averaged heat and moisture. We find the DYCOMS–noWind is similar to the baseline DYCOMS case in terms of boundary layer heat and moisture. ED shows cold and moist biases, and both EDMF$_U$ and EDMF$_{UD}$ are warmer and drier. Entrainment heat flux in ED are too small (Figure 5.8D), while the entrainment moisture flux is more accurate (Figure 5.8H). The difference between EDMF$_U$ and EDMF$_{UD}$ in terms of θ_l, q_t, and q_l is small. EDMF$_{UD}$ has a slightly smaller q_t in the lower half of the PBL, resulting in a slightly more well-mixed profile. EDMF$_{UD}$ has a stronger entrainment heat and moisture flux than EDMF$_U$. The total heat flux in-cloud is slightly positive, as opposed to near zero/slight negative in the baseline DYCOMS. The total moisture flux is slightly smaller in the middle of the PBL compared to the baseline DYCOMS. As a result, there is a closer match with LES in the total moisture flux for all three simulations. The role of wind shear in STBL appears to be more important in the total heat and moisture transport in the middle of the PBL. One hypothesis is that the change in wind shear organizes updrafts and downdrafts differently, causing the heat and moisture transport to be different as they ascend and descend in the PBL. Though the organization is different because of shear (e.g., roll, cellular), we find that it does not affect the overall simulation of STBL, i.e., the mean profile of θ_l and q_t are similar with or without wind. Both EDMF$_U$ and EDMF$_{UD}$ simulate similar LWP as LES, while ED overestimates LWP. Both EDMF$_U$ and EDMF$_{UD}$ show an increase in boundary layer averaged θ_l (Figure 5.7H), which is consistent with LES. In contrary, ED shows a constant θ_l. In terms of boundary layer moisture, LES shows constant q_t throughout the simulation. However, EDMF$_U$ and EDMF$_{UD}$ show a slight increase in q_t, whereas ED shows a stronger increase (Figure 5.7L). It appears that the role of wind in simulating PBL heat and

moisture is minor, as the difference between DYCOMS and DYCOMS–noWind is small. In terms of WRF SCM PBL parameterization, all three simulations show very similar results as they do in DYCOMS.

5.5   Summary and conclusions

In this study, the parameterization of convective updrafts and downdrafts is investigated in STBL under changing physical conditions. This work is an extension of Chapter 4, and the same modeling framework is adopted. Specifically, we place an emphasis on how the parameterization of updrafts and downdrafts responds to the same changing environment in LES. The EDMF framework used in this work is modified to have different updraft and downdraft initialization. The local transport in the boundary layer is unchanged from previous work and is represented by the MYNN scheme. This modified mass-flux model is implemented and tested in the WRF SCM.

LES modeling of four STBL cases is performed– baseline DYCOMS, without radiation (DYCOMS–noRad), without surface fluxes (DYCOMS–noSfx), and without mean wind and geostrophic wind (DYCOMS–noWind). We find that in LES, updraft and downdraft heat and moisture transport are important in all four cases, though the height where these transports dominate changes. To account for the roles that updrafts and downdrafts play under changing physical environment in LES, the parameterization in SCM is modified. In the new parameterization, we initialize updraft and downdraft starting vertical velocity to depend on surface fluxes, surface wind shear, and radiative cooling. Initial updraft and downdraft temperature and moisture depend on surface fluxes and entrainment heat and moisture flux. The initiation of updrafts is modified to account for not only positive surface fluxes but also radiative flux divergence between cloud-top and cloud base.

Three SCM simulations are tested: without mass flux (ED), with updrafts only (EDMF$_U$), and with updrafts and downdrafts (EDMF$_{UD}$). Results suggest that EDMF$_U$ is capable of simu-

lating all four cases well, even in the case of no surface fluxes. $EDMF_{UD}$ is not able to simulate DYCOMS–noSfx well, as the inclusion of downdrafts prevents updrafts from reaching the top of the PBL. $EDMF_{UD}$ simulates the other three cases well. As for ED, a strong overestimation of LWP is observed in all cases but DYCOMS–noRad, where entrainment heat and moisture flux are much weaker. We find that $EDMF_U$ responds similarly to LES under the same changing physical environment. $EDMF_{UD}$ fails to maintain constant θ_l throughout the simulation when surface fluxes are removed but otherwise simulates the PBL heat and moisture similarly as LES. For ED, it fails to simulate the increase in θ_l in DYCOMS and DYCOMS–noWind. It also fails to maintain the constant q_t in DYCOMS and DYCOMS–noWind, and the decrease in q_t in DYCOMS–noSfx.

Overall, $EDMF_U$ represents STBLs better than ED and $EDMF_{UD}$. This suggests that updrafts are necessary even when surface fluxes are removed. Additionally, the inclusion of downdrafts do not generally lead to improvements in STBL simulation. When $EDMF_{UD}$ models the STBL well, the difference between $EDMF_{UD}$ and $EDMF_U$ is small. If updrafts are modeled properly (i.e., considering radiative flux divergence as additional trigger criterion, formulate starting updraft temperature and moisture with surface fluxes, surface shear, and radiative flux), it is capable of simulating all four STBL cases documented in this study, which covers a wide range of meteorological conditions.

5.6   Direction for future work

Chapter 4 and 5 document the formulation of non-local turbulent transport in well-mixed STBLs. The non-local turbulent transport is parameterized in the form of rising updrafts and descending downdrafts. While explicitly parameterizing downdrafts is more consistent with LES representation of turbulence in the PBL, we find limited improvements in SCM under a wide range of physical conditions. Although one might expect $EDMF_U$ to struggle when surface fluxes are removed, it in fact outperforms $EDMF_{UD}$. In this work, the focus has been on well-mixed

STBLs. Further investigation should include decoupled STBLs (e.g., CGILS S11), where two circulations are expected. Surface driven updrafts are likely limited to the lower half of the PBL, and cloud-top triggered downdrafts likely cannot descend below the top half of the PBL. The roles of updrafts and downdrafts play in the turbulent transport in decoupled STBLs and whether SCM can simulate them correctly should be studied. Additionally, a case in Arctic Stratocumulus should be explored. In Arctic Stratocumulus, surface effects are cutoff from the cloud layer, and surface driven updrafts are unlikely to reach the cloud. Whether SCM can simulate Arctic Stratocumulus with downdrafts and/or updrafts should be studied. Last but not least, real 3D simulation of Stratocumulus clouds should be investigated, and the skill of $EDMF_U$ and/or $EDMF_{UD}$ should be quantified.

5.7 Acknowledgments

Bibliography

Akyurek, B. O. and Kleissl, J. (2017). Closed-Form Analytic Solution of Cloud Dissipation for a Mixed-Layer Model. Journal of the Atmospheric Sciences, 74(8):2525–2556.

Alessandrini, S., Delle Monache, L., Sperati, S., and Cervone, G. (2015). An analog ensemble for short-term probabilistic solar power forecast. Applied Energy, 157:95–110.

Angevine, W. M., Jiang, H., and Mauritsen, T. (2010). Performance of an Eddy DiffusivityMass Flux Scheme for Shallow Cumulus Boundary Layers. Monthly Weather Review, 138(7):2895–2912.

Angevine, W. M., Olson, J., Kenyon, J., Gustafson, W. I., Endo, S., Suselj, K., and Turner, D. D. (2018). Shallow Cumulus in WRF Parameterizations Evaluated against LASSO Large-Eddy Simulations. Monthly Weather Review, 146(12):4303–4322.

Arbizu-Barrena, C., Ruiz-Arias, J. A., Rodrguez-Bentez, F. J., Pozo-Vzquez, D., and Tovar-Pescador, J. (2017). Short-term solar radiation forecasting by advecting and diffusing MSG cloud index. Solar Energy, 155:1092–1103. Publisher: Elsevier Ltd.

Beer, C. G. P. and Leopold, L. B. (1947). Meteorological factors influencing air pollution in the Los Angeles area. Transactions, American Geophysical Union, 28(2):173.

Benjamin, S. G., Weygandt, S. S., Brown, J. M., Hu, M., Alexander, C. R., Smirnova, T. G., Olson, J. B., James, E. P., Dowell, D. C., Grell, G. A., Lin, H., Peckham, S. E., Smith, T. L., Moninger, W. R., Kenyon, J. S., and Manikin, G. S. (2016). A North American Hourly Assimilation and Model Forecast Cycle: The Rapid Refresh. Monthly Weather Review, 144(4):1669–1694.

Blossey, P. N., Bretherton, C. S., Zhang, M., Cheng, A., Endo, S., Heus, T., Liu, Y., Lock, A. P., Roode, S. R. d., and Xu, K.-M. (2013). Marine low cloud sensitivity to an idealized climate change: The CGILS LES intercomparison. Journal of Advances in Modeling Earth Systems, 5(2):234–258.

Bony, S. and Dufresne, J.-L. (2005). Marine boundary layer clouds at the heart of tropical cloud feedback uncertainties in climate models. Geophysical Research Letters, 32(20).

Brient, F., Couvreux, F., Villefranque, N., Rio, C., and Honnert, R. (2019). Object-Oriented Identification of Coherent Structures in Large Eddy Simulations: Importance of Downdrafts in Stratocumulus. Geophysical Research Letters, 46(5):2854–2864.

Chauvin, R., Nou, J., Thil, S., and Grieu, S. (2016). Cloud motion estimation using a sky imager. AIP Conference Proceedings, 1734(1):150003.

Chinita, M. J., Matheou, G., and Teixeira, J. (2017). A Joint Probability DensityBased Decomposition of Turbulence in the Atmospheric Boundary Layer. Monthly Weather Review, 146(2):503–523.

Chow, C. W., Urquhart, B., Lave, M., Dominguez, A., Kleissl, J., Shields, J., and Washom, B. (2011). Intra-hour forecasting with a total sky imager at the UC San Diego solar energy testbed. Solar Energy, 85(11):2881–2893.

Chung, D., Matheou, G., and Teixeira, J. (2012). Steady-State Large-Eddy Simulations to Study the Stratocumulus to Shallow Cumulus Cloud Transition. Journal of the Atmospheric Sciences, 69(11):3264–3276.

Clemesha, R. E. S., Gershunov, A., Iacobellis, S. F., Williams, A. P., and Cayan, D. R. (2016). The northward March of summer low cloudiness along the California coast. Geophysical Research Letters, 43(3):1287–1295.

Coimbra, C. F., Kleissl, J., and Marquez, R. (2013). Overview of Solar-Forecasting Methods and a Metric for Accuracy Evaluation. In Kleissl, J., editor, Solar Energy Forecasting and Resource Assessment, pages 171–194.

Crosbie, E., Wang, Z., Sorooshian, A., Chuang, P. Y., Craven, J. S., Coggon, M. M., Brunke, M., Zeng, X., Jonsson, H., Woods, R. K., Flagan, R. C., and Seinfeld, J. H. (2016). Stratocumulus Cloud Clearings and Notable Thermodynamic and Aerosol Contrasts across the ClearCloudy Interface. Journal of the Atmospheric Sciences, 73(3):1083–1099.

Davini, P., DAndrea, F., Park, S.-B., and Gentine, P. (2017). Coherent Structures in Large-Eddy Simulations of a Nonprecipitating Stratocumulus-Topped Boundary Layer. Journal of the Atmospheric Sciences, 74(12):4117–4137.

de Lozar, A. and Mellado, J. P. (2015). Mixing Driven by Radiative and Evaporative Cooling at the Stratocumulus Top. Journal of the Atmospheric Sciences, 72(12):4681–4700.

de Roode, S. R., Siebesma, A. P., Jonker, H. J. J., and de Voogd, Y. (2012). Parameterization of the Vertical Velocity Equation for Shallow Cumulus Clouds. Monthly Weather Review, 140(8):2424–2436.

Delle Monache, L., Nipen, T., Liu, Y., Roux, G., and Stull, R. (2011). Kalman Filter and Analog Schemes to Postprocess Numerical Weather Predictions. Monthly Weather Review, 139(11):3554–3570.

Denholm, P., Clark, K., and OConnell, M. (2016). On the Path to SunShot: Emerging Issues and Challenges in Integrating High Levels of Solar into the Electrical Generation and Transmission System. page 68.

Dev, S., Savoy, F. M., Lee, Y. H., and Winkler, S. (2017). Short-term prediction of localized cloud motion using ground-based sky imagers. In IEEE Region 10 Annual International Conference, Proceedings/TENCON, pages 2563–2566. ISSN: 21593450.

Engstrm, A., Bender, F. A.-M., and Karlsson, J. (2014). Improved Representation of Marine Stratocumulus Cloud Shortwave Radiative Properties in the CMIP5 Climate Models. Journal of Climate, 27(16):6175–6188.

Fang, M., Albrecht, B. A., Ghate, V. P., and Kollias, P. (2014). Turbulence in Continental Stratocumulus, Part I: External Forcings and Turbulence Structures. Boundary-Layer Meteorology, 150(3):341–360.

Gala, Y., Fernndez, ., Daz, J., and Dorronsoro, J. R. (2016). Hybrid machine learning forecasting of solar radiation values. Neurocomputing, 176:48–59.

GEBCO (2017). General Bathymetric Chart of the Oceans.

Gensler, A., Henze, J., Sick, B., and Raabe, N. (2016). Deep Learning for solar power forecasting An approach using AutoEncoder and LSTM Neural Networks. In 2016 IEEE International Conference on Systems, Man, and Cybernetics (SMC), pages 002858–002865.

Gerber, H., Frick, G., Malinowski, S. P., Brenguier, J.-L., and Burnet, F. (2005). Holes and Entrainment in Stratocumulus. Journal of the Atmospheric Sciences, 62(2):443–459.

Ghate, V. P., Miller, M. A., Albrecht, B. A., and Fairall, C. W. (2014). Thermodynamic and Radiative Structure of Stratocumulus-Topped Boundary Layers. Journal of the Atmospheric Sciences, 72(1):430–451.

Ghonima, M. S., Heus, T., Norris, J. R., and Kleissl, J. (2016). Factors Controlling Stratocumulus Cloud Lifetime over Coastal Land. Journal of the Atmospheric Sciences, 73(8):2961–2983.

Ghonima, M. S., Yang, H., Kim, C. K., Heus, T., and Kleissl, J. (2017). Evaluation of WRF SCM Simulations of Stratocumulus-Topped Marine and Coastal Boundary Layers and Improvements to Turbulence and Entrainment Parameterizations. Journal of Advances in Modeling Earth Systems, 9(7):2635–2653.

Hahn, C. and Warren, S. (2007). A Gridded Climatology of Clouds over Land (1971-96) and Ocean (1954-97) from Surface Observations Worldwide. Technical report, Oak Ridge National Laboratory. type: dataset.

Han, J. and Bretherton, C. S. (2019). TKE-Based Moist Eddy-Diffusivity Mass-Flux (EDMF) Parameterization for Vertical Turbulent Mixing. Weather and Forecasting, 34(4):869–886.

Hartmann, D. L., Ockert-Bell, M. E., and Michelsen, M. L. (1992). The Effect of Cloud Type on Earth's Energy Balance: Global Analysis. Journal of Climate, 5(11):1281–1304.

Haupt, S. E. and Kosovic, B. (2015). Big Data and Machine Learning for Applied Weather Forecasts: Forecasting Solar Power for Utility Operations. In 2015 IEEE Symposium Series on Computational Intelligence, pages 496–501.

Hong, S.-Y., Noh, Y., and Dudhia, J. (2006). A New Vertical Diffusion Package with an Explicit Treatment of Entrainment Processes. Monthly Weather Review, 134(9):2318–2341. ISBN: 0027-0644.

Huang, H., Xu, J., Peng, Z., Yoo, S., Yu, D., Huang, D., and Qin, H. (2013a). Cloud motion estimation for short term solar irradiation prediction. 2013 IEEE International Conference on Smart Grid Communications, SmartGridComm 2013, (Section IV):696–701. ISBN: 9781479915262.

Huang, H.-Y., Hall, A., and Teixeira, J. (2013b). Evaluation of the WRF PBL Parameterizations for Marine Boundary Layer Clouds: Cumulus and Stratocumulus. Monthly Weather Review, 141(7):2265–2271.

Iacobellis, S. F. and Cayan, D. R. (2013). The variability of California summertime marine stratus: Impacts on surface air temperatures. Journal of Geophysical Research: Atmospheres, 118(16):9105–9122.

Iacono, M. J., Delamere, J. S., Mlawer, E. J., Shephard, M. W., Clough, S. A., and Collins, W. D. (2008). Radiative forcing by long-lived greenhouse gases: Calculations with the AER radiative transfer models. Journal of Geophysical Research: Atmospheres, 113(D13).

Jamaly, M. and Kleissl, J. (2012). Validation of SolarAnywhere Enhanced Resolution Irradiation in California. Internal Report, page 12.

Jimenez, P. A., Hacker, J. P., Dudhia, J., Haupt, S. E., Ruiz-Arias, J. A., Gueymard, C. A., Thompson, G., Eidhammer, T., and Deng, A. (2016). WRF-SOLAR: Description and clear-sky assessment of an augmented NWP model for solar power prediction. Bulletin of the American Meteorological Society, 97(7):1249–1264.

Johnstone, J. A. and Dawson, T. E. (2010). Climatic context and ecological implications of summer fog decline in the coast redwood region. Proceedings of the National Academy of Sciences of the United States of America, 107(10):4533–8. Publisher: National Academy of Sciences.

Kankiewicz, A., Dise, J., Wu, E., and Perez, R. (2014). Solar 2014: Reducing Solar Project Uncertainty With an Optimized Resource Assessment Tuning Methodology. 2014 American Solar Energy Society Annual Conference, pages 1–6. ISBN: 9781510801790.

Klein, S. A. and Hartmann, D. L. (1993). The seasonal cycle of low stratiform clouds. Journal of Climate, 6(8):1587–1606. ISBN: 0894-8755.

Kohler, C., Steiner, A., Saint-Drenan, Y.-M., Ernst, D., Bergmann-Dick, A., Zirkelbach, M., Ben Bouallgue, Z., Metzinger, I., and Ritter, B. (2017). Critical weather situations for renewable energies Part B: Low stratus risk for solar power. Renewable Energy, 101:794–803.

Kohler, M. (2006). An integral approach to modeling PBL transports and clouds: EDMF@ECMWF. *Proceedings of workshop on parametrization of clouds in large-scale models*, pages 13–15.

Kurowski, M. J., Malinowski, S. P., and Grabowski, W. W. (2009). A numerical investigation of entrainment and transport within a stratocumulus-topped boundary layer. *Quarterly Journal of the Royal Meteorological Society*, 135(638):77–92.

KuwanoYoshida, A., Enomoto, T., and Ohfuchi, W. (2010). An improved PDF cloud scheme for climate simulations. *Quarterly Journal of the Royal Meteorological Society*, 136(651):1583–1597.

Lara-Fanego, V., Ruiz-Arias, J., Pozo-Vzquez, D., Santos-Alamillos, F., and Tovar-Pescador, J. (2012). Evaluation of the WRF model solar irradiance forecasts in Andalusia (southern Spain). *Solar Energy*, 86(8):2200–2217.

Lee, J. A., Haupt, S. E., Jimnez, P. A., Rogers, M. A., Miller, S. D., and McCandless, T. C. (2017). Solar irradiance nowcasting case studies near sacramento. *Journal of Applied Meteorology and Climatology*, 56(1):85–108.

Lilly, D. K. (1968). Models of cloud-topped mixed layers under a strong inversion. *Quarterly Journal of the Royal Meteorological Society*, 94(401):292–309.

Lin, J.-L., Qian, T., and Shinoda, T. (2014). Stratocumulus Clouds in Southeastern Pacific Simulated by Eight CMIP5CFMIP Global Climate Models. *Journal of Climate*, 27(8):3000–3022.

Lock, A. P. and Macvean, M. K. (1999). The parametrization of entrainment driven by surface heating and cloud-top cooling. *Quarterly Journal of the Royal Meteorological Society*, 125(553):271–299.

Malinowski, S. P., Gerber, H., Jen-La Plante, I., Kopec, M. K., Kumala, W., Nurowska, K., Chuang, P. Y., Khelif, D., and Haman, K. E. (2013). Physics of Stratocumulus Top (POST): Turbulent mixing across capping inversion. *Atmospheric Chemistry and Physics*, 13(24):12171–12186.

Matheou, G. and Teixeira, J. (2019). Sensitivity to Physical and Numerical Aspects of Large-Eddy Simulation of Stratocumulus. *Monthly Weather Review*, 147(7):2621–2639.

Mathiesen, P., Collier, C., and Kleissl, J. (2013). A high-resolution, cloud-assimilating numerical weather prediction model for solar irradiance forecasting. *Solar Energy*, 92:47–61.

Mathiesen, P. and Kleissl, J. (2011). Evaluation of numerical weather prediction for intra-day solar forecasting in the continental United States. *Solar Energy*, 85(5):967–977.

Mellado, J. P. (2017). Cloud-Top Entrainment in Stratocumulus Clouds. *Annual Review of Fluid Mechanics*, 49(1):145–169.

Mellado, J. P., Bretherton, C. S., Stevens, B., and Wyant, M. C. (2018). DNS and LES for Simulating Stratocumulus: Better Together. Journal of Advances in Modeling Earth Systems, 10(7):1421–1438.

Mellado, J. P., Stevens, B., and Schmidt, H. (2014). Wind Shear and Buoyancy Reversal at the Top of Stratocumulus. Journal of the Atmospheric Sciences, 71(3):1040–1057.

Mellor, G. L. and Yamada, T. (1982). Development of a turbulence closure model for geophysical fluid problems. Reviews of Geophysics, 20(4):851–875.

Miller, S. D., Rogers, M. A., Haynes, J. M., Sengupta, M., and Heidinger, A. K. (2017). Short-term solar irradiance forecasting via satellite/model coupling. Solar Energy, (November):0–1. Publisher: Elsevier.

Nakanishi, M. and Niino, H. (2006). An Improved MellorYamada Level-3 Model: Its Numerical Stability and Application to a Regional Prediction of Advection Fog. Boundary-Layer Meteorology, 119(2):397–407.

Nakanishi, M. and Niino, H. (2009). Development of an Improved Turbulence Closure Model for the Atmospheric Boundary Layer. Journal of the Meteorological Society of Japan, 87(5):895–912.

Neggers, R. A. J. (2009). A Dual Mass Flux Framework for Boundary Layer Convection. Part II: Clouds. Journal of the Atmospheric Sciences, 66(6):1489–1506.

Neggers, R. A. J., Kohler, M., and Beljaars, A. C. M. (2009). A Dual Mass Flux Framework for Boundary Layer Convection. Part I: Transport. Journal of the Atmospheric Sciences, 66(6):1465–1487.

NESDIS (2017). GOES Imager Calibration.

Olson, J. B., Kenyon, J. S., Angevine, W. A., Brown, J. M., Pagowski, M., and Suelj, K. (2019). A Description of the MYNN-EDMF Scheme and the Coupling to Other Components in WRFARW.

Pedersen, J. G., Malinowski, S. P., and Grabowski, W. W. (2016). Resolution and domain-size sensitivity in implicit large-eddy simulation of the stratocumulus-topped boundary layer. Journal of Advances in Modeling Earth Systems, 8(2):885–903.

Peng, Z., Yu, D., Huang, D., Heiser, J., Yoo, S., and Kalb, P. (2015). 3d cloud detection and tracking system for solar forecast using multiple sky imagers. Solar Energy, 118:496–519. Publisher: Elsevier Ltd ISBN: 9781450324694.

Perez, R., Ineichen, P., Moore, K., Kmiecik, M., Chain, C., George, R., and Vignola, F. (2002). A new operational model for satellite-derived irradiances: description and validation. Solar Energy, 73(5):307–317.

Perez, R., Kivalov, S., Schlemmer, J., Hemker, K., Renn, D., and Hoff, T. E. (2010). Validation of short and medium term operational solar radiation forecasts in the US. Solar Energy, 84(12):2161–2172.

Pincus, R. and Stevens, B. (2009). Monte Carlo Spectral Integration: a Consistent Approximation for Radiative Transfer in Large Eddy Simulations: MONTE CARLO SPECTRAL INTEGRATION. Journal of Advances in Modeling Earth Systems, 1(2):n/a–n/a.

Pleim, J. E. (2007). A Combined Local and Nonlocal Closure Model for the Atmospheric Boundary Layer. Part I: Model Description and Testing. Journal of Applied Meteorology and Climatology, 46(9):1383–1395.

Rastogi, B., Williams, A. P., Fischer, D. T., Iacobellis, S. F., McEachern, K., Carvalho, L., Jones, C., Baguskas, S. A., and Still, C. J. (2016). Spatial and Temporal Patterns of Cloud Cover and Fog Inundation in Coastal California: Ecological Implications. Earth Interactions, 20(15):1–19.

Reynolds, D. W., Clark, D. A., Wilson, F. W., and Cook, L. (2012). Forecast-Based Decision Support for San Francisco International Airport: A NextGen Prototype System That Improves Operations during Summer Stratus Season. Bulletin of the American Meteorological Society, 93(10):1503–1518.

Rienecker, M. M., Suarez, M. J., Gelaro, R., Todling, R., Bacmeister, J., Liu, E., Bosilovich, M. G., Schubert, S. D., Takacs, L., Kim, G.-K., Bloom, S., Chen, J., Collins, D., Conaty, A., da Silva, A., Gu, W., Joiner, J., Koster, R. D., Lucchesi, R., Molod, A., Owens, T., Pawson, S., Pegion, P., Redder, C. R., Reichle, R., Robertson, F. R., Ruddick, A. G., Sienkiewicz, M., Woollen, J., Rienecker, M. M., Suarez, M. J., Gelaro, R., Todling, R., Julio Bacmeister, Liu, E., Bosilovich, M. G., Schubert, S. D., Takacs, L., Kim, G.-K., Bloom, S., Chen, J., Collins, D., Conaty, A., Silva, A. d., Gu, W., Joiner, J., Koster, R. D., Lucchesi, R., Molod, A., Owens, T., Pawson, S., Pegion, P., Redder, C. R., Reichle, R., Robertson, F. R., Ruddick, A. G., Sienkiewicz, M., and Woollen, J. (2011). MERRA: NASAs Modern-Era Retrospective Analysis for Research and Applications. Journal of Climate, 24(14):3624–3648.

Sahu, D. K., Yang, H., and Kleissl, J. (2018). Assimilating observations to simulate marine layer stratocumulus for solar forecasting. Solar Energy, 162:454–471.

Siebesma, A. P., Soares, P. M. M., and Teixeira, J. (2007). A Combined Eddy-Diffusivity Mass-Flux Approach for the Convective Boundary Layer. Journal of the Atmospheric Sciences, 64(4):1230–1248.

Siebesma, A. P. and Teixeira, J. (2000). An Advection-Diffusion scheme for the convective boundary layer: description and 1d-results. pages 14th Symp. on Boundary Layers and Turbulence, Aspen, CO, Amer. Meteor. Soc., 231–234.

Skamarock, W. C., Klemp, J. B., Dudhia, J., Gill, D. O., Liu, Z., Berner, J., Wang, W., Powers, J. G., Duda, M. G., Barker, D. M., and Huang, X.-Y. (2019). A Description of the Advanced Research WRF Model Version 4. page 162.

Soares, P. M. M., Miranda, P. M. A., Siebesma, A. P., and Teixeira, J. (2004). An eddy-diffusivity/mass-flux parametrization for dry and shallow cumulus convection. Quarterly Journal of the Royal Meteorological Society, 130(604):3365–3383.

SolarAnywhere (2019). Web-Based Service that Provides Hourly, Satellite-Derived Solar Irradiance Data Forecasted 7 Days Ahead and Archival Data Back to January 1, 1998.

Stevens, B. (2002). Entrainment in stratocumulus-topped mixed layers. Quarterly Journal of the Royal Meteorological Society, 128(586):2663–2690.

Stevens, B. (2010). Introduction to UCLA-LES.

Stevens, B., Lenschow, D. H., Vali, G., Gerber, H., Bandy, A., Blomquist, B., Brenguier, J. L., Bretherton, C. S., Burnet, F., Campos, T., Chai, S., Faloona, I., Friesen, D., Haimov, S., Laursen, K., Lilly, D. K., Loehrer, S. M., Malinowski, S. P., Morley, B., Petters, M. D., Rogers, D. C., Russell, L., Savic-Jovcic, V., Snider, J. R., Straub, D., Szumowski, M. J., Takagi, H., Thornton, D. C., Tschudi, M., Twohy, C., Wetzel, M., and van Zanten, M. C. (2003). Dynamics and Chemistry of Marine StratocumulusDYCOMS-II. Bulletin of the American Meteorological Society, 84(5):579–594.

Stevens, B., Moeng, C.-H., Ackerman, A. S., Bretherton, C. S., Chlond, A., de Roode, S., Edwards, J., Golaz, J.-C., Jiang, H., Khairoutdinov, M., Kirkpatrick, M. P., Lewellen, D. C., Lock, A., Mller, F., Stevens, D. E., Whelan, E., and Zhu, P. (2005). Evaluation of Large-Eddy Simulations via Observations of Nocturnal Marine Stratocumulus. Monthly Weather Review, 133(6):1443–1462.

Suselj, K., Kurowski, M. J., and Teixeira, J. (2019a). On the Factors Controlling the Development of Shallow Convection in Eddy-Diffusivity/Mass-Flux Models. Journal of the Atmospheric Sciences, 76(2):433–456.

Suselj, K., Kurowski, M. J., and Teixeira, J. (2019b). A Unified Eddy-Diffusivity/Mass-Flux Approach for Modeling Atmospheric Convection. Journal of the Atmospheric Sciences, 76(8):2505–2537.

Suselj, K., Teixeira, J., and Chung, D. (2013). A Unified Model for Moist Convective Boundary Layers Based on a Stochastic Eddy-Diffusivity/Mass-Flux Parameterization. Journal of the Atmospheric Sciences, 70(7):1929–1953.

Taylor, K. E. (2001). Summarizing multiple aspects of model performance in a single diagram. Journal of Geophysical Research: Atmospheres, 106(D7):7183–7192.

Teixeira, J. (1999). Simulation of fog with the ECMWF prognostic cloud scheme. Quarterly Journal of the Royal Meteorological Society, 125(554):529–552.

Teixeira, J., Cardoso, S., Bonazzola, M., Cole, J., DelGenio, A., DeMott, C., Franklin, C., Hannay, C., Jakob, C., Jiao, Y., Karlsson, J., Kitagawa, H., Khler, M., Kuwano-Yoshida, A.,

LeDrian, C., Li, J., Lock, A., Miller, M. J., Marquet, P., Martins, J., Mechoso, C. R., Meijgaard, E. v., Meinke, I., Miranda, P. M. A., Mironov, D., Neggers, R., Pan, H. L., Randall, D. A., Rasch, P. J., Rockel, B., Rossow, W. B., Ritter, B., Siebesma, A. P., Soares, P. M. M., Turk, F. J., Vaillancourt, P. A., Von Engeln, A., and Zhao, M. (2011). Tropical and Subtropical Cloud Transitions in Weather and Climate Prediction Models: The GCSS/WGNE Pacific Cross-Section Intercomparison (GPCI). Journal of Climate, 24(20):5223–5256.

Teixeira, J. and Siebesma, A. P. (2000). A Mass-Flux/K-Diffusion approach to the parameterization of the convective boundary layer: global model results. pages 14th Symp. on Boundary Layers and Turbulence, Aspen, CO, Amer. Meteor. Soc., 231–234.

Torregrosa, A., Combs, C., and Peters, J. (2016). GOES-derived fog and low cloud indices for coastal north and central California ecological analyses: COASTAL FLC FREQUENCY. Earth and Space Science, 3(2):46–67.

Weinreb, M. and Han, D. (2011). Conversion of GVAR Infrared Data to Scene Radiance or Temperature.

Williams, A. P., Schwartz, R. E., Iacobellis, S., Seager, R., Cook, B. I., Still, C. J., Husak, G., and Michaelsen, J. (2015). Urbanization causes increased cloud base height and decreased fog in coastal Southern California. Geophysical Research Letters, 42(5):1527–1536.

Witek, M. L., Teixeira, J., and Matheou, G. (2011). An Integrated TKE-Based Eddy Diffusivity/Mass Flux Boundary Layer Closure for the Dry Convective Boundary Layer. Journal of the Atmospheric Sciences, 68(7):1526–1540.

Wood, R. (2012). Stratocumulus Clouds. Monthly Weather Review, 140(8):2373–2423.

Wood, R. and Bretherton, C. S. (2006). On the relationship between stratiform low cloud cover and lower-tropospheric stability. Journal of Climate, 19(24):6425–6432. ISBN: 0894-8755.

Wu, E., Clemesha, R. E. S., and Kleissl, J. (2018). Coastal Stratocumulus cloud edge forecasts. Solar Energy, 164(September 2017):355–369. Publisher: Elsevier.

Wu, E., Yang, H., Kleissl, J., Suselj, K., Kurowski, M. J., and Teixeira, J. (2020). On the Parameterization of Convective Downdrafts for Marine Stratocumulus Clouds. Monthly Weather Review, in revision 12/2019.

Wu, E., Zapata, M. Z., Monache, L. D., and Kleissl, J. (2019). Observation-Based Analog Ensemble Solar Forecast in Coastal California. 46th IEEE Photovoltaic Specialists Conference (PVSC), page 5.

Yamaguchi, T. and Randall, D. A. (2011). Cooling of Entrained Parcels in a Large-Eddy Simulation. Journal of the Atmospheric Sciences, 69(3):1118–1136.

Yang, H. and Kleissl, J. (2016). Preprocessing WRF initial conditions for coastal stratocumulus forecasting. Solar Energy, 133:180–193.

Yang, H., Kurtz, B., Nguyen, D., Urquhart, B., Chow, C. W., Ghonima, M., and Kleissl, J. (2014). Solar irradiance forecasting using a ground-based sky imager developed at UC San Diego. Solar Energy, 103:502–524.

Zamora Zapata, M., Norris, J. R., and Kleissl, J. (2020). Coastal stratocumulus dissipation dependence on initial conditions and boundary forcings in a Mixed-Layer Model. In preparation.

Zelinka, M. D., Randall, D. A., Webb, M. J., and Klein, S. A. (2017). Clearing clouds of uncertainty. Nature Climate Change, 7:674–678.

Zhong, X. (2017). Advancing solar irradiance/marine layer stratocumulus forecasting in California. PhD thesis, UC San Diego.

Zhong, X., Sahu, D. K., and Kleissl, J. (2017). WRF inversion base height ensembles for simulating marine boundary layer stratocumulus. Solar Energy, 146:50–64.